Astronomy & Astrophysics manuscript no. aa_example_clean
June 5, 2026
©ESO 2026

arXiv:2606.06005v1 [astro-ph.GA] 4 Jun 2026

The Multi-phase Biconical Outflow in the local IR-Luminous Merger IRASF01364-1042

Y. Song[1,2,3⋆], V. U[4,5], J. Kader[5], M. Bianchin[5,6,7,⋆⋆], J. Agostino[8], L. Barcos-Muñoz[9,10], N. Torres-Albà[10], A. Medling[8], C. Ricci[11,12], L. Armus[4], T. Lai[4], L. Ghodsi[13], A. Evans[9,10], H. Inami[14], S. Stierwalt[15], T. Bohn[14], K. L. Emig[9], V. Buiten[16], G. Donnelly[8], E. Treister[17], A. Jimenez-Gallardo[1], T. Böker[18], D. Kakkad[19], S. Linden[20], P. van der Werf[16], V. Charmandaris[21,22,23], R. Remigio[5], L. Lenkić[4], C. Finlez[1,2], M. Sanchez-García[22,23], C. Lofaro[22,23], A. Saravia[9,10], I. Yoon[9], G. C. Privon[9,10,24], T. Gao[25,26], H. Aziz[5], R. McGurk[27], T. Díaz-Santos[22,23], D. Kunneriath[9], and David B. Sanders[28]

(Affiliations can be found after the references)

June 5, 2026

ABSTRACT

Aims. We investigate the spatially-resolved ISM properties of the local (z = 0.048), IR-luminous ($L_{\rm IR}$ = $10^{11.87}$ $L_\odot$), late-stage galaxy merger IRAS F01364-1042, combining multi-wavelength IFU observations from *JWST/MIRI-MRS*, ALMA and Keck/KCWI. The system exhibits excess emission from mid-IR H_2 lines relative to dust, as identified in a previous *Spitzer/IRS* survey of local IR-luminous galaxies (LIRGs). The bright H_2 emission was speculated to arise from widespread shocks associated with a powerful starburst/AGN-driven outflow.

Methods. Using our multi-wavelength datasets, we assess and compare the resolved morphology and kinematics of multi-phase gas tracers on sub-kpc scales. We construct emission line maps of several key tracers of the ionized (e.g., [Ne II] 12.8μm, [O III]λ5007), warm molecular (e.g., H_2 0-0 S(3)), and cold molecular gas (e.g., CO (J= 2 − 1)), and perform detailed decomposition of spectra extracted in resolved regions across the areas of emission, with a focus on the central ∼ 3 kpc of the system covered by all our datasets.

Results. We confirm the presence of a multi-phase galactic biconical outflow along the minor axis of a highly inclined rotating disk, based on the multi-phase gas morphology and prominent line broadening (FWHM > 500 km s^{-1}) in the ionized gas tracers detected out to ∼ 5 kpc from the nucleus. The molecular gas tracers are detected out to ∼2 kpc, and exhibit a distinct "X"-shaped morphology and different velocity fields from the ionized gas, which we attribute to the higher concentration of molecular gas near the disk. We adopt a simple model to interpret the observed multiphase gas kinematics and infer an outflow velocity of ∼ 500 - 600 km s^{-1} ∼350 km s^{-1}, and ∼ 200 - 300 km s^{-1}, in the ionized, warm and cold molecular phase, respectively, with corresponding mass outflow rates of ∼ 0.3 − 2.3, ∼ 31, and ∼ 38 − 240 $M_\odot$ yr^{-1}. The cold molecular phase dominates both the total mass outflow rate and the associated kinetic energy (∼ 2 − 8 × 10^{42} erg s^{-1}). Via *JWST/MIRI-MRS* detection of the [Ne V] 14.3μm line, we identify, for the first time, a dust-obscured AGN in IRAS F01364-1042. The low inferred AGN bolometric luminosity (1.2 − 1.8 × 10^{43} erg s^{-1}) suggests that the nuclear starburst alone, with a star formation rate of ∼ 40 − 60 $M_\odot$ yr^{-1}, can account for the energy required to drive the outflow, though a more active AGN phase in the recent past may have also played a role.

Conclusions. Our work showcases the necessity of multi-wavelength observations in interpreting the gas dynamics in merger-driven dusty starbursts, and the capability of *JWST/MIRI-MRS* in uncovering obscured low-luminosity AGN that may be common in these systems.

Key words. Galaxies: ISM – Galaxies: nuclei – Galaxies: starburst – Galaxies: individual: IRASF01364-1042

1. Introduction

Gas-rich galaxy mergers represent a crucial transformative phase in the formation and evolution of massive galaxies. Simulations have predicted that nuclear gas inflows due to strong gravitational torque during a merger would trigger both a powerful nuclear starburst and accretion onto the central supermassive black hole (SMBH) (e.g., Di Matteo et al. 2005; Springel et al. 2005a; Hopkins et al. 2006). During this phase, rapid, simultaneous growth of the galaxy's stellar content and the SMBH takes place behind thick layers of dust and gas (e.g., Blecha et al. 2018), until the energy released by the accreting SMBH (i.e., Active Galactic Nuclei, or AGN) disperses the obscuring materials, revealing the bright and powerful central engine as a quasar (Springel et al. 2005b; Hopkins et al. 2005). This clearing process, so called "AGN feedback", in the form of winds and outflows, is thought to be responsible for shutting down galaxy star formation (SF) and further SMBH growth, which eventually leads to the formation of massive quiescent galaxies (e.g., Springel et al. 2005b; Khalatyan et al. 2008; Hopkins et al. 2013). Throughout this transformation, the SMBH and its host galaxy would evolve in tandem (e.g., Silk & Rees 1998; Kauffmann & Haehnelt 2000; Wyithe & Loeb 2003), which may explain the observed cut-off at the bright end of the local galaxy luminosity distribution (e.g., Bower et al. 2006), and the widely observed tight relations between the masses of SMBHs and various properties of their host galaxies (i.e., stellar velocity dispersion, bulge mass, and luminosity; e.g., Magorrian et al. 1998; Ferrarese & Merritt 2000; McConnell & Ma 2013).

Luminous and Ultra-luminous Infra-Red Galaxies (LIRGs: $L_{\rm IR[8-1000\mu m]}$ > $10^{11-12}L_\odot$; ULIRGs: $L_{\rm IR[8-1000\mu m]}$ > $10^{12}L_\odot$) in the local Universe (z < 0.1) provide the best laboratories to study in detail the fueling and feedback processes that are associated with the above evolutionary scenario. Predominantly triggered by interactions/mergers between gas-rich spirals (see review by Sanders & Mirabel 1996), these systems are known to host ex-

⋆ e-mail: yiqing.song@eso.org
⋆⋆ IAU Gruber Fellow

tremely compact ($r \lesssim 100$ pc) nuclear starbursts that reach above 1000 $M_\odot$ yr^{-1} kpc^{-2} in star formation rate (SFR) surface density ($\Sigma_{\rm SFR}$; e.g., Condon et al. 1991; Barcos-Muñoz et al. 2017; U et al. 2019; Larson et al. 2020; Song et al. 2022). In many cases, these starbursts are accompanied by powerful, but heavily-obscured AGN ($N_{\rm H} > 10^{23}$ cm^{-2}) that are detected only in the radio, mid-IR and hard X-rays (e.g., Iwasawa et al. 2011; Stierwalt et al. 2013; Petric et al. 2011; Vardoulaki et al. 2015a; Inami et al. 2018; Torres-Albà et al. 2018; Ricci et al. 2021), and can even reach quasar luminosity (Boksenberg et al. 1977; Sanders et al. 1988; Rupke & Veilleux 2013). These extreme nuclear activities also drive powerful outflows that have been observed ubiquitously in local U/LIRGs across different ISM phases and physical scales (e.g., Heckman et al. 1990; Rupke et al. 2005b; Veilleux et al. 2005, 2013; Spoon et al. 2013; Cicone et al. 2014; Hill & Zakamska 2014; Cazzoli et al. 2016; Barcos-Muñoz et al. 2018; Pereira-Santaella et al. 2018; U et al. 2019; Lutz et al. 2020; Fluetsch et al. 2021; Perna et al. 2021; Lamperti et al. 2022), manifesting signs of rapid galactic scale transformation as predicted by theoretical works. However, many studies associate these outflows with the nuclear starburst rather than AGN activity (e.g. Rupke et al. 2005a; Lamperti et al. 2022), the role of which remains challenging to quantify as their signatures are often attenuated by the heavy nuclear dust extinction.

The supreme spatial resolution and sensitivity of the *James Webb Space Telescope* (JWST; Gardner et al. 2023) have enabled a new, detailed view of the multi-phase ISM in local U/LIRGs, providing low-extinction and spatially-resolved diagnostics on the properties of the interstellar dust, ionized, hot ($T \sim 1000 - 3000$ K) and warm ($100 \lesssim T \lesssim 1000$ K) molecular gas around their obscured nuclei on sub-kpc scales, as has been successfully demonstrated with the Early Science Release program 1328 (PI: L. Armus, A. Evans; e.g., Lai et al. 2022; U et al. 2022; Lai et al. 2023; Armus et al. 2023; Rich et al. 2023; Bianchin et al. 2024; Buiten et al. 2024; Bohn et al. 2024). To this end, we have obtained new *JWST/MIRI-MRS* observations in Cycle-1 (1717; PI: V. U) to study the ISM properties in seven local U/LIRGs from the Great Observatories All-sky LIRG Survey (GOALS; Armus et al. 2009) selected based on their extraordinarily bright Near- and Mid-IR (NIR and MIR) H_2 emission. These galaxies were first highlighted by Stierwalt et al. (2013, 2014) based on their high H_2/PAH luminosity ratios measured with *Spitzer/IRS* on >kpc scales, which were attributed to enhanced rotational H_2 emission from either AGN heating or shocked warm molecular gas, rather than weak PAH emission that traces SF. Observations with Keck/OSIRIS similarly revealed enhanced NIR ro-vibrational H_2 relative to Brγ emission in the immediate vicinity of these galactic nuclei at spatial resolutions of $\lesssim 100$ pc (e.g. Medling et al. 2014; U et al. 2019), pointing to nuclear activity as a key driver behind the enhanced H_2 emission. These new *JWST/MIRI-MRS* observations, further complemented by ancillary multi-wavelength IFU datasets from Keck, VLT and ALMA, allow comprehensive multiphase diagnostics on the nuclear power source and putative outflows in these bright H_2-emitters at matched, sub-kpc scales. Several case studies utilizing these datasets have been presented by U et al. (2022), Bianchin et al. (2024) and Kader et al. (2026), who identified powerful multi-phase outflows driven by AGN photo-ionization and/or radio jets in the Seyfert galaxies NGC 7469 and VV 340a.

In this work we focus on a starburst-dominated galaxy from the sample, the late-stage galaxy merger and LIRG ($L_{\rm IR} = 10^{11.87}$ L$_\odot$; Armus et al. 2009), IRASF01364−1042 (hereafter as IRASF01364), shown in Figure 1. As noted by Stierwalt et al. (2014), IRASF01364 shows distinctly high $L_{\rm H_2}/L_{\rm PAH}$ and $L_{\rm H_2}/L_{\rm IR}$ ratios among galaxies in the GOALS sample, making it a promising target to search for shocked molecular outflows at higher spatial resolution. While its compactness and high luminosity surface density in the radio suggest an AGN presence (Vardoulaki et al. 2015b; Barcos-Muñoz et al. 2017; Song et al. 2022), observations in the mid-IR (MIR), X-ray and optical all indicate starburst activity as the dominant source of its bolometric luminosity (Stierwalt et al. 2013; Veilleux et al. 1995; Yuan et al. 2010; Iwasawa et al. 2011; Díaz-Santos et al. 2017). Interpretation of these results is complicated by the relatively low spatial/spectral resolution of the datasets, as well as high dust content in the source, as evidenced by its high IR/UV ratio (~ 250; Howell et al. 2010) and deep 9.7 μm silicate absorption feature ($s_{9.7} = -1.27$; Stierwalt et al. 2013). High-resolution ground-based NIR IFU observations reveal a 200 pc-radius rotating nuclear gas disk in ro-vibrational H_2 and Paα emission, with the former showing turbulent motion beyond the nuclear disk that potential traces a nuclear molecular outflow (Medling et al. 2014, 2015; U et al. 2019).

In this work we report the first confirmation and characterization of a kpc-scale multi-phase biconical outflow and a dust-obscured AGN in IRASF01364, combining new sensitive IFU observations from *JWST/MIRI-MRS*, Keck/KCWI and ALMA. The article is organized as follows: In Section 2 we present the observations utilized in this work and the data reduction procedures. We describe the analyses performed on the multi-wavelength datasets in Section 3 and present the key results in Section 4 where we identify the kinematic and morphological signature of the outflow, as well as characterize the spatially-resolved properties of the dust and multi-phase gas in the system. We combine these results to infer the energetics of the newly-confirmed outflow and its origin in Section 5, in the context of similar galactic outflows reported in the literature. We summarize the main findings in Section 6.

Throughout this article, we adopt cosmological parameters $H_0 = 70\,{\rm km\,s^{-1}Mpc^{-1}}$, $\Omega_{\rm vaccum} = 0.72$ and $\Omega_{\rm matter} = 0.28$ based on the 5 yr Wilkinson Microwave Anisotropy Probe result (Hinshaw et al. 2009) and the three-attractor model (Mould et al. 2000). IRASF01364 has a redshift of $z = 0.04819$ determined from optical stellar absorption features (see Section 2.4), corresponding to a luminosity distance of $D_{\rm L} = 214$ Mpc, with a scale of 945 pc/″.

2. Data & Reduction

2.1. HST

To visualize the optical morphology of IRASF01364, we download calibrated *HST* images in filters *F*336*W*, *F*435*W* and *F*814*W* (ID: 10592, 16914; PI: A. Evans; Kim et al. 2013, Evans et al. in prep.) from the the Mikulski Archive for Space Telescopes Portal (MAST)[1]. The central wavelengths and widths of the HST filters, in units of Å, are 3361 and 554, 4297 and 1038, 8333 and 2511, respectively, for *F*336*W*, *F*435*W* and *F*814*W* [2].The images are corrected for astrometric offsets using field stars with coordinates provided in Gaia DR3 catalogue (Gaia Collaboration et al. 2023) as initial references, and the corrections were visually fine-tuned using common features seen in the images, resulting in an average correction of −0.″3

[1] https://mast.stsci.edu
[2] https://hst-docs.stsci.edu

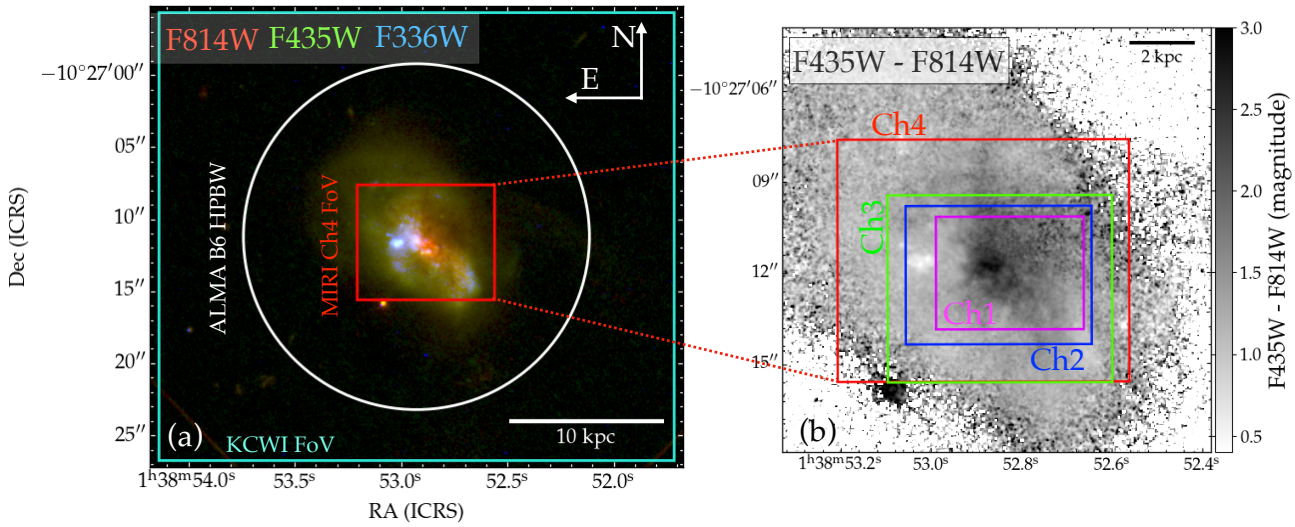


Fig. 1: *HST* images of IRAS F01364-1042. (a): False color image with F336W, F435W and F814W filters, which are represented in blue, green and red, respectively. The Half-Power-Beam-Width (HPBW) of the ALMA Band 6 primary beam, and the fields-of-view (FoVs) of the calibrated data cubes from Keck/KCWI and the longest wavelength channel of *JWST/MIRI-MRS* (i.e., ch4) are outlined in white, cyan and red, respectively. (b) Zoom-in of the *HST* F435W - F814W map in magnitude, where a darker grey shade indicates a redder (F435W - F814W) color, and thus higher dust extinction. Colored boxes outline the FoVs of the *JWST/MIRI-MRS* ch1-ch4 cubes. Prominent, non-uniform dust structures can be seen extending from the nucleus out to ~ 5 kpc into the galaxy. The large FoVs of the Keck/KCWI and ALMA datasets allow characterization of the ISM across the entire system, while *JWST/MIRI-MRS* probes the immediate vicinity of the dust-obscured nucleus.

in RA and +0.″4 in DEC. In Figure 1, we show a zoomed-in view of the HST color composite image centered on the system, with $F336W$ (blue), $F435W$ (green) and $F814W$ (red) tracing emission from un-obscured young massive stars, tidal features and dusty materials, respectively. In the same Figure we further show the $F435W - F814W$ map to highlight the heavy and non-uniform dust extinction at and around the galaxy nucleus, underlining the necessity of *JWST/MIRI* observations for uncovering its nature. The fields-of-view (FoVs) of the multi-wavelength IFU datasets (see the next Sections) are also visualized.

2.2. JWST/MIRI-MRS

Mid-infrared IFU observations of IRASF01364 were conducted with the JWST Mid-InfraRed Instrument (MIRI; Rieke et al. 2015) in Medium Resolution Spectroscopy (MRS) mode (hereafter as *MRS*; Wells et al. 2015) on August 23, 2023, as part of Cycle-1 GO Program 1717 (PI: V. U). Exposures across the short (A), medium (B), and long (C) sub-bands of each of the four wavelength channels resulted in observations that cover the full 4.9 – 28.8 μm range. The SLOWR1 readout pattern and standard 4-point dither pattern were adopted in each sub-band observation of the science target, with an integration time of 800 s per exposure. Dedicated background exposures were taken within each of the three sub-bands using a 2-point dither pattern.

The uncalibrated frames were downloaded from MAST and reduced using the JWST Science Calibration Pipeline version 1.18.0 (Bushouse et al. 2023) and CRDS context of `jwst_1364.pmap`. We utilized the official MIRI MRS Pipeline Notebook (Law et al. 2025)[3], which includes steps to apply detector-level corrections, outlier/cosmic-ray shower detection, wavelength calibration, flux calibration, background subtraction, and co-addition of dither frames. The final calibrated cubes have FoVs of 5.″1×4.″3, 6.″3×5.″3, 7.″8×7.″0, and 9.″5×9.″5 (see Figure 1), with spaxel sizes of 0.″13, 0.″20, 0.″245, and 0.″273 for channel 1, 2, 3 and 4, respectively. We adopt wavelength-dependent spectral resolutions (R) characterized by Argyriou et al. (2023), which yield R(λ) = 4603 - 128λ, where λ is the observed wavelength in μm. We perform an astrometric correction by aligning the emission peak of the collapsed channel cubes with that of the 334 GHz dust continuum image from ALMA (see Section 2.3), both of which are dominated by the IR-bright nucleus. The average corrections are −0.″02 in RA and −0.″08 in DEC, in line with the expected pointing performance of JWST (Patapis et al. 2024). Following Lai et al. (2023), we model the point-spread-function (PSF) at each channel using *MRS* observations of the standard star HD 159222 (PID: 1050; PI: B. Vandenbussche), which yield Full-Width-Half-Maximum (FWHM) of ~ 0.″27−0.″31, 0.″38−0.″46, 0.″53−0.″66 and 0.″80−1.″05 for ch1, ch2, ch3 and ch4, respectively. In Figure 2, we display maps of the median flux values at rest-frame 5, 10, 15, 25 μm to illustrate the increasing PSF size towards longer wavelengths. The full spectra extracted from all *MRS* cubes using two different apertures are also shown in the same Figure along with *Spitzer/IRS* spectrum of the entire galaxy (extracted with a 10″ × 4″ slit; Stierwalt et al. 2013) to showcase the high spectral resolution of the former. We describe the spectral extractions in Section 3.1.

2.3. ALMA

We utilize archival sub-arcsecond ALMA datasets for IRASF01364 from programs 2017.1.01235.S, 2018.1.00279.S (Band 3 and 7; PI: L. Barcos-Muñoz) and 2019.1.00811.S (Band 6; PI: A. Medling; Agostino et al. 2026) to compare the multi-frequency continuum and bulk molecular gas emission traced by CO (J = 1-0, 2-1, 3-2) with MIR emission probed by *MRS*. To minimize biases related to interferometric spatial

[3] https://github.com/spacetelescope/jwst-pipeline-notebooks

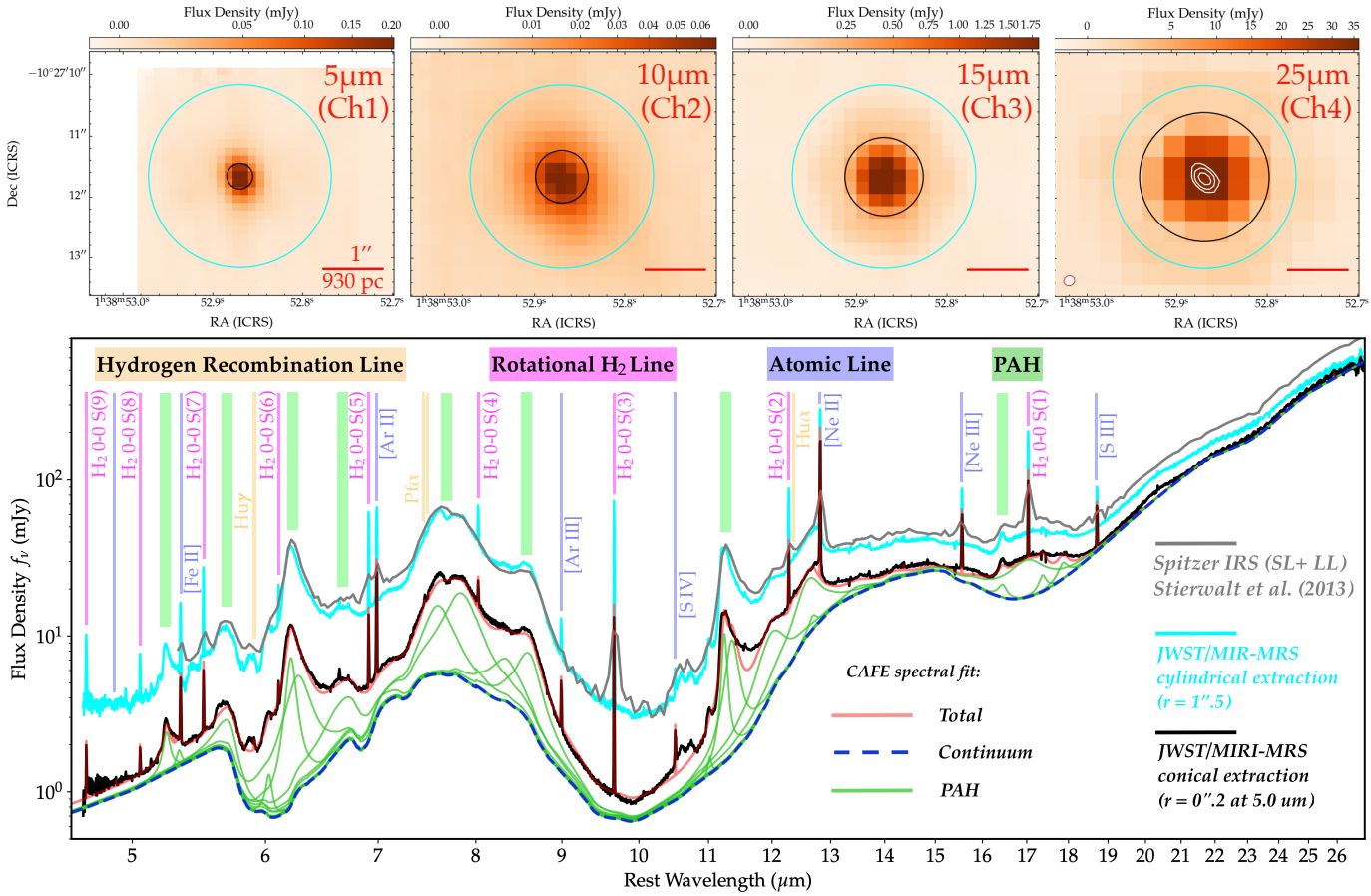


Fig. 2: MIR emission of IRASF01364 across the *MRS* wavelength range. *Top:* Median flux density map at rest-frame 5, 10, 15, 25 μm from ch1, ch2, ch3 and ch4 cubes, respectively. All images are zoomed to the same scale, where the physical size corresponding to 1″ is indicated with the red scale bar in the lower right corner of each panel. The cyan circles, with a fixed radius of r = 1.″5, indicate the cylindrical aperture used to extract the integrated MIR spectrum from the central ∼ 3 kpc of the galaxy that is covered by all channel cubes. The black circles indicate the expanding conical aperture, with r = 0.″2 at 5 μm and r = 1.″0 at 25 μm, used to extract the spectrum of the compact (∼ 100 pc) nuclear starburst, as portrayed by the ALMA 334 GHz continuum, shown in white contours. The red ellipse indicates the synthesized beam size of the 334 GHz continuum image (see Section 2.3). *Bottom: Spitzer/IRS* spectrum from Stierwalt et al. (2013) (in grey), compared to the full *MRS* spectra extracted with the fixed-radius, cylindrical aperture (cyan) and expanding conical aperture (black). For the latter, the total fitted spectral profile and the underlying continuum and PAH profiles from `CAFE` spectral decomposition are overlaid in red, dark blue (dashed) and green, respectively. See Section 3.1 for details. While recovering the emission previously detected with *Spitzer/IRS*, the high spectral resolution of *MRS* allows a much more detailed characterization of the various MIR emission and absorption features present in IRASF01364.

filtering, from these ALMA programs we select only observations that recover emission larger than 1″ (i.e., the Largest Angular Scale, LAS > 1″) to more properly compare with *MRS* observations. Details of these datasets are provided in Table A.1 in Appendix A. All observations are single-pointing, and we illustrate the Half-Power-Beam-Width (HPBW) of the Primary Beam (∼ 24″) at Band 6 in Figure 1.

We download the raw datasets from the ALMA Science Archive[4] and recover the calibrated MeasurementSet (MS) for each dataset by rerunning the `scriptForPI.py` script using CASA (McMullin et al. 2007; CASA Team et al. 2022) in pipeline mode using the version listed in the associated QA2 report. We then image the continuum emission at each Band using CASA `tclean` after flagging line emission in each MS, combining MSs from multiple executions and/or array configurations, using the multi-term multi-frequency deconvolver (Rau & Cornwell 2011) with `nterms` of 2 to account for the likely non-flat continuum spectral shape. Afterwards, we recover the flagged line emission in each MS, perform continuum subtraction using `uvcontsub`, and image the CO line emission cube combining MSs covering the same CO transition, in native velocity channels of 10.5, 10.5 and 7.1 km s^{-1}, respectively for the Band 3, 6 and 7 datasets. We adopt the `MultiScale` deconvolving algorithm (Cornwell 2008) with scales of 5, 10, 30 pixels to model the line emission with components of different sizes, with pixel cell sizes of 0.″05, 0.″06 and 0.″07 for the Band 3, 6 and 7 images respectively. For both the continuum and line imaging, we adopt Briggs weighting with robustness of `2.0` (Briggs 1995) to emphasize the extended emission, and manually draw the clean masks iteratively until no significant residual remains down to the 1$\sigma_{\rm rms}$ threshold, where $\sigma_{\rm rms}$ is the root-mean-square noise measured from an emission-free region in the dirty image, reported in Table A.1 along with other properties of the final cleaned images and cubes. The synthesized beams of the final imaging products have FWHM

[4] https://almascience.eso.org/aq/

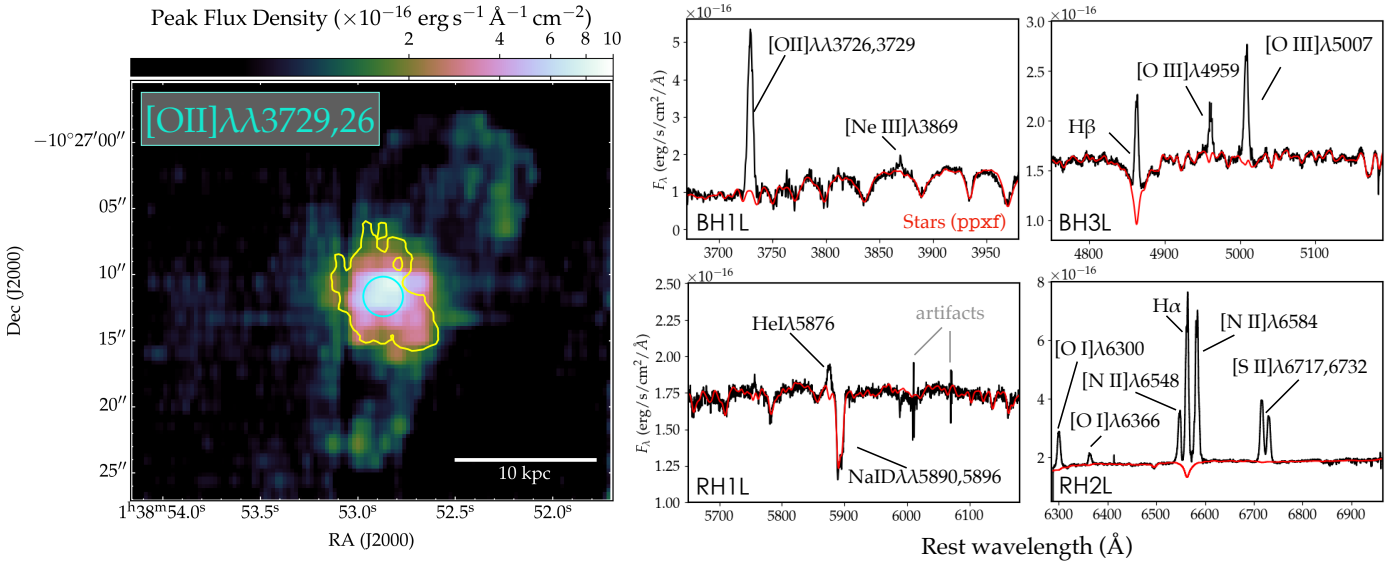


Fig. 3: Optical emission of IRASF01364 as observed by Keck/KCWI. *Left:* Map of the peak flux density of the [O II]$\lambda\lambda$3729,3726 line, overlaid with the 5σ contour of the stellar continuum measured in the adjacent wavelength range, in yellow. For context, the cyan circle marks the aperture used to extract the integrated *MRS* spectrum shown in Figure 2. The same aperture is used to extract the spectra shown in the *right* panels. *Right:* KCWI spectra extracted from the final reduced and aligned BH1L, BH3L, RH1L and RH2L cubes. The fitted stellar spectra derived from `ppxf` are shown in red. See Section 3.3 for details. The [O II] emission map reveals extended ionized gas emission around IRASF01364 beyond the bulk of the stellar emission on 10 kpc-scale. A number of other key emission lines are also detected, allowing further characterization of the ionized gas properties.

of $\sim$ 0.″3 – 0.″5 across all three Bands. The contours from the Band 7 334 GHz continuum image, which has the smallest synthesized beam, are also shown in Figure 2.

2.4. Keck/KCWI

To complement the *MRS* observation of the central region of IRASF01364, we further obtained new optical wide-field IFU observations with the Keck Cosmic Wave Imager (Morrissey et al. 2018) on the Keck II telescope (2023B_K454; PI: R. McGurk). The observations were carried out on September 17, 2023 under clear sky conditions with seeing of 0.″9 using a two-point dither pattern with a dedicated off-target sky frame. The BH1, BH3, RH1 and RH2 gratings were adopted to cover wavelength ranges of 3500–4100, 4700–5600, 5900-6485 and 6592-7297 Å, respectively, with a high spectral resolution of $R \sim 3500$ and ~ 4500, for RH and BH gratings, respectively. Utilizing the large IFU slicer, we achieve a FoV of 33″ × 20.″4 per pointing with slit width-limited angular resolution (0.″3 sampling rate along the 1.″4-wide slit). The detector was spatially binned by a factor of 2×2. Basic reduction and wavelength solutions for the spectroscopic data were performed using the official KCWI data reduction pipeline `KCWI_DRP` v1.0 [5], which also performs flux calibration and sky subtraction using dedicated sky pointings. The individual spectral cubes were cropped and co-added using the `CWITools` Python package (O'Sullivan & Chen 2020). The reduced data cubes have a common FOV of 36″×32″ in pixel scale of 0.″29, outlined in Figure 1 in cyan, and the instrumental FWHM for the emission lines was measured to be 0.9 Å. We use the WCS-corrected *HST* F336W and F435W images (see Section 2.1) as reference for fine-tuning the astrometry of the KCWI cubes until the UV/optical continuum morphology traced by these datasets visually match. The average corrections are −0.″8 in RA and +0.″7 in DEC for the RH gratings and −1.″1 in RA and −2.″3 in DEC for the BH gratings.

In Figure 3 we showcase the data quality, in particular highlighting the extended ionized gas emission as traced by the [O II]$\lambda\lambda$3729,3726 doublet covered by the BH1L cube, as well as spectra extracted from all four cubes, which we analyze in more detail in Section 3.3. As the BH1L spectrum shows the most prominent stellar absorption features, we derive the source redshift from this spectrum by performing spectral fitting with `ppxf` (Cappellari 2023) and the FSPS stellar templates (Conroy et al. 2009; Conroy & Gunn 2010). The resulted redshift is $z = 0.04819 \pm 0.00012$ accounting for the uncertainties associated with the spectral resolution ($\sim$ 34 km/s). We experiment with different aperture radii (i.e., 0.″5, 1.″0, 2.″0) for spectral extraction, which yield consistent results. The derived value also agrees well with the redshift (i.e., 0.04823) reported in the NASA/IPAC Extragalactic Database (NED[6]), obtained from SDSS DR13 (Albareti et al. 2017). The wavelength ranges spanned by the data cubes cover important emission lines for diagnostics of the excitation, dust extinction and density of the ionized gas, e.g.,[O II]$\lambda\lambda$3729,3726, Hβ, [O III]$\lambda\lambda$4959,5007, [O I]$\lambda\lambda$6300,6366, Hα, [N II]$\lambda\lambda$6548,6584 and [S II]$\lambda\lambda$6717,6732, etc. Additionally, the RH1L grating covers Na ID absorptions at 5890 and 5896 Å. Due to the redshift of IRASF01364, the Hα-[N II] spectral complex coincides with the atmospheric telluric O_2 B-band absorption feature. We remove this feature via an iterative process using a model O_2 B-band spectrum assuming $T = 296$ K, downloaded from the GEISA 2015 atmospheric molecular line database[7], after applying a small (1.75 Å) shift and scaling factor to the absorption line widths, until the continuum level within and outside the Hα-[N II] complex match.

[5] https://kcwi-drp.readthedocs.io

[6] https://ned.ipac.caltech.edu/

[7] https://geisa.aeris-data.fr/geisa-2015

3. Analysis

3.1. MIRI-MRS

3.1.1. Spectral decomposition & PAH fitting with CAFE

To conduct an initial assessment of the MIR spectral properties of IRASF01364, we utilize the spectral fitting tool CAFE[8](Marshall et al. 2007; Diaz-Santos et al. 2025). The program performs extraction and stitching of spectra from *MRS* channel cubes, using the longest-wavelength cube as reference, as well as decomposition of the stitched full spectrum into multi-temperature continuum, emission lines, and PAH components. Designed to allow flexible modeling of the complex and often blended PAH profiles, the program also computes wavelength-dependent attenuation (e.g. Lai et al. 2024) due to absorptions from silicates, water ice and hydrogenated amorphous carbon for estimating the intrinsic fluxes of individual PAH features.

As the MIR emission of IRASF01364 is dominated by the nuclear starburst, we first focus on analyzing the nuclear spectrum across all *MRS* channels extracted with CAFE. To isolate emission from the nuclear starburst, which spans $\sim$ 0.″4 in the 334 GHz continuum (see Figure 2), we adopt a conical aperture centered on the 334 GHz emission peak (i.e., RA= 24.72029 deg, DEC=−10.45324 deg) with a radius of 0.″2 at 5.0 μm and 1.″0 at 25.0 μm, to account for the increasing *MRS* PSF with wavelength (see Section 2.2). As the chosen aperture size is twice the PSF FWHM at any given wavelength, no aperture correction was performed. The aperture sizes and the extracted spectrum, along with the results of spectral decomposition with CAFE are shown in Figure 2. We later refer to this spectrum as the "nuclear" spectrum. The observed and attenuation-corrected fluxes of the PAH features obtained from CAFE are listed in Table B.1.

In Figure 2, we also show, in cyan, another spectrum extracted with a cylindrical aperture with a fixed radius of r = 1.″5. This is chosen to capture the total MIR emission from the central 3 kpc, which is the largest area covered by all *MRS* channels. This spectrum closely matches that obtained with *Spitzer/IRS* with a slit size of $\sim 10'' \times 4''$ (Stierwalt et al. 2013, 2014), shown in grey, confirming that the bulk of the mid-IR emission from the system is concentrated in the central few kpc. We later refer to the area defined by this cylindrical aperture as the "central" region or region C, for which we also extract profiles of the sub-mm CO lines from ALMA datasets (Section 3.2) and the optical emission lines from Keck/KCWI cubes (Section 3.3) to perform a direct comparison between multi-phase gas tracers observed within the central $\sim$ 3 kpc of the galaxy. The PAH fluxes obtained with CAFE from this central region are also reported in Table B.1.

3.1.2. Multi-component fitting of emission lines

As CAFE is designed to model the full MIR spectrum and PAH features rather than individual emission lines (Marshall et al. 2007), we further perform more detailed multi-component Gaussian fitting with lmfit[9] (Newville et al. 2025) of each emission line to more robustly characterize their flux and kinematics. For each line, we first model and subtract the local continuum in adjacent line-free regions between 0.02 to 0.06 μm away from the expected central wavelength, using a third-degree Legendre polynomial. Several atomic lines exhibit double-peaked profiles and broad line wings, indicating the presence of multiple kinematic components. Hence, we model the continuum-subtracted line profile three times, with one, two and three Gaussian components, respectively. Each component is restricted to have a central velocity within [-500, 500] km s^{-1} of the line center, and a linewidth larger than the instrumental linewidth at the observed wavelength (see Section 2.2). We adopt the default Levenberg-Marquardt algorithm for the least-square minimization, accounting for the flux uncertainties associated with the spectrum by providing its reciprocal as weights to the residual. We then choose among the three different models the one with the lowest value of the Bayesian Information Criterion (BIC) as the best-fit that sufficiently characterizes the line profile without overfitting. We show the fitting results for Huδ, H_2 0-0 S(2) and [Ne III] 15.6 μm in Appendix C as examples to illustrate the model selection process.

Besides the lines already identified by CAFE (see Figure 2), we also search for highly-ionized coronal lines from Satyapal et al. (2021) that may reveal elusive AGN activity in IRASF01364. Notably, the [Ne V] 14.3 μm line with ionizing potentials (IP) of 97 eV is detected at SNR> 5 in both the nuclear and central spectra, while other coronal lines are either not detected or heavily blended with weak PAH or molecular features that prevents reliable identification (e.g., [Mg V] 13.5 μm;

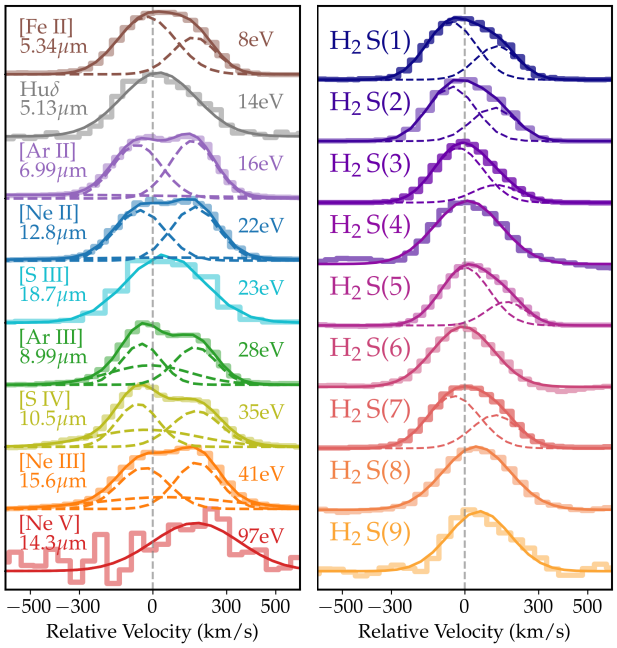


Fig. 4: Spectral profiles of atomic (*left*) and rotational H_2 lines (*right*) detected in the *MRS* nuclear spectrum, defined in Section 3.1.1 and shown in Figure 2 (in black). All profiles are normalized by the peak line flux density, displayed in velocity space relative to the expected line center based on the redshift of the galaxy (i.e., z = 0.04819) and offset vertically for visualization. From top to bottom, the atomic lines are arranged in order of increasing ionizing potential, and the H_2 lines are ordered from H_2 0-0 S(1) to H_2 0-0 S(9). The best-fit models are displayed in solid lines, with individual fitted Gaussian components shown in dashed lines. The best-fit parameters are presented in Table D.1. See Section 3.1.2 for details. Most ionized gas tracers and some H_2 lines show signs of multiple kinematic components, while broad components with FWHM > 500 km s^{-1} are only detected in the former.

[8] https://github.com/GOALS-survey/CAFE
[9] https://lmfit.github.io/lmfit-py

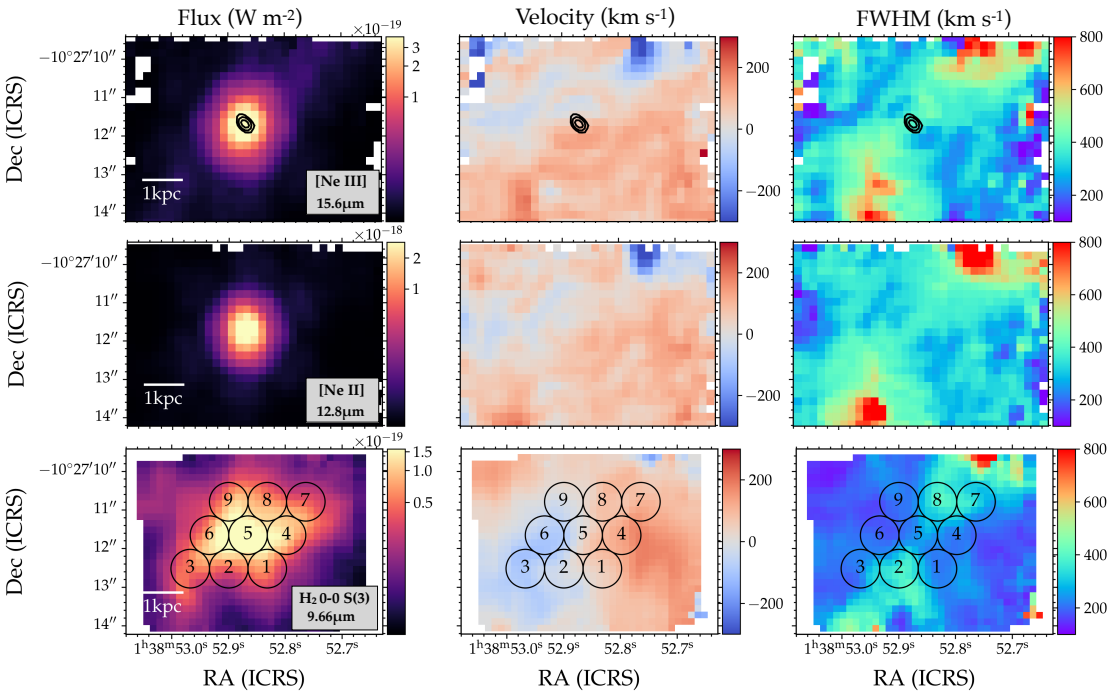


Fig. 5: *MRS* maps of the integrated line flux, velocity and FWHM linewidth for [Ne III], [Ne II] and H_2 0-0 S(3) lines (see Section 3.1.3). Spaxels with SNR < 3 in each line are masked. ALMA 334 GHz continuum contours from Figure 2 are overlaid in the [Ne III] maps, and the spectral extraction regions defined in Section 3.1.3 are overlaid on the H_2 0-0 S(3) maps. While ionized gas tracers ([Ne II], [Ne III]) show compact emission at the nucleus, molecular gas traced by the H_2 line shows extended "X"-shaped morphology on ∼ 3 kpc scales. Ionized and molecular gas both show enhanced gas dispersion along the SE-NW direction.

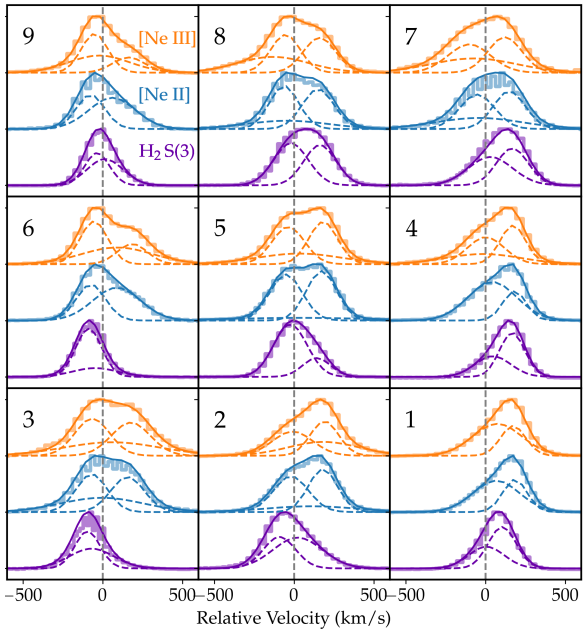


Fig. 6: Line profiles of [Ne III], [Ne II] and H_2 0-0 S(3) extracted from the nine regions defined in Section 3.1.3 and shown in Figure 5. Profiles are normalized by the peak flux density and offset vertically for better visual distinction, with best-fit model and components shown in solid and dashed lines. Broad wings are seen across most regions in the neon lines but not in H_2 0-0 S(3), which also has overall narrower profiles.

Buiten et al. in prep.). We leave more comprehensive coronal line identification and characterization to future work (U et al. in prep.) and focus only on the [Ne V] 14 μm line in further analysis (see Section 4.3). In Figure 4 we show the line profiles and best-fit models of several emission lines from the nuclear spectrum, i.e., extracted from the conical aperture as defined in Section 3.1.1. The best-fit parameters and the corresponding uncertainties from `lmfit` for all emission lines identified in the nuclear and central spectra are listed in Table D.1. Most ionized gas tracers show clear double-peaked profiles, with many showing a third broad component with FWHM > 500 km s^{-1}. While some H_2 lines also show signs of multiple kinematic components, they generally lie close to the expected velocity and have relatively narrow line widths with FWHM $\lesssim$ 300 km s^{-1}. We note that, unless otherwise specified, we do not apply the MIR attenuation derived from `CAFE` to the MIR line fluxes reported throughout this work, given that PAH, ionized and molecular gas have different physical origins and spatial distributions as shown in spatially-resolved multi-wavelength studies of nearby galaxies (e.g., Tielens 2008; Egorov et al. 2025).

3.1.3. Emission line maps & additional spectral fits

To visualize the spatially-resolved gas distribution and kinematics, we further generate flux, velocity and FWHM linewidth maps of the emission lines via performing, on each spaxel, the same line fitting procedure as described in Section 3.1.2 with `lmfit`. Even for the brightest lines, the per-spaxel level signals are insufficient for robust characterization with more than one Gaussian component across the FoV of the *MRS* channel cubes, therefore we show examples of the resulting maps from single-Gaussian fitting, for [Ne III], [Ne II] and H_2 0-0 S(3) in Figure 5. The warm molecular gas as traced by the H_2 0-0 S(3) line, shows extended "X"-shaped structures on ∼ 5 kpc scales, while

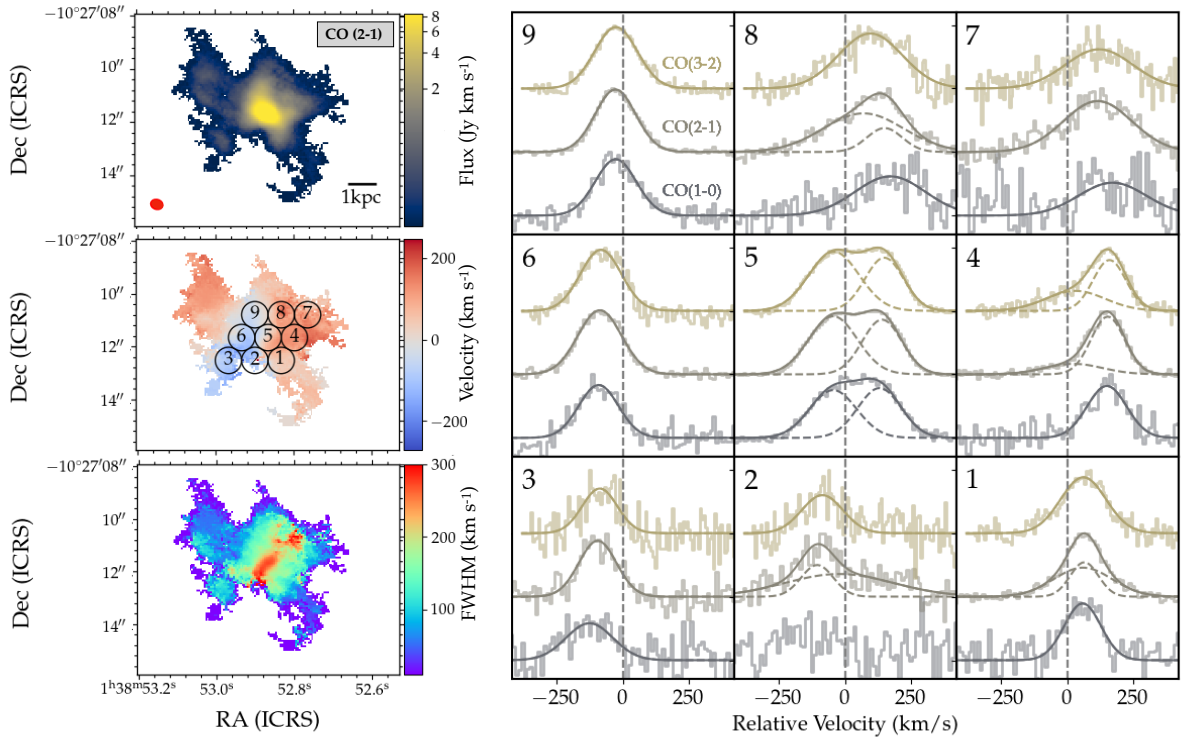


Fig. 7: Spectral analysis of the ALMA datasets. *Left:* Moment maps of integrated flux, velocity and linewidth FWHM of the CO (J=2-1) emission, with the spectral extraction regions defined in Section 3.1.3 (same as in Figure 5) overlaid on the velocity map. The synthesized beam is indicated with a red ellipse in the lower left corner of the flux map. *Right:* Extracted line profiles of multi-J CO lines. Profiles are normalized by the peak flux density and offset vertically for better visual distinction, with best-fit model and components shown in solid and dashed lines. The cold molecular gas traced by CO (2-1) shows similar morphology and large-scale velocity gradient along E-W direction as the warm molecular gas (Figure 5). Line profiles are sufficiently characterized by a single component across most regions except for in region 5, where all three transitions show consistent, double-peaked profiles.

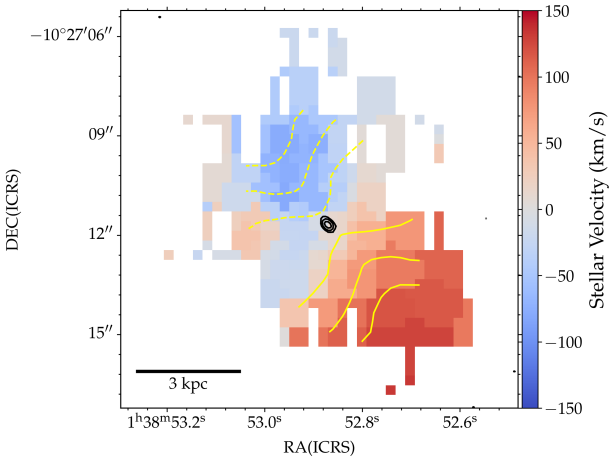


Fig. 8: Line-of-sight stellar velocity map derived from Keck/KCWI BH1L cube using `ppxf`. Only spaxels with stellar emission stronger than SNR > 5 (i.e., within the yellow contour in Figure 3) are shown. See Section 3.3 for details. ALMA 334 GHz continuum contours from Figure 2 are shown in black. The velocity field is reproduced by model of a rotating disk at inclination $i \sim 60°$ and position angle PA $\sim 220°$, shown in yellow contours, in levels of [40, 70, 90] km s^{-1}, with blue-shifted velocities shown in dashed lines (see Section 4.1).

the ionized gas traced by the neon lines appear mostly concentrated around the nucleus. The ionized and warm molecular gas also appear to move along perpendicular directions, as suggested by the velocity maps shown in the center column, while all gas tracers show broadened linewidths along the SE-NW direction. We elaborate on these findings in Section 4 and 5.

To investigate variations in the MIR spectral properties along the extended molecular emission, we perform additional spectral extractions and decomposition with `CAFE` in nine non-overlapping cylindrical apertures that cover the spatial extent of the H_2 0-0 S(3) emission. We set a uniform radius of 0.″5 for these apertures to ensure sufficient SNR for detailed spectral fitting of the emission line profiles while fully encompassing the PSF at the wavelength of the [S III] 18.7 μm line (FWHM $\sim$ 0.″86), which is the longest-wavelength emission line of interest. The regions defined by these apertures are also visualized in Figure 5, and are later referred to as regions 1 to 9, where region 5 is centered on the nucleus. To further compare the resolved kinematics between the ionized and warm molecular gas, in Figure 6 we show the line profiles (normalized by the peak flux density) and best-fit models for [Ne II], [Ne III] and H_2 0-0 S(3). We present the best-fit parameters of these emission line profiles in Table D.2, and the decomposed fluxes of the brightest PAH features from `CAFE` in Table B.2. Across regions 1 - 9, the H_2 0-0 S(3) line can be sufficiently modeled with two narrow components while the neon lines consistently show a broad component in region 2, 3, 5, 7, and 8, corresponding to the areas of

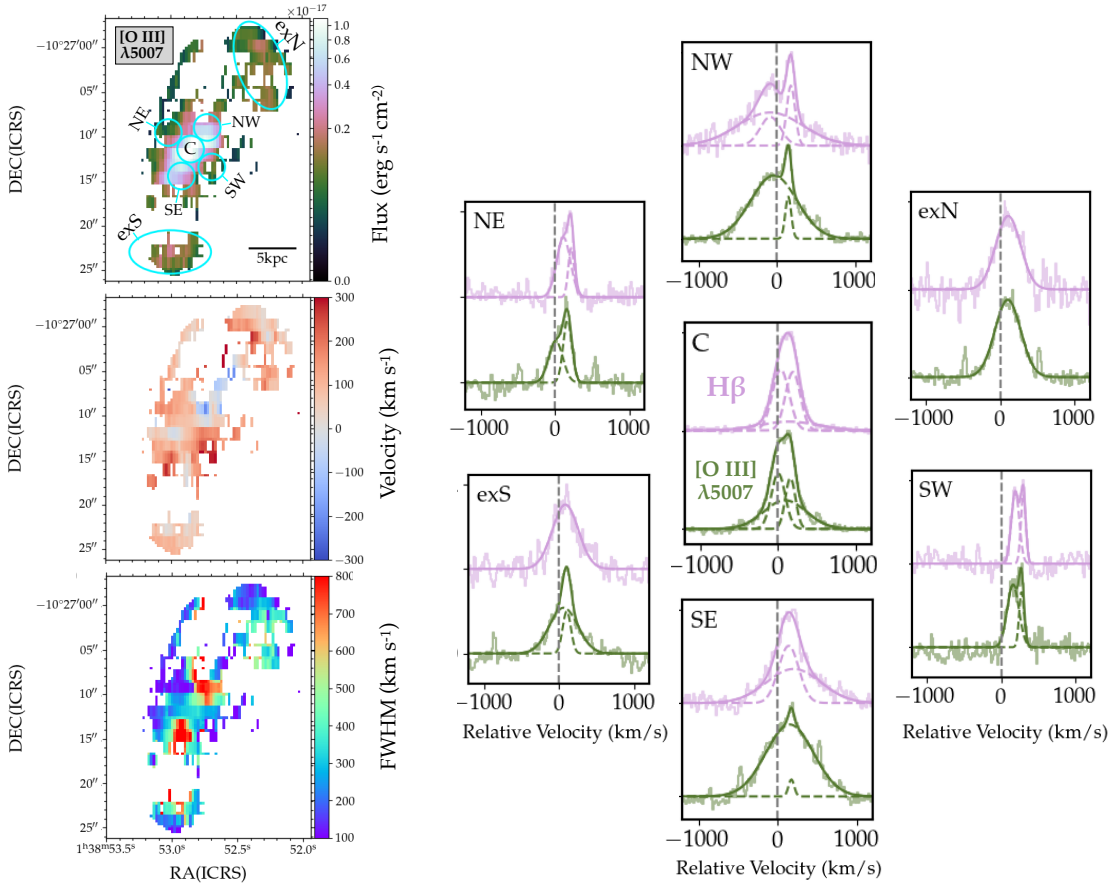


Fig. 9: Spectral analysis of the Keck/KCWI datasets. *Left:* Maps of integrated flux, velocity and linewidth FWHM of [O III]λ5007 emission, with the spectral extraction regions defined in Section 3.3 overlaid on the integrated flux map. *Right:* Extracted line profiles of Hβ and [O III]λ5007, normalized by the peak flux density and offset vertically for better visual distinction, with best-fit model and components shown in solid and dashed lines. The ionized gas as traced by [O III]λ5007 extends beyond $\sim$ 10 kpc from the nucleus along the SE-NW direction, with no clear sign of rotation in the central region as seen in the stellar kinematics (Figure 9). Line profiles of both Hβ and [O III]λ5007 exhibit broad wings along the SE-NW direction, i.e., kinematic minor axis of the central stellar disk.

enhanced gas dispersion from the emission line maps in Figure 5.

3.2. ALMA

To visualize the distribution and kinematics of the cold molecular gas, we generate moment 0, 1 and 2 maps from the calibrated ALMA CO cubes from Section 2.3, using the 3D source-finding tool `Duchamp` (Whiting 2012). As an example, in Figure 7 we show the maps for the CO (J = 2 - 1) emission at rest-frame frequency ($\nu_{\rm rest}$) of 230.538 GHz, which exhibits extended structures similar to those of H_2 0-0 S(3) emission (see Figure 5). To study the spatial variation of the cold molecular gas kinematics, we repeat the analysis described in Section 3.1.3 and extract and model the multi-J CO line profiles across regions 1 to 9. The results are also visualized in Figure 7, and best-fit values are presented in Table D.3, along with those obtained for region C, as defined in Section 3.1.1. The corresponding maps for CO (J = 1 - 0) at $\nu_{\rm rest}$ = 115.271 GHz, and CO (J = 3 - 2) at $\nu_{\rm rest}$ = 345.796 GHz, which are detected with overall lower SNR, are shown in Appendix A. All three CO lines are sufficiently modeled by a single Gaussian in most regions except for region 5.

3.3. KCWI

To properly recover the flux distribution and kinematics of the emission lines detected in each KCWI cube over the large FoV (e.g., Figure 3), we perform simultaneous modeling of the emission line profile and the underlying stellar continuum at each spaxel with `ppxf`. This is done in two stages: First, Voronoi binning is performed on each cube so that each bin reaches SNR of 60 for the brightest line detected within the wavelength range covered by the cube. We then fit the stellar spectrum at each bin after masking the emission lines. Afterwards, we repeat the fitting at each spaxel including both stellar and gas components, where the former is set by rescaling the best-fit stellar template derived for the corresponding Voronoi bin in the first stage, and the latter is modeled by a single Gaussian. At this stage, we set the initial guess for the gas velocities to the stellar velocity derived at each spaxel, and tie the kinematics of emission lines together to further reduce degeneracy, given that some lines are blended (e.g., [O II], [S II] doublets). In Figure 8 we show the stellar velocity field derived from the BH1L cube where the stellar features are most prominent. In Figure 9, we show the emission line maps for [O III]λ5007, which best showcase the large-scale kinematics of the extended ionized gas emission detected out to $\sim$ 10 kpc from the nucleus.

To investigate the ionized gas kinematics in more detail, we extract spectra from seven regions covering different parts of the ionized gas emission, which are respectively referred to by their locations as the "exS", "SE", "SW","C","NE", "NW", and "exN" regions, and illustrated in Figure 9. The "C" region was initially defined in Section 3.1.1. Region SE, SW, C, NE and NW are circular with radii of $r = 1\farcs5$ for matched-scale comparison across area of bright [O III]λ5007 emission, while region exS and exN are elliptical and larger, with semi-axes of $\sim 2\farcs5 \times 5''$, to encompass the fainter extended emission. We then conduct multi-component Gaussian fitting of the brightest emission lines detected in each spectrum following the same procedures described in Section 3.1.2, after fitting and subtracting the underlying stellar component with `ppxf` (see Figure 3 for examples). We set the line flux ratios of the [O III]λ5007/λ4959 and [N II]λ6584/λ6548 to the theoretical value of 3, and restrict those of the [O II]λ3729/λ3726 and [S II]λ6716/λ6731 to vary only between the theoretical limits of 0.38 - 1.45 and 0.44 - 1.45 (Sanders et al. 2016), respectively. The line profiles of [O III]λ5007 and Hβ extracted from all seven regions are shown in the right panels of Figure 9. We report the best-fit parameters of individual components for the [O III]λ5007 and Hβ lines in Table D.4. Both lines show prominent broad components with FWHM $\gtrsim$ 600 km/s in region C, SE and NW. Detailed modelling of the kinematics of other key diagnostic lines is challenging given either the much fainter emission (e.g., [O I]λ6300, [S II]$\lambda\lambda$6716,31) or heavily blended profiles (Hα and [N II]$\lambda\lambda$6548,84, [O II]$\lambda\lambda$3726,29), therefore we present only the total flux of these other lines in Table D.5.

4. Results

4.1. A Multi-phase Biconical Outflow

Despite the different gas phases and spatial scales probed by our multi-wavelength datasets, the emission line maps separately presented in Figure 5, 7 and 9 all exhibit consistent, prominent linewidth enhancement along the SE-NW direction, which is the kinematic minor axis of the stellar rotation shown in Figure 8. We model the observed stellar velocity field using ^{3D}Barolo (Di Teodoro & Fraternali 2015), and overlay the best-fit results in Figure 8, which yield disk inclination angle of $i \sim 60°$ and position angle PA$\sim 220°$. This indicates a highly-inclined stellar disk with a minor axis along SE-NW direction, which may also produce broadened linewidths in the gas tracers due to the large velocity gradient along the line-of-sight. However, the spectral analyses presented in Figure 6 and 9 reveal that the linewidth enhancement arises from the superposition of at least two distinct kinematic components at and beyond the nucleus. In particular, Figure 9 shows that, in regions SE and NW, both the [O III]λ5007 and Hβ lines exhibit a prominent, broad component with FWHM of $\gtrsim 700\,\mathrm{km\,s^{-1}}$ (see Table D.4), indicating highly turbulent ionized gas motion at $\sim$ 5 kpc away from the nucleus and beyond the bulk of the stellar content. This, combined with the biconical shape of the linewidth-enhanced regions from the multi-wavelength emission line maps, signifies the presence of a multi-phase biconical outflow along the SE-NW direction.

In the left panel of Figure 10, we show the line profiles of several gas tracers extracted from region C, which is covered by all our datasets. Similar to what is seen in the nuclear *MRS* spectrum (Figure 4), broad line wings indicative of outflowing gas are present in most ionized gas tracers but not the molecular ones, and the high-ionization [Ne V] 14μm line shows a distinct, red-shifted profile. These differences imply that they do not necessarily trace the same kinematic structure(s), despite being measured over the same spatial scale. We leave a more in-depth discussion of the origins of the observed line profiles in the central region to Section 5, where we further infer the energetics of the multi-phase gas involved in the biconical outflow.

In the central panel of Figure 10 we visualize the morphology of the multi-phase gas derived from the multi-wavelength datasets. The extended [O III]λ5007 emission unambiguously traces the ionized bicone along the SE-NW direction beyond the bulk of the stellar emission probed by *HST*. The warm and cold molecular gas traced by H_2 and CO both exhibit "X"-shaped morphology and outline the inner edges of the ionized bicone. Given that ALMA observations have a much larger FoV than those from *MRS*, the close spatial correspondence between H_2 and CO indicates that molecular gas is mostly concentrated at the base of the bicone, similar to what was found in the outflows of nearby starbursts (e.g., Leroy et al. 2015; Beirão et al. 2015; Bolatto et al. 2021). The brighter and more extended molecular emission in the NW indicates that it occupies the near-side. This is supported by the line profiles presented in Figure 6 and 9, where the ionized gas tracers consistently present blue-shifted broad wings in region 8 and NW, and red-shifted ones in region 2 and SE. We provide a sketch of the inferred outflow configuration in the right panel of Figure 10, where we also highlight the fact that dust is present in the bicone based on the prominent obscuration along the NW cone observed in the *HST* data shown in Figure 1. In the following Sections we present key results drawn from our analyses in Section 3 to characterize the spatially-resolved and integrated multi-phase ISM properties across IRASF01364 in the context of this newly discovered galactic outflow.

4.2. Dust Extinction

The non-uniform and extended distribution of dust and heavy nuclear obscuration are among the most defining features of the optical morphology of IRASF01364, as shown in Figure 1. We quantify the spatially-resolved variation in visual extinction using the Hα and Hβ line flux measured with the KCWI dataset (Table D.5) across the regions defined in Section 3.3 and shown in Figure 9. Following Fluetsch et al. (2021), we adopt the extinction law for actively star-forming galaxies from Calzetti et al. (2000) (i.e., $R_V = 4.05$), and assume the intrinsic Hα/Hβ ratio of 2.86 for Case B recombination with temperature of $T = 10^4$ K (Hummer & Storey 1987).

The resulting values are highest in region SW, covering a dusty tidal tail of the merger, with $A_V \sim 3.0$. Regions SE and C have consistent $A_V \sim 2.1 - 2.4$, while regions NW and exN have significantly lower values, with $A_V \sim 0.75 - 0.8$. Region exS has a high derived A_V of 2.67 ± 0.40, but the faint and highly blended Hα and [N II] doublet emission here may have biased the measured line ratio. These values further lend support to the picture presented Figure 10 where the NW cone lies on the near-side, and the SE cone on the far-side. The latter is much fainter due to heavier obscuration by the disk and/or other foreground materials associated with the tidal tail (Fluetsch et al. 2021). The high extinction in the SW region likely comes from a combination of pre-existing dusty gas in the tidal tail and partial obscuration by dust along the edges of the bicone.

To further quantify the level of dust obscuration at the nucleus, we measure the apparent depth of the silicate feature at 9.7 μm from the *MRS* spectra, defined as $s_{9.7} = \ln(f_{9.7}/C_{9.7})$, where $f_{9.7}$ is the flux density measured at 9.7 μm, and $C_{9.7}$ is

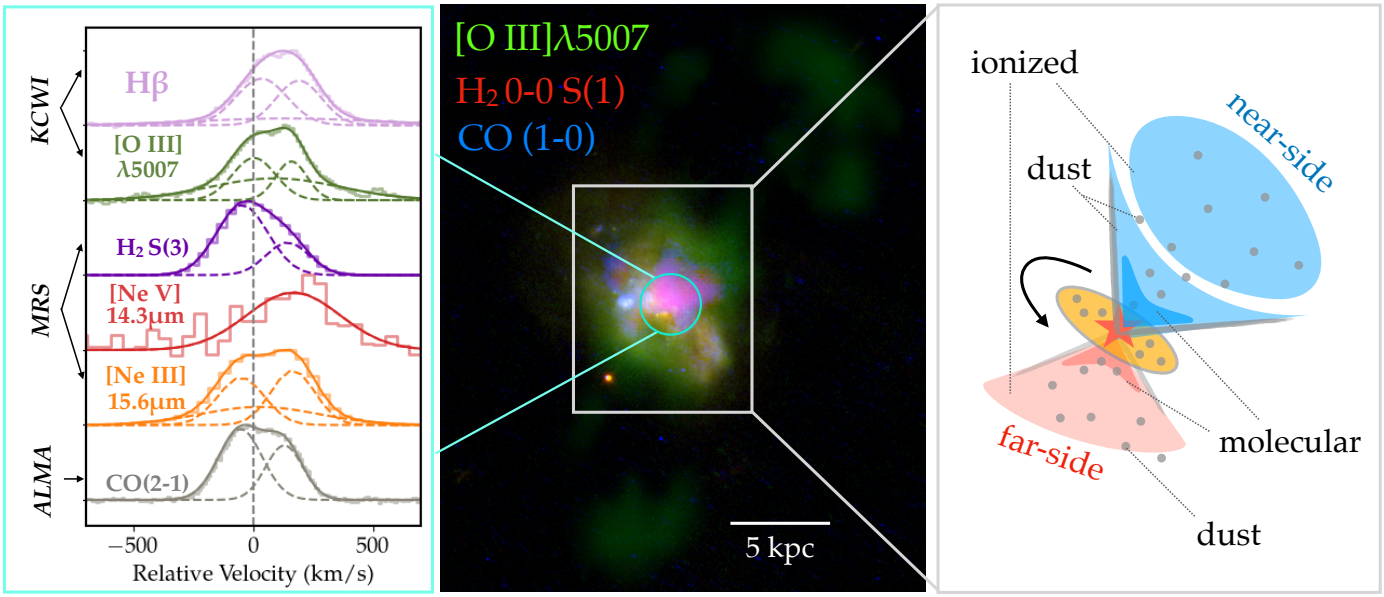


Fig. 10: Multi-phase gas morphology and kinematics derived from Keck/KCWI, *JWST/MIRI-MRS*, and ALMA data. *Left:* Comparison of line profiles of emission lines detected in the multi-wavelength datasets in the central 3 kpc in region C, defined in Section 3.1.1 (see also Figure 2). Profiles are normalized by the peak flux density and offset vertically for better visual distinction, with best-fit model and components shown in solid and dashed lines. *Middle:* Color-composite overlay of ALMA CO (1-0), *MRS* H_2 0-0 S(1) and Keck/KCWI [O III]λ5007 emission on top of the F336W/F435W/F814W tri-color *HST* image from Figure 1, showcasing the multi-phase biconical structure emerging from the dust-obscured nucleus of IRASF01364. The cyan ellipses highlight the regions defined in Section 3.3 for analyzing the large-scale ionized gas emission. *Right:* Simplified representation of the molecular and ionized outflow bicones with respect to the stellar disk (in yellow ellipse) and the nucleus (red star). The black curved arrow indicates the rotation of the stellar disk inferred from Figure 8. The cold and warm molecular gas are co-spatial and trace the inner edges of the ionized bicone, and appear brighter and more extended on the near-side NW cone.

the flux density of the underlying continuum at 9.7 μm, extrapolated with a power-law from 5 to 14 μm, following a method commonly adopted in the literature (e.g. Spoon et al. 2007; Stierwalt et al. 2013; Rich et al. 2023). The resulting $s_{9.7}$ values are −2.35, −2.12 and −1.66, in the expanding cone aperture, regions 5 and C, respectively. Compared to *Spitzer/IRS* measurements made with a $\sim 10'' \times 4''$ slit, which yield $s_{9.7} = -1.27$ for IRASF01364, and $s_{9.7} > -1.0$ for more than 60% of local LIRGs (e.g. Stierwalt et al. 2013), these values indicate highly concentrated dusty materials at the nucleus of IRASF01364. Following Chiar et al. (2007) and Güver & Özel (2009), these values indicate $A_V \gtrsim 60$ and column density of $N_{\rm H} \gtrsim 1.3 \times 10^{23}$ cm^{-2}. This result is consistent with the nuclear dust extinction derived by U et al. (2019) at 2.2 μm using Brγ/Brδ line ratios, which yield $A_V \sim 12 A_{2.2} \simeq 46 \pm 26.4$ assuming extinction law from Calzetti et al. (2000). The high uncertainties were due to faint Brδ emission. It is possible that the intrinsic nuclear extinction may be even higher, at up to $A_V \sim 200$ and $N_H \sim 5 \times 10^{23}$ cm^{-2}, as inferred from the high silicate optical depth ($\tau_{\rm sil} \sim 12$) obtained from `CAFE` (see Appendix B) assuming a mixed geometry (Marshall et al. 2007). However, potential degeneracy among the underlying multi-temperature dust model components could also impact the derived optical depths. Hence, we adopt the values derived from $s_{9.7}$ as the main reference for the nuclear extinction, as this quantity is measured directly from the observed spectrum, independent of assumptions about how multiple dust components and their associated opacities are distributed within the galaxy. Lastly, we highlight that the A_V derived from the KCWI spectrum of region C is more than 30 times lower, demonstrating the limitation of optical lines in probing the heavy nuclear obscuration in local LIRGs.

4.3. Detection of high IP lines

As shown in Figure 4 and 10, we detect the [Ne V] 14μm line with IP = 97 eV in both the nuclear and central *MRS* spectra, as well as [O IV] 26μm with IP= 55 eV (see Table D.1). This marks the first detections of high IP (> 50 eV) lines in IRASF01364. Previous non-detections with *Spitzer/IRS* (Petric et al. 2011; Inami et al. 2013) can likely be explained by a combination of spatial and spectral dilution, as well as limited sensitivity. As star formation does not provide sufficient energy to quadruply ionize Ne, the detection of [Ne V] on kpc-scales is generally considered as a strong evidence for AGN activity (e.g. Satyapal et al. 2007; Petric et al. 2011; Satyapal et al. 2021; Bierschenk et al. 2024). However, the [Ne V]/[Ne II] and [O IV]/[Ne II] ratios measured from the *MRS* spectra are low, at $\sim$ 0.005 and $\sim$ 0.2, respectively, which fall in the range previously measured among starburst-dominated local LIRGs with *Spitzer/IRS* (Petric et al. 2011; Inami et al. 2013; Pereira-Santaella et al. 2010). This indicates that the AGN does not contribute significantly to the ionized gas excitation at the nucleus, which is consistent with the low AGN fraction ($\sim$ 7%) derived from multi-wavelength nuclear SED fitting by Gao et al. (2025). We further discuss the properties of the putative AGN in Section 5.3 based on the [Ne V] 14μm detection.

We do not detect the [Ne V] 24μm line, and estimate a flux upper-limit of 5×10^{-19} W m^{-2} from three times the

root-mean-square of the nuclear spectrum measured around the expected redshifted wavelength (25.37 μm). This yields a lower-limit of $\sim$ 0.6 for the [Ne V]14μm/24μm ratio, which is widely adopted in AGN studies as a diagnostic of the electron density (e.g., Dudik et al. 2007; Pereira-Santaella et al. 2010; Ramos Almeida et al. 2025). However, our derived lower-limit is too low to yield any meaningful constraint on the electron density, which may range from $\lesssim$ 100 to up to 10^7 cm^{-3}, as shown by modelling results (e.g., Ramos Almeida et al. 2025). We also do not detect any high IP optical lines in the KCWI spectra, likely due to dust extinction (see Section 4.2). A more detailed *JWST* investigation of the high IP lines in a sample of local LIRGs including IRASF01364 will be presented in a future work (U et al. in prep.).

4.4. PAH Equivalent Width and Band Ratios

Broad emission features between 3 - 18 μm from PAH molecules mark the most common trait of MIR spectra of star-forming galaxies (Smith et al. 2007). These molecules trace small dust grains in the photodissociation regions (PDR; Bakes & Tielens 1994) and are sensitive probes of the radiation field and grain properties (e.g. Draine et al. 2021). In particular, the equivalent width (EW) of PAH features are observed to be lower in AGN environments (e.g., EW(PAH 6.2) < 0.27 μm; Stierwalt et al. 2013; Inami et al. 2018), due to dilution by the strong AGN continuum, and/or grain destruction by the harsh radiation field (Smith et al. 2007; Diamond-Stanic & Rieke 2010). As the 3.3 μm feature is not covered in our *MRS* dataset, we follow Stierwalt et al. (2013) and measure the apparent EW of the 6.2 μm PAH feature from the nuclear *MRS* spectrum, and from regions 5 and region C, using a spline fit of the local continuum. This yields a consistent value $\sim$ 0.29 – 0.33 μm across these different apertures, which is slightly lower than previous measurement with *Spitzer/IRS* (i.e., 0.39 μm) and still puts the nucleus among the class of composite sources (i.e., 0.27 < EW(PAH 6.2) < 0.54 μm), consistent with the scenario of a non-dominant AGN (see also Section 4.3).

PAH features are also detected across region 1 - 9, suggesting the potential presence of small dust grains outside the nucleus and in the outflow, which have been observed in several nearby galactic outflows (Sutter et al. 2025; Lopez et al. 2026) and predicted by simulation of multiphase outflow (Richie & Schneider 2026). In Figure 11 we show the PAH band flux ratios between 6.2 and 7.7 μm, and those between 11.3 and 7.7 μm, derived from `CAFE` fitting of the *MRS* spectra extracted from region 1 - 9 (see Appendix B). Region 3 and 7 are excluded as the 6.2 and 7.7 μm features are poorly constrained. Following Lai et al. (2022), we overlay theoretical tracks from Draine et al. (2021), which illustrate the utility of the 11.3/7.7 and 6.2/7.7 ratios as tracers of grain ionization state and size, respectively. While the 6.2/7.7 ratios for the extranuclear regions (in black) are roughly consistent within uncertainties between the observed (in triangles) and intrinsic (i.e., attenuation-corrected; in crosses) measurements, the former show significantly reduced 11.3/7.7 ratios indicating a higher fraction of ionized grains compared to the latter. This difference is even more prominent at the nucleus (i.e., region 5, in red). This is attributed to the large optical depth near the 11.3 μm band due to the deep 9.8 μm silicate absorption feature (Section 4.2). Hence, properly accounting for the effect of MIR attenuation is crucial for understanding dust grain properties in heavily-obscured centers of local LIRGs (Lai et al. 2024; Donnelly et al. 2025).

For comparison, we also overlay spatially-resolved measurements from two other local LIRGs, NGC 3256 (in circles for outflows and pink shaded area for star-forming regions; Bohn et al. 2024) and NGC 7469 (in squares; Lai et al. 2022), which were also obtained with `CAFE`. For all three systems, the AGN (in red symbols) show consistently lower 11.3/7.7 ratios than the non-AGN regions, indicating more ionized dust grains towards the AGN. The 6.2/7.7 ratios are generally higher in IRASF01364 than in the other two systems, potentially pointing to smaller grain sizes in the former. Considering the uncertainties, no clear differences in the 6.2/7.7 ratios are observed between the AGN and non-AGN regions in these systems.

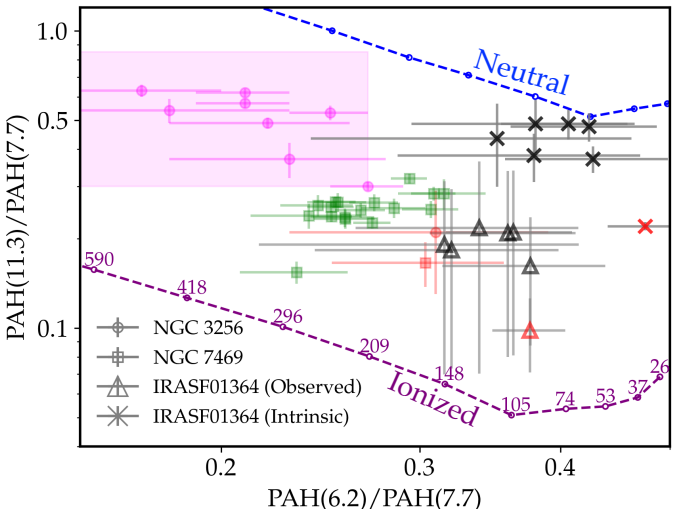


Fig. 11: PAH band ratios measured between the 11.3 and 7.7μm features with respect to the ones between 6.2 and 7.7 μm features, from region 1 - 9. Region 3 and 7 are not shown due to poor coverage of the 6.2 and 7.7 μm features. Observed and attenuation-corrected values are shown in triangles and crosses, respectively. Measurements for NGC 7469 from Lai et al. (2022) are shown in squares, and those for NGC 3256 from Bohn et al. (2024) are shown in circles and the pink shaded region. Red-colored symbols mark the AGN. Dashed lines mark the theoretical tracks from Draine et al. (2021) for neutral (blue) and ionized grains (purple) with varying numbers of carbon atoms (indicated in purple texts). Similar to the other two LIRGs, in IRASF01364, the dust grains are more ionized at the AGN than in the extranuclear regions. No clear differences in grain sizes are observed between the AGN and non-AGN regions.

4.5. Spatially-resolved ionized gas excitation

4.5.1. MIR

Following Inami et al. (2013), we utilize the [S IV]/[Ne II] vs. [Ne III]/[Ne II] ratios to investigate the ionized gas excitation across regions 1 - 9, shown in Figure 12. As [S IV] 10 μm, [Ne III] 15.6μm and [Ne II] 12.8μm have distinct IPs of 35, 41 and 22 eV, respectively, elevated [S IV]/[Ne II] and/or [Ne III]/[Ne II] ratios could be used to identify regions of high excitation. In the Figure we also show *Spitzer/IRS* measurements from Inami et al. (2013) for the GOALS sample in grey circles, with AGN-dominated systems outlined in red. Our spatially-resolved *MRS* measurements for IRASF01364 (in triangles) are consistent with previous unresolved measurement with *Spitzer/IRS* (marked in star) which did not detect the [S IV] 10 μm line. All regions show similarly low line ra-

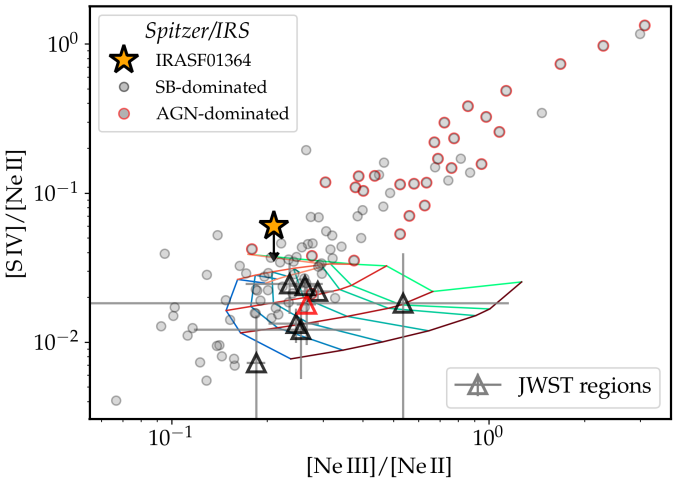


Fig. 12: [S IV]/[Ne II] vs. [Ne III]/[Ne II] ratios across region 1 - 9, shown in triangles. Region 5 (the nucleus) is colored in red. Region 7 is not shown due to poor detection of the [S IV] 10μm line. Measurements with *Spitzer/IRS* for the GOALS sample from Inami et al. (2013) are shown in grey circles, with AGN-dominated systems outlined in red. The star marks the *Spitzer/IRS* measurement for IRASF01364, where only an upper limit for [S IV]/[Ne II] was obtained. Model grids for fast radiative shock with solar metallicity and pre-shock electron density of 100 cm^{-3} (Allen et al. 2008; Sutherland et al. 2018) are overlaid in colored lines, with orange-brown lines representing shock velocities from 100 - 200 km s^{-1} and blue-green lines representing magnetic field strengths from 1 - 100 μG. All regions show line ratios similar to starburst-dominated systems, which are also consistent with the range predicted by models of fast radiative shock.

tios ([S IV]/[Ne II]~0.01, [Ne III]/[Ne II]~0.2) and overlap with starburst-dominated GOALS sources, with no clear differences between the nucleus and extra-nuclear regions. While in this work we do not apply MIR attenuation corrections to the atomic line fluxes, we note that such a correction would increase [S IV]/[Ne II] values by up to a factor of 2, which would still lie within the starburst-dominated regime.

As discussed in Inami et al. (2013), these low ratios could result from either photo-ionization by young starburst ($\lesssim$ 3.5 Myr) or shock excitation. For context, we emulate Inami et al. (2013) and overlay model grids of fast radiative shock from Allen et al. (2008), with shock velocity of 100 - 200 km s^{-1}, magnetic field strength of 1 - 100 μG, solar metallicity and pre-shock electron density of 100 cm^{-3}. The model grids were generated with the MAPPINGS V shock modelling code (Sutherland et al. 2018), which updates the calculation from Allen et al. (2008) with more realistic conditions, and were obtained from the Mexican Million Models Shock Database[10] (Alarie & Morisset 2019). Line ratios of all regions are within the range predicted by the shock model, suggesting that a dominant contribution from shocks across the central region of IRASF01364 is plausible.

4.5.2. Optical

To further investigate the excitation of large-scale ionized gas emission detected with KCWI, we construct the optical Baldwin–Phillips–Terlevich (BPT) diagnostic diagrams (Baldwin et al. 1981; Veilleux & Osterbrock 1987) using the observed [O III]/Hβ, [N II]/Hα, [O I]/Hα and [S II]/Hα line flux ratios for all spaxels with SNR > 5 detection in the [N II], [O I] and [S II] line, respectively, shown in Figure 13. Extinction correction is not applied here as its effect on the line ratios is expected to be trivial given the proximity in wavelengths between the emission line pairs, and also because not all regions have reliable A_V estimates (see Section 4.2). We classify and color-code each spaxel into "SF (star formation)" (blue), "composite" or "LINER" (low-ionization nuclear excitation region) (purple) and "Seyfert" (orange), following criteria presented by Kewley et al. (2006). The [O III]/Hβ vs. [N II]/Hα diagram also includes the empirical Seyfert/LINER demarcation by Schawinski et al. (2007). Measurements from individual regions defined in Section 3.3 are also shown (in circles), with region C colored in red.

A majority of the spaxels fall into the composite/LINER category in all three diagrams, which may be explained by a combination of several mechanisms including a low-luminosity AGN (Ferland & Netzer 1983), evolved stars (Binette et al. 1994) and shock ionization (Dopita & Sutherland 1995). The only region that falls into the Seyfert category in the [S II]/Hα diagram is region NW on the near-side outflow cone (see Figure 10), suggesting AGN excitation of the outflowing ionized gas. However, the observed Seyfert-like line ratios are also consistent with those predicted by the MAPPINGS V fast radiative shock model grids (see Section 4.5.1 and Figure 12) for shock velocities of $\sim$ 150−200 km s^{-1}. Overall, Figure 12 and 13 indicate that shock excitation is sufficient to explain the observed MIR and optical line ratios.

4.6. Multi-phase gas mass in the central region

While the multi-wavelength IFU datasets do not share the same FoVs, their common coverage in region C allow a matched-scale evaluation of the multi-phase gas content within the central $\sim$ 3 kpc of the system. In the following sections we derive the total multi-phase gas masses contained within region C based on the line fluxes measured in Section 3, without identifying their physical origins (disk rotation, outflow, etc.). This latter topic is discussed in detail in Section 5.1.

4.6.1. Ionized gas

After correcting for the visual dust extinction estimated in Section 4.2, the [O III]λ5007 and Hβ line luminosities are (4.9 ± 2.6) × 10^{40} erg s^{-1} and (5.3 ± 3.0) × 10^{40} erg s^{-1}, respectively. Given the measured [S II]λ6716/λ6731 line ratio ($\sim$ 1.38; Table D.5), the electron density at region C is $n_e \sim 50$ cm^{-3}. Assuming that the ionized gas fills the entire volume covered by region C, and a typical electron temperature of 10^4 K, the above values yield an ionized gas mass of (3.9±2.0) × 10^5 M$_\odot$ from [O III]λ5007 and (9.0 ± 5.1) × 10^6 M$_\odot$ from Hβ, following Eq.(5) and (7) in Carniani et al. (2015). It is possible that the electron density is underestimated when using the [S II]λ6716/λ6731 line ratio (e.g., Baron & Netzer 2019), in which case the values reported here would serve as upper limits. We note that the average flux ratios derived from all the KCWI apertures yield n_e values of 100 - 300 cm^{-3}, based on the prescription of Sanders et al. (2016) which is consistent with previous estimates for the GOALS galaxy sample using MIR [S III] 33.5/18.7 ratios observed with *Spitzer/IRS* (Inami et al. 2013) on similar physical

[10] http://3mdb.astro.unam.mx:3686/

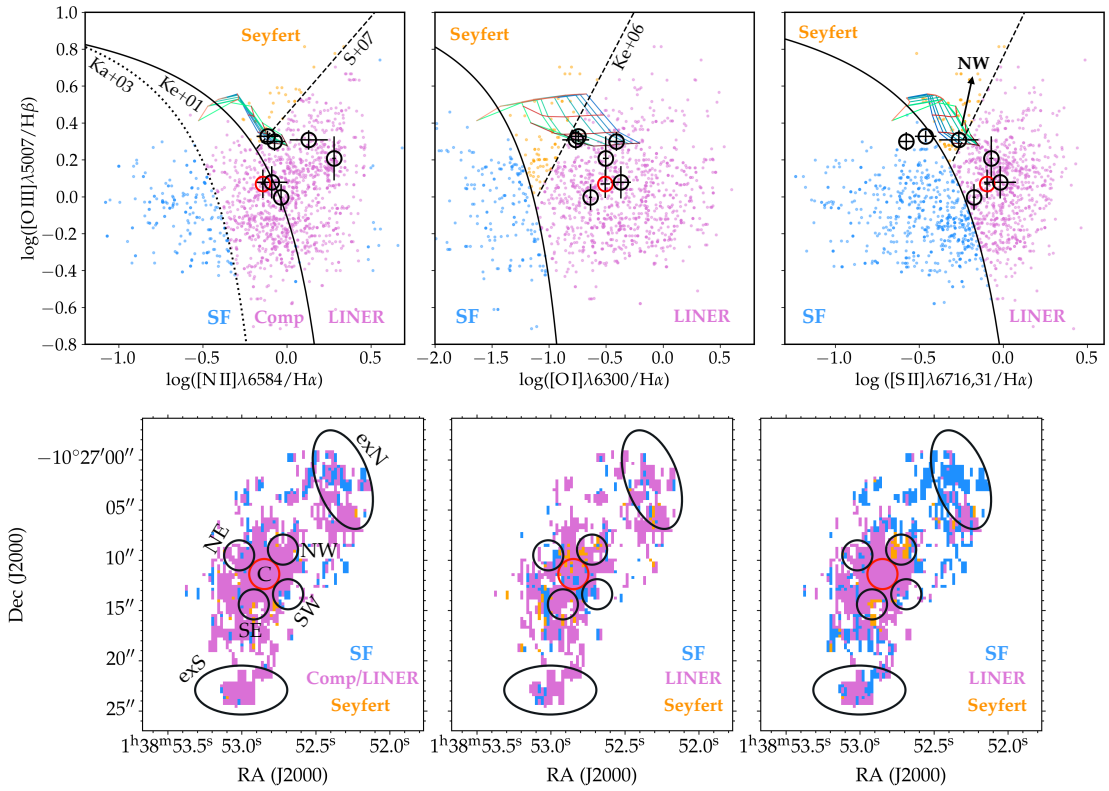


Fig. 13: Classification of the excitation mechanisms of the ionized gas in IRASF01364 based on the optical BPT diagrams (Baldwin et al. 1981; Veilleux & Osterbrock 1987) using log ([O III]λ5007/Hβ) vs. log ([N II]λ6584/Hα), log([O III]λ5007/Hβ) vs. log ([O I]λ6300/Hα), log([O III]λ5007/Hβ) vs. log ([S II]λ6716,31/Hα), from left to right, respectively. *Top*: measured line ratios at each spaxel are shown in blue, purple and orange, for classifications of "star formation", "composite/LINER", "Seyfert" excitation, respectively. The demarcation lines are defined by Kauffmann et al. (2003) (Ka+03), Kewley et al. (2001)(Ke+01), Schawinski et al. (2007) (S+07), and Kewley et al. (2006)(Ke+06). Model grids for fast radiative shock with the same parameters as in Figure 12 are overlaid. *Bottom*: spatial distribution of spaxels with different classifications. In all panels, circles mark measurements/locations of the regions defined in Section 3.3, with region C highlighted in red. Most optical line emission in the IRASF01364 can be attributed to composite/LINER excitation. Region NW shows Seyfert-like line ratios in the [S II]/Hα diagram, which may be due to AGN photo-ionization or shocks.

scales. Adopting this range of n_e would decrease the estimated ionized gas mass by a factor of 2 - 6.

4.6.2. Warm molecular gas

We use the nine rotational transitions of H_2 detected in the *MRS* spectrum to constrain the temperature and mass of the warm ($\gtrsim 100$ K) molecular gas within region C, by adopting the continuous power-law temperature model described in Togi & Smith (2016). The model is characterized by the lower and upper temperature limits (T_l, T_u) and the index (n) of the power-law distribution, and allows a smooth extrapolation between the transitions to recover the total molecular gas mass down to $\lesssim$ 100 K. In Figure 14, we show the best-fit model with T_u set to 5000 K following Bohn et al. (2024), for the extinction-corrected measurements (in crosses) that yields $T_l \simeq 243 \pm 3\,K$ and $n = 5.36 \pm 0.02$. The spectral index is in the range of values derived for nearby star-forming galaxies by Togi & Smith (2016), but somewhat steeper than previously derived in local LIRGs on global scales (Zakamska 2010; Pereira-Santaella et al. 2014), suggesting a relatively higher contribution from colder gas components in IRASF01364. However, these values are similar to those derived by Bohn et al. (2024) in the resolved nuclear outflows of NGC 3256. We note that using observed values without correcting for MIR attenuation (shown in triangles) does not affect the derived values, as the correction only affects the H_2 0-0 S(3) line, as shown in Figure 14.

For comparison, we also show measurements from the nuclear conical aperture (circles) and region 5 (squares), which respectively show excess and deficit in emission from warmer components, particularly those traced by the S(6) to S(9) lines, compared to region C. This indicates that the warmer molecular gas components are mostly concentrated at the innermost area encompassed by region 5 and the short-wavelength portion of the nuclear conical aperture, while the colder components are more diffuse and fill the central few kpcs covered by region C. Accounting for the heavy element correction factor of 1.36, the best-fit model shown in Figure 14 yields a total warm ($T \gtrsim 240$ K) molecular gas of $M_{\mathrm{H_2,\,warm}} \simeq 3.4 \times 10^8\,\mathrm{M_\odot}$ and column density of $N_{\mathrm{H_2,\,warm}} \simeq 3.5 \times 10^{21}\,\mathrm{cm^{-2}}$ in region C.

4.6.3. Cold molecular gas

The main source of uncertainty in estimating the cold ($T \sim 10-100$ K) molecular gas mass from CO observations lies in the CO-to-H_2 conversion factor, α_{CO}, which has been shown to be

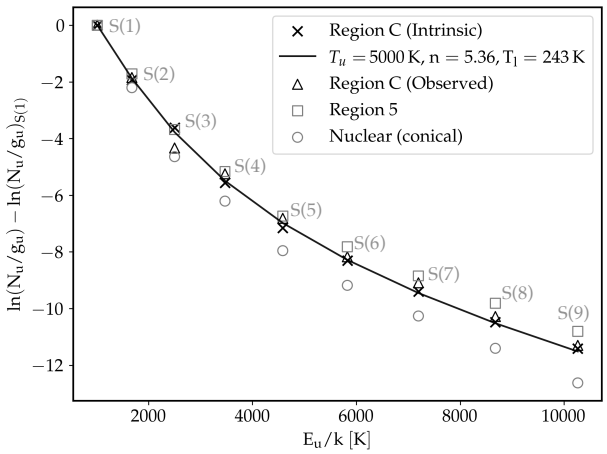


Fig. 14: H_2 excitation diagram and best-fit result assuming a continuous power-law temperature model as prescribed in Togi & Smith (2016), with an upper temperature limit set to 5000 K. Measurements from region C (Figure 9) are shown in triangles and crosses, for observed and extinction-corrected values, respectively. Extinction-corrected measurements from the nuclear region (Figure 2) and region 5 (Figure 2) are shown in empty gray circles and squares, respectively. Extinction correction mostly affects the measurement of the H_2 0-0 S(3) line. Compared to region C, region 5 shows somewhat higher contribution from S(6) - S(9) lines, while the nuclear (conical) region shows much lower contribution from S(3) - S(9) lines, indicating that the warmer molecular gas components are concentrated at the nucleus.

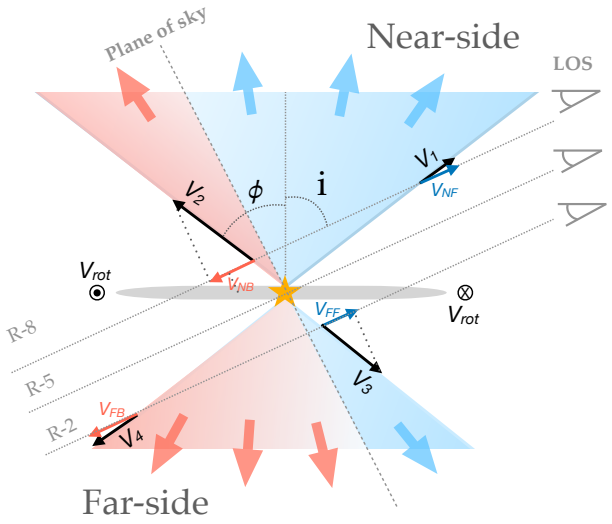


Fig. 15: Schematic of the kinematic model for the biconical outflow observed in IRASF01364, modified from Heckman et al. (1990) and Veilleux et al. (2001). The three gray dotted lines represent the potential lines-of-sight (LOS) towards regions 8, 5, and 2 (R-8, R-5, R-2) along the bicone, and the plane-of-sky is indicated by the dashed gray line. The yellow star and elongated ellipse respectively represent the nuclear starburst and the surrounding gaseous disk rotating at v_{rot}, viewed at an inclination angle i. The half opening angle the bicone is given by ϕ, and blue-shifted and red-shifted projected velocities are colored in blue and red, respectively. Each component is labeled based on the structure of origin (e.g. "NF" –"near-side cone, front wall", "FB" – "far-side cone, back-wall"). Deprojected velocities are colored in black.

environment-dependent (e.g., see review by Bolatto et al. 2013). The line ratios between different CO transitions offer clues on the physical condition of the molecular gas in different environments.

The CO line luminosity at each transition is given by Solomon et al. (1997):

$$\frac{L'_{\rm CO}}{\rm K\,kms^{-1}\,pc^2} = 3.25\times10^7 \frac{D_{\rm L}^2}{\nu_{\rm obs}^2(1+z)^3} S\Delta v \quad (1)$$

where the luminosity distance $D_{\rm L}$ is in Mpc, the observed frequency $\nu_{\rm obs}$ is in GHz, and the integrated line flux $S\Delta v$ is in Jy km s^{-1}. The resulting line luminosities for region C in CO(1-0), CO(2-1) and CO(3-2) are (3.6±1.5)×10^9, (2.9±0.1)×10^9, (3.0±0.1)×10^9 K kms^{-1} pc^2, respectively, which yield line ratios of $r_{21} \sim 0.8$ (i.e., $L'_{\rm CO(2-1)}/L'_{\rm CO(1-0)}$), $r_{32} \sim 1.0$ and $r_{31} \sim 0.8$. These values are higher than those found in nearby disk galaxies (e.g. Leroy et al. 2022) but similar to global measurements for local U/LIRGs (Montoya Arroyave et al. 2023), potentially due to the outflow reducing the CO optical depth. Hence we adopt the constant CO-to-H_2 conversion factor of $\alpha_{\rm CO} \sim 1.7 \pm 0.5\,M_\odot/({\rm K\,km\,s^{-1}\,pc^2})$ for CO (1-0) from Montoya Arroyave et al. (2023) based on calibration using neutral carbon [C I] measurements, which yield cold molecular gas mass of $M_{\rm H_2,cold} \sim (6\pm3)\times10^9\,M_\odot$. This value is also consistent with the total mass estimated from single-dish CO(1-0) measurements by Herrero-Illana et al. (2019) using a similar $\alpha_{\rm CO}$, indicating that most of the molecular gas in IRAS F01364 is concentrated in the central few kpcs. Roughly half of this mass is contained within region 5, which is three times smaller than region C in radius. The inferred gas column densities within regions C and 5 are $(6\pm3)\times10^{22}$ cm^{-2} and $\sim 3\times10^{23}$ cm^{-2}, respectively. These values are about 10 times higher than those inferred for the warm molecular gas from rotational H_2 lines in the last Section.

5. Discussion

5.1. Identifying the kinematic components of the outflow

As mentioned in Section 4.1, the diversity and complexity of line profiles of multi-phase gas tracers observed in region C (Figure 10) indicates that they may originate from different kinematic features. This is also hinted at in Figure 5 where we observe different morphologies and velocity gradients between the ionized gas traced by the MIR neon lines and warm molecular gas traced by the H_2 emission. In this Section we attempt to provide a coherent picture to interpret the various line profiles observed across the different gas phases in the central 3 kpc of IRASF01364, in the context of the newly uncovered multi-phase outflow (see Section 4.1) and similar biconical outflows described in the literature.

As highlighted in Figure 10, nearly all multi-wavelength gas tracers in the spectrum of region C feature a similar double-peaked line profile. These profiles have also been commonly observed in biconical outflows of nearby starburst galaxies (e.g., M 82, NGC 253, NGC 2992; Heckman et al. 1990; Shopbell & Bland-Hawthorn 1998; Veilleux et al. 2001; Leroy et al. 2015), and are attributed to the superposition of the nuclear disk and/or walls of the bicone along a tilted line-of-sight (LOS). To interpret the potential origins of the observed multiple kinematic components, in Figure 15 we provide a modified version of the schematic presented by Heckman et al. (1990), based

on the outflow configuration inferred previously in Section 4.1 and focusing on the LOS towards regions 8, 5 and 2 (hereafter as R-8, R-5 and R-2) along the bicone.

5.1.1. Outflow velocities

As discussed in Heckman et al. (1990) and illustrated in Figure 15, gas flowing along the front and back walls of a biconical outflow from a inclined disk would naturally produce two distinct narrow kinematic components along the LOS, at red-shifted and blue-shifted projected velocities, respectively. For example, along R-8 through the near-side NW cone, we would observe two velocity components coming from the front and back wall, respectively, at $v_{NF} = v_1 \cos(i - \phi)$ (NF - "near-side, front wall") and $v_{NB} = v_2 \cos(i + \phi)$ (NB - "near-side, back wall"), where v_1 and v_2 are the intrinsic velocities at the observed location, i is the inclination of the nuclear disk, and ϕ is the half opening angle of the near-side cone. Similarly, we may observe two components at $v_{FF} = v_3 \cos(i + \phi)$ (FF - "far-front") and $v_{FB} = v_4 \cos(i - \phi)$ (FB - "far-back") for the far-side SE cone at R-2, in the simplistic case that the bicone is perfectly symmetrical.

Now focusing on the observed MIR neon line profiles (see Figure 6), if we assume that the two narrow components observed in R-8 and R-2 originate from outflowing gas along the walls, from Table D.2 we then have $|v_{NF}| \simeq 60\,\mathrm{km\,s^{-1}}$, $|v_{NB}| \simeq 150\,\mathrm{km\,s^{-1}}$, $|v_{FF}| \simeq 10\,\mathrm{km\,s^{-1}}$ and $|v_{FB}| \simeq 180\,\mathrm{km\,s^{-1}}$. We estimate $\phi \sim 40 - 50°$ from the FWHM linewidth map of [O III]λ5007 (Figure 9) based on the opening angle of the area with FWHM $\gtrsim 500\,\mathrm{km\,s^{-1}}$, and adopt $i \sim 60°$ derived from the stellar velocity field in Figure 8 (see Section 4.1). The resulting de-projected velocities would be $v_1 \sim 60\,\mathrm{km\,s^{-1}}$, $v_2 \sim 580\,\mathrm{km\,s^{-1}}$, $v_3 \sim 40\,\mathrm{km\,s^{-1}}$ and $v_4 \sim 190\,\mathrm{km\,s^{-1}}$. These values would suggest that the outflow is decelerating away from the disk in the near-side cone, but somehow accelerating in the far-side cone, which we consider unlikely as both sides should exhibit similar behavior.

Given the clear rotation pattern seen in the stellar emission within the central 3 kpc, it is possible that gas rotating with the stellar disk at a velocity $v_{\rm rot}$ also contributes to the observed line profiles. As shown in Figure 8, such rotation produces blue-shifted narrow component towards the disk far-side (DF), and red-shifted narrow component towards the disk near-side (DN), with $v_{DF} = v_{DN} = v_{\rm rot} \sin i$ assuming the gaseous disk is symmetric. In this case, the blue-shifted narrow component in R-8 indicates $|v_{DF}| \simeq 60\,\mathrm{km\,s^{-1}}$, and the red-shifted narrow component in R-2 indicates $|v_{DN}| \simeq 180\,\mathrm{km\,s^{-1}}$, which are also consistent with the narrow components observed in R-5. The much higher value of $|v_{DN}|$ could result from the LOS intercepting the disk near the edge in R-2 compared to R-8, yielding $v_{\rm rot} \sim 200\,\mathrm{km\,s^{-1}}$.

While the above scenarios have attributed the narrow components distinctly to either gas flowing along the walls of the outflow cones or that is rotating around the stellar disk, we note that realistically, they likely represent contributions from both structures, which would require high spatial and spectral resolution to disentangle. This is illustrated in Appendix E, where we perform kinematic modeling of the molecular gas disk on the CO(2-1) dataset, which has the highest spatial and spectral resolution among the multi-wavelength IFU datasets utilized in this work. This was done with ^{3D}Barolo, using disk inclination and position angle previously derived by Agostino et al. (2026) from ~10-pc resolution ALMA CO(2-1) observations of the nuclear molecular disk. We describe in more detail the procedures and results in Appendix E. The results shown in Figure E.1 highlights the challenge in robustly separating the outflow and disk components, which span the same velocity range. This is also seen in the emission line channels maps shown in Appendix F. For an example, the [Ne III] line, shown in Figure F.1, shows clear signature of disk rotation as the bright, compact nuclear emission moves from NE to SW from between ~ -300 to 300 $\mathrm{km\,s^{-1}}$. Meanwhile, extended fainter emission corresponding to the NW and SE cone also appear in these channels, and hence the narrow components associated with the walls of the outflow cones would be blended with the disk emission both spatially and spectrally, especially given the *MRS* spectral resolution of $\sim 120\,\mathrm{km\,s^{-1}}$ (in FWHM) at the observed wavelengths of [Ne III].

Nevertheless, the broad component with FWHM $\sim 600 - 1000\,\mathrm{km\,s^{-1}}$ consistently seen in R-2, R-5, R-8 in the ionized gas tracers (Table D.2) allows for a more definitive characterization of the outflow velocity in the ionized gas phase, given by $v_{\rm out,ion} = |v_{\rm broad}| + \mathrm{FWHM}_{\rm broad}/2 \sim 300 - 600\,\mathrm{km\,s^{-1}}$, following definitions commonly adopted in the literature (e.g., Rupke et al. 2005a; Fluetsch et al. 2021). For the CO lines, a broad component is detected along the bicone marginally in R-2 and more strongly in R-8 (see Figure 7 and Table D.3), which yield outflow velocity in the cold molecular gas phase of $v_{\rm out,cold\,H_2} \sim 200 - 300\,\mathrm{km\,s^{-1}}$. These values are in agreement with the fact that emission is seen along the bicone up to $\sim \pm 500\,\mathrm{km\,s^{-1}}$ in the [Ne III] channel maps in Figure F.1, but only up to $\sim \pm 200\,\mathrm{km\,s^{-1}}$ in the CO(2-1) channel maps shown in Figure F.2. For the H_2 0-0 S(3) line (Table D.2), no broad components are identified in any regions potentially due to insufficient spectral resolution (~ 90 km/s in FWHM). As the channel maps in Figure F.1 show emission up to $\sim \pm 350\,\mathrm{km\,s^{-1}}$ along the bicone, from which we adopt a warm molecular gas outflow velocity of $v_{\rm out,warm\,H_2} \sim 350\,\mathrm{km\,s^{-1}}$.

5.1.2. Molecular vs. ionized gas

As already highlighted in previous Sections, broad wings characterized by a FWHM linewidth of $> 500\,\mathrm{km\,s^{-1}}$ are seen consistently in both MIR neon lines in regions 2, 3, 5, 7, 8 (see also Table D.2) along the outflow direction, with the broadest component measured at the nucleus, reaching FWHM $\sim 1000\,\mathrm{km\,s^{-1}}$ in both region 5 and the nuclear aperture (see Table D.1). On larger scales, shown in Figure 10, the ionized gas emission traced by [O III]λ5007 and Hβ in regions NW and SE along the bicone are completely dominated by a broad component with FWHM $\sim 300-500\,\mathrm{km\,s^{-1}}$. In all these regions, the broad component exhibits consistent blue-shifted velocities towards the NW and red-shifted velocities towards SE, which we interpret as the presence of outflowing ionized gas in between the walls of the bicone.

As illustrated in Figure 15, outflowing materials traveling at a range of velocity inside the bicone would produce a broad component that is dominantly blue-shifted in the near-side cone seen at R-8 and region NW and red-shifted in the far-side cone seen at R-2 and region SE. Along a LOS closer to the nucleus (e.g., R-5 or region C), the superposition of materials flowing in opposite directions would produce a broad component near systemic velocity. This picture is consistent with what we observe in the ionized gas tracers, except for the [Ne V] 14μm line, which we discuss later in Section 5.1.3.

On the other hand, this broad component is largely absent in the molecular gas tracers, where the broadest component with FWHM of $\sim 300-500\,\mathrm{km\,s^{-1}}$ is detected only in CO (2-1) at R-8 and marginally at R-2. As discussed in Section 5.1.1, this likely indicates a slower outflow in the molecular gas phase, whose line profiles are not easily distinguishable from that of the disk.

In addition, as we illustrate in Figure 15, slow-moving molecular gas accumulating near the disk will produce dominantly red-shifted emission in the near-side cone and blue-shifted emission in the far-side cone, in contrast to what is seen in the ionized gas tracers. These predictions are in agreement with what is seen in the channel maps in Appendix F, and can be attributed to the tilted outflow cones resulting in LOS intercepting the NB and FF walls much closer to the disk than the NF and FB walls. As such, emission coming from the NB and FF walls will consistently dominate over those coming from molecular gas in the center of the outflow and along the NF and FB walls, due to the rapidly decreasing molecular gas density with elevation. This may also explain the prominent "X"-shaped morphology observed in the CO and H_2 lines (i.e., Figure 10, Figure F.1).

5.1.3. Kinematics of the [Ne V] 14μm line

As shown in Figure 4 and 10, unlike other ionized gas tracers, the [Ne V] 14μm line tracing the most highly-ionized gas only exhibits a single red-shifted narrow component at $\sim$ 180 km s^{-1} with FWHM $\sim$ 300 km s^{-1}. Similar profiles have been observed in optical studies of high IP lines in nearby AGN hosting radio jet (e.g., Rodríguez-Ardila et al. 2006, 2017), where the highly-ionized gas traces a dense energetic outflow and is driven mechanically by the jet. Extended coronal line emission associated with such jet-driven outflows have also been observed in [Ne V] with MRS in local Seyferts and quasars (Davies et al. 2024; Kader et al. 2026; Bianchin et al. 2026). While VLA observations at 15 and 33 GHz do not show evidence of a radio jet down to $\sim$ 100 pc scales (Barcos-Muñoz et al. 2017; Song et al. 2022), we cannot rule out the possibility of a small-scale one-sided jet (e.g., Mezcua & Prieto 2014) driving the observed red-shifted emission of [Ne V] 14μm. Alternatively, this component may trace highly-excited gas emanating from the inner NB wall of the biconical outflow, given that it shares similar velocity as the red-shifted narrow components seen in the other ionized gas tracers with lower IP. The $\sim$1.6 times higher [Ne V] 14μm line flux measured from region C compared to that from the nuclear spectrum (Table D.1) potentially indicates that the [Ne V] emission is extended. However, assuming the emission is unresolved and considering *MRS* aperture correction factor (1.13 from Argyriou et al. (2023)) given the aperture sizes specified in Section 3.1, the evidence for extended [Ne V] emission is marginal. A more detailed search and characterization of other tracers with similarly high IPs would be required to investigate the kinematics of the highly-ionized gas, which we defer to future works.

5.1.4. Potential contributions from the merger

Given the merger nature of IRASF01364, one may also question whether tidal effects play a role in driving the observed gas kinematics. For an example, the distinctly different velocity fields observed between the ionized and molecular may also result from disk counter-rotation/misalignment triggered by the merger (e.g., Lu et al. 2021). However, we highlight that the disk inclination and position angle derived from the stellar velocity field shown in Figure 10 are in agreement with those derived from previous 10 pc-scale observations of the nuclear ionized and molecular gas disks of IRASF01364 in Paα, rovibrational H_2, and CO(2-1) lines by Medling et al. (2015) and Agostino et al. (2026). Hence, there is no evidence of strong disk misalignment among stars, ionized and molecular gas.

Nevertheless, the effect of merger is clearly present, which manifests in the extended molecular loop and tail observed towards the NE and SW direction respectively in the CO (2-1) maps shown in Figure 7. The narrow, double-peaked profiles of [O III]λ5007 and Hβ in the NE and SW regions along the major axis of the stellar disk shown in Figure 9 likely result from overlapping emission between the disk and tidal features. However, given the consistent disk rotation observed in this work and previous high-resolution studies of the nuclear disk (i.e., Medling et al. 2015; Agostino et al. 2026), as well as broadened line profiles along the outflow direction observed across the multi-phase tracers, we argue that the multi-phase kinematics of the central 3 kpc of the system focused in this work are likely dominated by disk rotation and the outflow rather than tidal features.

5.2. Outflow Energetics

Following the scenario proposed above, in this Section, we aim to quantify the outflow properties, as measured mainly within the central $\sim$ 3 kpc of IRASF01364, i.e., in region C, where gas emission is the brightest across gas phases. This region also covers the bulk of the CO emission (e.g., see Figure A.1) tracing the cold molecular gas outflow, which dominates the total outflow energetics, as we show later in this Section. We follow Lutz et al. (2020) and Fluetsch et al. (2021) and define outflow properties (outflow dynamical time $\tau_{\rm dyn}$, mass outflow rate $\dot{M}_{\rm out}$, outflow kinetic energy $E_{\rm kin}$ and kinetic power $\dot{E}_{\rm kin}$) as follows:

$$\tau_{\rm dyn} = R_{\rm out}/v_{\rm out}$$
$$\dot{M}_{\rm out} = M_{\rm out}/\tau_{\rm dyn}$$
$$E_{\rm kin} = 0.5 M_{\rm out} v_{\rm out}^2$$
$$\dot{E}_{\rm kin} = 0.5 \dot{M}_{\rm out} v_{\rm out}^2$$

where $v_{\rm out}$ and $R_{\rm out}$ are the outflow velocity and radius. Unless otherwise noted, we adopt $R_{\rm out}$ to be the deprojected physical radius of region C, which is 1.6 kpc for a disk inclination of 60°. We discuss below the outflow properties inferred from different gas tracers.

Cold Molecular Gas: Via modeling the disk emission using ^{3D}Barolo, as shown in Appendix E, we estimate that the outflow may contributes $\sim$ 40% of the CO(2-1) emission captured in region C. This would yield an outflow mass in cold molecular gas of $M_{\rm out,cold\,H_2} \sim 1.2 - 3.6 \times 10^9$ M$_\odot$, based on the total cold molecular gas mass derived in Section 4.6.3. While we have adopted $\alpha_{\rm CO} = 1.7$ M$_\odot$ (K km s^{-1} pc^2)$^{-1}$ in Section 4.6.3, for the outflowing molecular gas this value may be much lower due to turbulence reducing the CO optical depth (e.g., Bolatto et al. 2013). Previous works on outflows in local LIRGs have commonly adopted $\alpha_{\rm CO} = 0.8$ M$_\odot$ (K km s^{-1} pc^2)$^{-1}$ (e.g., Cicone et al. 2014; Fluetsch et al. 2019), and an even lower value of $\sim 0.4 - 0.6$ M$_\odot$ (K km s^{-1} pc^2)$^{-1}$ has been estimated in the outflow of NGC 3256 from CO absorption features observed with *JWST/NIRSpec* by Pereira-Santaella et al. (2024). Adopting this latter value, and an outflow velocity of $v_{\rm out,cold\,H_2} \sim 200 - 300$ km s^{-1} estimated in Section 5.1.1, we then have $M_{\rm out,cold\,H_2} \sim 3 - 12 \times 10^8$ M$_\odot$ yr^{-1}, $\tau_{\rm dyn,cold\,H_2} \sim 5 - 8$ Myr, $\dot{M}_{\rm out,cold\,H_2} \sim 38 - 240$ M$_\odot$ yr^{-1}, $E_{\rm kin,cold\,H_2} \sim 0.1 - 1.1 \times 10^{57}$ erg and $\dot{E}_{\rm kin,cold\,H_2} \sim 0.5 - 6.8 \times 10^{42}$ erg s^{-1}.

Warm Molecular Gas: Following discussions in Section 5.1.1, we infer from the channel maps (i.e., Figure F.1) an outflow velocity in the warm molecular gas phase up to $v_{\rm out,cold\,H_2} \sim$

350 km s^{-1}. As detailed modelling of the disk emission is challenging given the relatively coarse spectral resolution, here we simply assume that the warm molecular gas also contributes $\sim$ 40% of the total H_2 emission captured in region C, following the distribution of the cold molecular gas traced by CO(2-1). This is based on the similar spatial distributions and velocity profiles observed between the warm and cold molecular gas tracers, shown in Figure 10. Following this assumption, we have $M_{\rm out,warm\,H_2} \sim 1.4 \times 10^8$ M$_\odot$ based on the total warm molecular gas mass derived in Section 4.6.2. The inferred outflow properties are $\tau_{\rm dyn,warm\,H_2} \sim 4.5$ Myr, $\dot{M}_{\rm out,warm\,H_2} \sim 31$ M$_\odot$ yr^{-1}, $E_{\rm kin,warm\,H_2} \sim 1.7 \times 10^{56}$ erg and $\dot{E}_{\rm kin,warm\,H_2} \sim 1.2 \times 10^{42}$ erg s^{-1}.

Ionized Gas: Following discussions in Section 5.1.1, we assume that the outflow is mainly traced by the broad components identified in the ionized gas tracers, which yields $v_{\rm out,ion} \sim 500 - 600$ km s^{-1} from [Ne II], [Ne III], [O III] and Hβ (Table D.1 and D.4). These broad components account for 20 - 50% of the total line fluxes of these tracers within region C, which correspond to an outflow mass in ionized gas of $M_{\rm out,ion} \sim 0.8 - 7.0 \times 10^6$ M$_\odot$ based on the total mass calculated in Section 4.6.1 from Hβ. The inferred ionized outflow properties are $\tau_{\rm dyn,ion} \sim 3$ Myr, $\dot{M}_{\rm out,ion} \sim 0.3 - 2.3$ M$_\odot$ yr^{-1}, $E_{\rm kin,ion} \sim 0.2 - 2.5 \times 10^{55}$ erg and $\dot{E}_{\rm kin,ion} \sim 0.2 - 2.6 \times 10^{41}$ erg s^{-1}. As discussed in Section 5.1.1, it is possible that the outflow walls also contributes, to some degree, to the narrow components observed in region C, in which case the estimated $\dot{M}_{\rm out,ion}$, $E_{\rm kin,ion}$ and $\dot{E}_{\rm kin,ion}$ may further increase by up to a factor of two. We note that while the ionized gas emission extends out to a projected distance of $\sim$ 10 kpc beyond the nucleus, it is unclear whether they belong to the same outflow structure, and hence not considered here.

The values calculated above together indicate that molecular gas, especially in the cold phase ($T \lesssim 100$ K), heavily dominates the mass and energetics of the galactic outflow in IRASF01364, consistent with conclusions drawn from previous multi-phase studies of outflows in other local U/LIRGs (Fluetsch et al. 2021). The values of the mass outflow rates and kinetic energies in the molecular phase are also comparable to values derived from previous studies (e.g. Cicone et al. 2014; Pereira-Santaella et al. 2018; Lutz et al. 2020; Fluetsch et al. 2021) of local U/LIRGs, with $\dot{M}_{\rm out}$ nearly 10 times higher than what is seen in nearby starbursts (e.g. Leroy et al. 2015; Krieger et al. 2019; Bolatto et al. 2021). However, the local U/LIRGs hosting $\dot{M}_{\rm out} > 100$ M$_\odot$ yr^{-1} in the sample of Lutz et al. (2020) all have a much higher AGN contribution to the bolometric luminosity (> 25%;) than IRASF01364 ($\sim$ 5 – 7%; Díaz-Santos et al. 2017; Gao et al. 2025). We note that the assumed CO-to-H_2 conversion factor has a key impact on the estimated energetics. Sensitive, multi-tracer observations will provide critical constraints on the derived outflow properties. We discuss the potential origin of this powerful outflow in Section 5.5.

5.3. A low-luminosity, dust-obscured AGN

The detection of [Ne V] 14.3μm line from *MRS* provides the first direct evidence of AGN activity in the nucleus of IRASF01364. The line flux measured from region C is $(4.5 \pm 0.8) \times 10^{-16}$ erg s^{-1} cm^{-2}, corresponding to an AGN bolometric luminosity of $L_{\rm bol} \simeq 1.2 - 1.8 \times 10^{43}$ erg s^{-1}, adopting calibrations by Satyapal et al. (2007) and Spinoglio et al. (2022). Using the relationship between [Ne V] 14.3μm and 2−10 keV luminosity obtained by Bierschenk et al. (2024), we expect intrinsic 2−10 keV luminosity of $L^{\rm int}_{\rm 2-10\,keV} \sim 2.1 \times 10^{42}$ erg s^{-1}. Given the observed 2−10 keV luminosity from *Chandra* is $L^{\rm obs}_{\rm 2-10\,keV} \sim 1.5 \times 10^{41}$ erg s^{-1} (Iwasawa et al. 2011), we estimate the obscuring column density $N_{\rm H}$ using RXTorusD (Ricci & Paltani 2023), a physical X-ray absorption and reflection model. We adopt a photon index of $\Gamma \sim 1.8$, typical for nearby AGN (Ricci et al. 2017b), which yields $N_{\rm H} \sim 1.6 \times 10^{23}$ cm^{-2}, indicating that the AGN is dust-obscured. Similar results are obtained by Torres-Albà et al. (in prep.) via direct modelling of the *Chandra* spectrum (Iwasawa et al. 2011). The inferred obscuring column density is consistent with nuclear obscuration derived from the 9.7 μm absorption feature (Section 4.2) and the gas column density from CO (Section 4.6.3), pointing to a potential shared origin, although the latter is highly dependent on the uncertain $\alpha_{\rm CO}$.

While dust-obscured AGN are frequently found in local gas-rich mergers (Ricci et al. 2017a; Koss et al. 2018; Ricci et al. 2021), the low inferred $L^{\rm int}_{\rm 2-10\,keV}$ makes IRASF01364 one of the few local IR-luminous mergers found so far to host a low-luminosity AGN with $L_{\rm 2-10\,keV} < 10^{43}$ erg s^{-1} (e.g. Ricci et al. 2021). The AGN also seems to play a minimal role in photo-ionizing the surrounding gas, based on the MIR and optical line ratios shown in Figure 12 and 13, consistent with the low bolometric AGN fraction ($\sim$ 7%) inferred from X-ray-to-mm SED fitting by Gao et al. (2025). Following Ricci et al. (2023), we infer an extreme obscuring column density of $\sim 10^{26}$ cm^{-2} from comparing the observed 2-10 keV emission to the ALMA 100 GHz flux ($\sim$ 2 mJy) measured on $\sim$ 300 pc-scale. While this may suggest a potentially more powerful AGN that is more obscured than inferred from the mid-IR, the starburst likely dominates both the X-ray and 100 GHz emission of IRASF01364, hence complicating the interpretation. Observations at much higher resolutions would be necessary to isolate emission from the low-luminosity AGN. Upcoming deep observations with *XMM-Newton* will also further shed light on the nature of the AGN (ID: 096261; PI: N. Torres-Albà).

Given a central blackhole mass of $\sim 10^8 - 10^9$ M$_\odot$ estimated from kinematic modelling (Medling et al. 2015; Agostino et al. 2026), the inferred Eddington ratio (i.e.,$\lambda_{\rm edd} = L_{\rm bol}/L_{\rm edd}$) would be extremely low $\lesssim 10^{-3}$, indicating highly-inefficient accretion. This agrees with the recent finding from Rieke et al. (2025) that most late-stage IR-luminous mergers appear to have low accretion rates, challenging the picture of a merger-quasar evolutionary sequence where the final phase of the gas-rich merger is characterized by the emergence of a highly accreting AGN (e.g. Hopkins et al. 2006). Continuous search with *JWST* in galaxy mergers will potentially uncover many more cases of low-luminosity AGN that do not dominate the excitation nor total energy budget of the system, as already suggested from previous surveys with *Spitzer* (e.g., Petric et al. 2011; Stierwalt et al. 2013; Inami et al. 2013) and *NuSTAR* (Ricci et al. 2021).

5.4. Star formation rate of the nuclear starburst

Due to the relative faintness of MIR hydrogen recombination lines, many studies have explored and advocated for the usage of other bright MIR features as extinction-free tracers of star formation rates (SFR), such as the [Ne II] 12.8μm and [Ne III] 15.6μm lines (e.g. Ho & Keto 2007; Inami et al. 2013; Zhuang et al. 2019; Whitcomb et al. 2020) and PAH features (e.g. Shipley et al. 2016; Xie & Ho 2019; Hernán-Caballero et al. 2020).

From the observed line flux measurements from region C reported in Table D.1, we derive a total SFR of $\sim 8 - 10$ M$_\odot$ yr^{-1} from [Ne II] and [Ne III], accounting for contribution from the AGN using the [Ne V] 14.3μm line, following calibrations provided in (Zhuang et al. 2019). The values derived from

observed fluxes of 6.2, 7.7 and 11.3 μm PAH features (Table B.1) based on prescriptions from Shipley et al. (2016) are lower, at $\sim 2-6\,M_\odot\,yr^{-1}$. Assuming Case B recombination (Hummer & Storey 1987), we derive SFR $\sim 4\,M_\odot\,yr^{-1}$ from the observed Pfα and Huα line flux, with Hα-based calibrations from Murphy et al. (2011). We note that the inferred intrinsic Hα luminosity is about 5 - 10 times higher than the extinction-corrected Hα luminosity calculated within region C from the KCWI datasets, further confirming the limitation of optical lines for probing the heavy nuclear obscuration in IRASF01364.

The general agreement between values derived from PAH and hydrogen recombination lines is expected as both prescriptions were calibrated on Hα measurements (Murphy et al. 2011; Shipley et al. 2016). The AGN and shock from the outflow may have played a role in reducing the PAH emission via destruction of small grains (Zhang et al. 2022; García-Bernete et al. 2024). Meanwhile, since both hydrogen recombination lines and neon lines trace the ionizing photon rates (Ho & Keto 2007; Murphy et al. 2011), the relatively lower values derived from the former are likely due to their faint emission blending partially with the underlying strong MIR continuum and PAH emission, hence we consider the estimates from the much brighter neon lines to be more reliable.

Previous studies of IRASF01364 based on high-resolution ($< 0\farcs1 = 90$ pc) NIR Brγ (U et al. 2019) and radio continuum observations (Barcos-Muñoz et al. 2017; Song et al. 2022) yield nuclear SFR of 50 - 60 $M_\odot\,yr^{-1}$, which is about five times higher than the estimates based on MIR neon lines. There are several potential causes for the discrepancy: First, the MIR lines may still suffer significant attenuation due to the heavy nuclear obscuration in IRAS F01364. If we were to assume that the wavelength-dependent attenuation derived from `CAFE` applies equally to PAH and ionized gas, the inferred intrinsic SFR from the neon lines would be $\sim 30\,M_\odot\,yr^{-1}$, which approaches the values reported in the literature. However, as we note in Section 3.1, it is unlikely that the PAH and ionized gas are subject to the same attenuation.

Alternatively, as shown in a recent work by Robinson et al. (2026) using results from radiative transfer modeling (Efstathiou et al. 2022), SFR calibrations based on MIR neon lines or PAH features measured in normal star-forming galaxies consistently underestimate the SFR for local ULIRGs by up to 1 dex, which is attributed to a distinct mode of star formation in these more extreme systems. This is also observed by Inami et al. (2013), who found that the neon line luminosities strongly correlate with the total IR luminosities at low IR luminosities but show clear deviation towards high IR luminosities. Applying the scaling relations derived by Robinson et al. (2026) (their Eqn. 34), we obtain from the [Ne II] line flux, a SFR of $\sim 40-50\,M_\odot\,yr^{-1}$ for the nuclear starburst, which is similar to values based on previous high-resolution NIR and radio continuum observations. Given that the total SFR of the system is $\sim 130\,M_\odot$ (Howell et al. 2010), and the nucleus dominates the MIR emission as shown in Figure 2, we hence adopt a nuclear SFR $\sim 40-60_\odot\,yr^{-1}$. A systematic, matched-resolution comparison among multi-wavelength SFR tracers across a range of nuclear environments in local LIRGs would further help elucidate the origin of the discrepancy identified in this work and the literature.

5.5. Connecting the outflow, AGN and nuclear starburst

As noted in Section 5.2, the total mass outflow rate and kinetic energy/power are dominated by those of the molecular gas phase, which are highly dependent on the unconstrained α_{CO} factor. This hinders a direct comparison among the energetics of the outflow, starburst, and AGN to infer the origin and driving mechanisms of the outflow. Nevertheless, we note that the outflow orientation along the galaxy minor axis and the derived outflow velocities (Section 5.1) match what is commonly observed in nearby starbursts (e.g. Leroy et al. 2015; Bolatto et al. 2021; Lamperti et al. 2022). Adopting the SFR estimated from previous high-resolution NIR and radio continuum observations of $40-60\,M_\odot\,yr^{-1}$, the kinetic power delivered by supernovae (SNe) from the nuclear starburst would be $\dot{E}_{kin,SN} = 7\times10^{41}(SFR/M_\odot\,yr^{-1}) \sim 4\times10^{43}\,erg\,s^{-1}$ (Veilleux et al. 2005), which is about two times higher than the estimated bolometric luminosity of the obscured AGN from Section 5.3. In addition to the mechanical energy ejected by SNe, the dusty compact starburst also provides ideal conditions for supplying strong IR radiation pressure that is efficient in driving the massive molecular outflow (e.g. Murray et al. 2005; Huang et al. 2020). Indeed, given a starburst radius of ~ 140 pc estimated from the radio continuum (Song et al. 2022), the inferred star formation rate surface density (Σ_{SFR}) would be $\gtrsim 10^3\,M_\odot\,yr^{-1}/kpc^2$, reaching the limit of radiation pressure supported maximal starburst (Barcos-Muñoz et al. 2017; Thompson et al. 2005). Thus, the combined power from SNe and radiation pressure from the optically thick starburst may be sufficient in driving the observed outflow with a total kinetic energy of $\dot{E}_{kin} = \dot{E}_{kin,ion} + \dot{E}_{kin,warm\,H_2} + \dot{E}_{kin,cold\,H_2} \sim 2-8\times10^{42}\,erg\,s^{-1}$, without evoking AGN contribution. The mass-loading factor, given by the ratio between the total mass outflow rate M_{out} ($\sim M_{out,warm\,H_2} + M_{out,cold\,H_2} \simeq 70-270\,M_\odot\,yr^{-1}$) and SFR, is about 1 - 5, which is also similar to those previously estimated in other starbursts (e.g., Leroy et al. 2015; Bolatto et al. 2013; Fluetsch et al. 2019).

On the other hand, as discussed by Cicone et al. (2014) and Lutz et al. (2020), AGN may still play a significant role in driving massive molecular outflows in starburst-dominated systems due to short-term AGN variability. Observational studies have shown that AGN power can vary rapidly, i.e., "flicker", over a timescale of $\sim 10^5$ yr (e.g., Schawinski et al. 2007; Keel et al. 2012), which is much shorter than the timescale of outflows and starbursts ($> 10^6$ Myr; e.g., Zubovas & Nardini 2020). A more active AGN in the past would also help explain the high SMBH mass measured from previous 10-pc scale studies (Medling et al. 2015; Agostino et al. 2026), given the low accretion level estimated in Section 5.3. In this scenario, AGN winds driven by powerful AGN activity in the recent past may have supplied significant energy to efficiently drive materials out of the disk. In addition, as predicted by simulations by Richings & Faucher-Giguère (2018a,b) for AGN with $10^{44-47}\,erg\,s^{-1}$, some molecular gas may have also formed in-situ in the shocked layer of the AGN wind with moderate outflow velocity of few $100\,km\,s^{-1}$, as the swept-up gas cools rapidly within ~ 1 Myr. The extended ionized gas emission detected in the KCWI datasets out to > 10 kpc beyond the nucleus (i.e., region exN and exS; Figure 9 and F.3) may be the relics of such AGN-driven wind. Alternatively, they may be tidal features photo-ionized directly by the powerful AGN, as have been observed in other interacting and merging galaxies (Keel et al. 2024; Finlez et al. 2025). However, the emission in exN and exS do not show clear signature of AGN photo-ionization from the BPT diagram in Figure 13, as commonly seen in "Extended Emission Line Regions" (EELRs) found in nearby quasars and active galaxies (e.g. Lintott et al. 2009; Keel et al. 2012; Sartori et al. 2016; Finlez et al. 2022; Venturi et al. 2023; Finlez et al. 2025, Bianchin et al. in prep.).

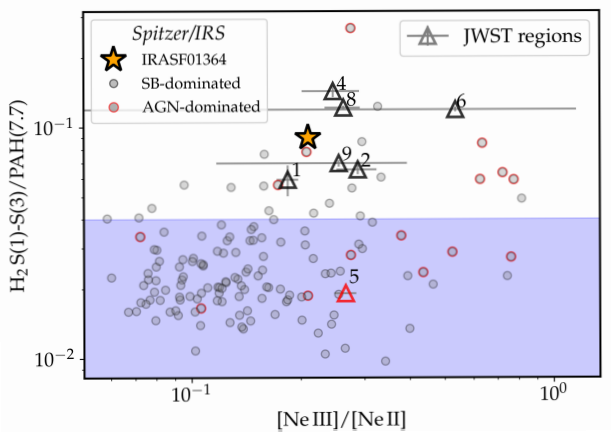


Fig. 16: Ratio between the summed fluxes of H_2,0-0 S(1) - S(3) and the 7.7 μm PAH feature, with respect to the [Ne III]/[Ne II] line flux ratio. Measurements from regions 1 - 9 are shown in triangles, and region 5 (the nucleus) is colored in red. Region 3 and 7 are excluded due to poor detection of the 7.7 μm PAH feature. Measurements with *Spitzer/IRS* for the GOALS sample from Inami et al. (2013) and Stierwalt et al. (2014) are shown in grey circles, with AGN-dominated systems outlined in red. Star marks the *Spitzer/IRS* measurement for IRASF01364. The purple shaded area indicate threshold from PDR modelling (Guillard et al. 2012). All extranuclear regions show excess H_2 emission consistent with previous *Spitzer/IRS* measurement but the nucleus show low H_2/PAH ratio consistent with prediction for PDR.

Hence, in the case that a more active AGN was present in the past, it likely did not reach sufficient power to dominate the overall gas excitation.

Regardless of the driving mechanisms, the MIR and optical diagnostics presented in Figure 12 and 13 suggests that shock associated with the outflow may be responsible for gas excitation throughout the system, which likely gives rise to the excess H_2 emission seen with *Spitzer/IRS* (Stierwalt et al. 2014). In Figure 16 we show the resolved measurements of the H_2/PAH ratio and [Ne III]/[Ne II] ratio from region 1 - 9, where we also overlay previous *Spitzer/IRS* measurement from Stierwalt et al. (2014) and Inami et al. (2013) for the GOALS sample (circles), including IRASF01364 (star). While measurements for the nuclear region (region 5) are consistent with the model-predicted limit for a photo-dissociation region (Guillard et al. 2012), marked in the shaded area, all extranuclear regions lie above this limit, and approach the values measured on the global scale. The H_2/PAH ratios also do not show clear dependence on the [Ne III]/[Ne II] ratio, indicating that the enhancement in H_2 is not related to the hardness of the radiation field due to the starburst/AGN. This provides a spatially-resolved confirmation that excess H_2 emission comes from shocked gas in the outflow rather than direct excitation from the starburst or AGN. In this regard, follow-up *MRS* observations of bright H_2 emitters identified by Stierwalt et al. (2013) will likely uncover many more cases of powerful galactic outflows such as the one in IRASF01364.

6. Summary

We combine IFU observations from *JWST-MIRI/MRS*, Keck/KCWI and ALMA to study the multiphase ISM properties in the late-stage merger and local LIRG IRAS F01364-1042. This system was initially highlighted by Stierwalt et al. (2013) due to its bright H_2 emission detected with *Spitzer/IRS*. The new, spatially resolved multi-wavelength datasets allow us to uncover and characterize, for the first time, a multi-phase galactic biconical outflow and a dust-obscured AGN in this starburst-dominated system. We summarize the main results as follows:

1. The key tracers of the ionized, warm, and cold molecular gas all show enhanced line width along the minor axis (SE-NW direction) of an inclined rotating stellar disk. The region of enhanced linewidths exhibits a clear biconical shape, signifying the presence of a multi-phase biconical outflow extending at least 5 kpc beyond the nucleus. Dust is present in the outflow, as visible from archival *HST* images, and from the derived visual extinction based on Hα/Hβ ratios measured from the KCWI datasets, which also supports a picture where the NW cone lies on the near-side, as inferred from the relatively stronger gas emission towards the NW direction.
2. The multi-phase gas exhibits different line profiles, with the ionized gas commonly showing a broad component with FWHM $>$ 500 km s^{-1}. We adopt a simplified kinematic model based on similar biconical outflows studied in the literature to explain the observed line profiles, which we attribute to the superposition of a gaseous nuclear disk and outflowing gas along the bicone. The molecular gas is likely more concentrated near the disk compared to the ionized gas, producing the apparent perpendicular motion observed between two. Based on this model, the observed line profiles and channel maps, we infer an outflow velocity of $\sim$ 500 - 600 km s^{-1}, $\sim$ 350 km s^{-1}, and $\sim$ 200 - 300 km s^{-1} in the ionized, warm, and cold molecular gas phase, respectively.
3. Focusing on measurements from the central $\sim$ 3 kpc, we infer $\sim$ 40 % flux contribution from the outflow, and estimate the multi-phase outflow energetics, which is heavily dominated by the cold molecular gas phase, similar to outflows found in other local LIRGs. We estimate a high cold molecular gas mass outflow rate of $\sim$ 38 - 240 $M_\odot$ yr^{-1}, and kinetic power of $\sim 0.5 - 6.8 \times 10^{42}$ erg s^{-1}, which are similar to those measured in AGN-dominated systems from the literature. However, these value are subject to high uncertainties related to the CO-to-H_2 conversion factor.
4. Detection of faint [Ne V] 14μm emission with *JWST/MRS* at the nucleus confirms, for the first time, the presence of a low-luminosity AGN in IRASF01364, which was suggested by previous multi-wavelength studies. From the observed [Ne V] 14μm flux we estimate an AGN bolometric luminosity of $L_{\rm bol} = 1.2 - 1.8 \times 10^{43}$ erg s^{-1}. Comparison between the observed and the inferred intrinsic X-ray luminosity suggests the AGN is dust-obscured with an obscuring column density of $N_H \sim 10^{23}$ cm^{-2}. The AGN is also accreting inefficiently based on the high SMBH mass estimated from previous 10-pc scale observations, indicating that the bulk of the SMBH growth took place in the past.
5. We estimate the SFR using MIR tracers measured on kpc-scales from the *JWST/MRS* dataset, and found lower values compared to previous NIR/radio continuum observations at higher resolution, potentially due to MIR attenuation or distinct physical conditions present in the compact nuclear starburst. Adopting the SFR from the latter, we estimate kinetic power from supernovae of $\sim 4 \times 10^{43}$ erg s^{-1}. Given the additional, high expected radiation pressure from the dusty starburst, star formation alone is sufficient for powering the observed powerful outflow. However, a more active AGN in

the recent past may also have played a role by enhancing the molecular gas content in the outflow and producing the bright excess H_2 emission in the MIR, as predicted by simulations. We confirm that the excess H_2 seen on global scale with *Spitzer/IRS* arises from outside the nucleus, likely a result from widespread shock associated with the outflow.

The results from this work highlight the importance of spatially-resolved multi-wavelength observations in investigating the nature of dust-obscured starbursts. In particular, we show that the ionized and molecular gas can have distinct behaviors, with ionized gas exhibiting stronger signatures of turbulence associated with the outflow, which may contribute to the differences observed between ionized and molecular gas tracers in dynamical studies of high−z star-forming galaxies (e.g., Rizzo et al. 2024). Additionally, we emphasize that in the case of IRASF01364, the molecular gas distribution and kinematics observed on kpc-scale does not solely trace disk rotation, and caution should be taken when interpreting the cold gas dynamics when information from other gas phases is not available. Last but not least, this work showcases the capability of *JWST/MRS* to unveil low-luminosity AGN hidden in dusty, starburst-dominated systems, which may represent a common phase in gas-rich galaxy mergers.

Acknowledgements. We would like to thank the anonymous referee for their thorough and constructive feedback that significantly improved the quality of this work. YS would like to thank F. Kemper, A. Prieto, A. Rodríguez Ardila and M. Romano for their helpful inputs on interpreting the PAH features, coronal line kinematics and AGN/outflow properties. VU and MB acknowledges funding support from the Space Telescope Science Institute program #JWST-GO-01717.001-A. VU acknowledges support from the National Science Foundation (NSF) Astronomy and Astrophysics Research Grant (AAG) #AST-2536603, NASA Astrophysics Data Analysis Program (ADAP) grant #80NSSC23K0750, and NASA Astrophysics Decadal Survey Precursor Science (ADSPS) grant #80NSSC25K0169. MB thanks the financial support of the IAU-Gruber Foundation Fellowship, and acknowledges support from the Juan de La Cierva scholarship with reference JDC2023- 052684 -I, funded by MICIU/AEI/10.13039/501100011033 y por el FSE+ and from the Agencia Estatal de Investigación of the Ministerio de Ciencia, Innovación y Universidades (MCIU/AEI) under the grant "Tracking active galactic nuclei feedback from parsec to kiloparsec scales", with reference PID2022−141105NB−I00 and the European Regional Development Fund (ERDF). ET acknowledges support from ANID through CATA-BASAL FB210003, and FONDECYT Regular 1241005 and 1250821. MSG and CML acknowledges that this research project was supported by the Hellenic Foundation for Research and Innovation (HFRI) under the "2nd Call for HFRI Research Projects to support Faculty Members & Researchers" (Project Number: 03382). TG acknowledges support from the Australian Research Council through Discovery Project DP210101945, funded by the Australian Government. DBS gratefully acknowledges support from NSF Grant 2407752. This work is based in part on observations made with the NASA/ESA/CSA James Webb Space Telescope. The data were obtained from the Mikulski Archive for Space Telescopes at the Space Telescope Science Institute, which is operated by the Association of Universities for Research in Astronomy, Inc., under NASA contract NAS 5-03127 for JWST. These observations are associated with program #GO-01717. This paper also makes use of the following ALMA data: ADS/JAO.ALMA#2017.1.01235.S, ADS/JAO.ALMA#2019.1.00811.S, 2018.1.00279.S. ALMA is a partnership of ESO (representing its member states), NSF (USA) and NINS (Japan), together with NRC (Canada), NSTC and ASIAA (Taiwan), and KASI (Republic of Korea), in cooperation with the Republic of Chile. The Joint ALMA Observatory is operated by ESO, AUI/NRAO and NAOJ. The National Radio Astronomy Observatory is a facility of the National Science Foundation operated under cooperative agreement by Associated Universities, Inc. Some of the data presented herein were obtained at Keck Observatory, which is a private 501(c)3 non-profit organization operated as a scientific partnership among the California Institute of Technology, the University of California, and the National Aeronautics and Space Administration. The Observatory was made possible by the generous financial support of the W. M. Keck Foundation. The authors wish to recognize and acknowledge the very significant cultural role and reverence that the summit of Maunakea has always had within the Native Hawaiian community. We are most fortunate to have the opportunity to conduct observations from this mountain.

References

Agostino, J., Medling, A. M., Barcos-Muñoz, L., et al. 2026, arXiv e-prints, arXiv:2601.16057
Alarie, A. & Morisset, C. 2019, Rev. Mexicana Astron. Astrofis., 55, 377
Albareti, F. D., Allende Prieto, C., Almeida, A., et al. 2017, ApJS, 233, 25
Allen, M. G., Groves, B. A., Dopita, M. A., Sutherland, R. S., & Kewley, L. J. 2008, ApJS, 178, 20
Argyriou, I., Glasse, A., Law, D. R., et al. 2023, A&A, 675, A111
Armus, L., Lai, T., U, V., et al. 2023, ApJ, 942, L37
Armus, L., Mazzarella, J. M., Evans, A. S., et al. 2009, PASP, 121, 559
Bakes, E. L. O. & Tielens, A. G. G. M. 1994, ApJ, 427, 822
Baldwin, J. A., Phillips, M. M., & Terlevich, R. 1981, PASP, 93, 5
Barcos-Muñoz, L., Aalto, S., Thompson, T. A., et al. 2018, ApJ, 853, L28
Barcos-Muñoz, L., Leroy, A. K., Evans, A. S., et al. 2017, ApJ, 843, 117
Baron, D. & Netzer, H. 2019, MNRAS, 486, 4290
Beirão, P., Armus, L., Lehnert, M. D., et al. 2015, MNRAS, 451, 2640
Bianchin, M., Ramos Almeida, C., González-Martín, O., et al. 2026, arXiv e-prints, arXiv:2604.08239
Bianchin, M., U, V., Song, Y., et al. 2024, ApJ, 965, 103
Bierschenk, M., Ricci, C., Temple, M. J., et al. 2024, ApJ, 976, 257
Binette, L., Magris, C. G., Stasińska, G., & Bruzual, A. G. 1994, A&A, 292, 13
Blecha, L., Snyder, G. F., Satyapal, S., & Ellison, S. L. 2018, MNRAS, 478, 3056
Bohn, T., Inami, H., Togi, A., et al. 2024, arXiv e-prints, arXiv:2403.14751
Boksenberg, A., Carswell, R. F., Allen, D. A., et al. 1977, MNRAS, 178, 451
Bolatto, A. D., Leroy, A. K., Levy, R. C., et al. 2021, ApJ, 923, 83
Bolatto, A. D., Wolfire, M., & Leroy, A. K. 2013, ARA&A, 51, 207
Bower, R. G., Benson, A. J., Malbon, R., et al. 2006, MNRAS, 370, 645
Briggs, D. S. 1995, PhD thesis, New Mexico Institute of Mining and Technology
Buiten, V. A., van der Werf, P. P., Viti, S., et al. 2024, ApJ, 966, 166
Bushouse, H., Eisenhamer, J., Dencheva, N., et al. 2023, JWST Calibration Pipeline
Calzetti, D., Armus, L., Bohlin, R. C., et al. 2000, ApJ, 533, 682
Cappellari, M. 2023, MNRAS, 526, 3273
Carniani, S., Marconi, A., Maiolino, R., et al. 2015, A&A, 580, A102
CASA Team, Bean, B., Bhatnagar, S., et al. 2022, PASP, 134, 114501
Cazzoli, S., Arribas, S., Maiolino, R., & Colina, L. 2016, A&A, 590, A125
Chiar, J. E., Ennico, K., Pendleton, Y. J., et al. 2007, ApJ, 666, L73
Cicone, C., Maiolino, R., Sturm, E., et al. 2014, A&A, 562, A21
Condon, J. J., Huang, Z. P., Yin, Q. F., & Thuan, T. X. 1991, ApJ, 378, 65
Conroy, C. & Gunn, J. E. 2010, ApJ, 712, 833
Conroy, C., Gunn, J. E., & White, M. 2009, ApJ, 699, 486
Cornwell, T. J. 2008, IEEE Journal of Selected Topics in Signal Processing, 2, 793
Davies, R., Shimizu, T., Pereira-Santaella, M., et al. 2024, A&A, 689, A263
Di Matteo, T., Springel, V., & Hernquist, L. 2005, Nature, 433, 604
Di Teodoro, E. M. & Fraternali, F. 2015, MNRAS, 451, 3021
Diamond-Stanic, A. M. & Rieke, G. H. 2010, ApJ, 724, 140
Díaz-Santos, T., Armus, L., Charmandaris, V., et al. 2017, ApJ, 846, 32
Diaz-Santos, T., Lai, T. S. Y., Finnerty, L., et al. 2025, CAFE: Continuum And Feature Extraction tool, Astrophysics Source Code Library, record ascl:2501.001
Donnelly, G. P., Lai, T. S. Y., Armus, L., et al. 2025, ApJ, 983, 79
Dopita, M. A. & Sutherland, R. S. 1995, ApJ, 455, 468
Draine, B. T., Li, A., Hensley, B. S., et al. 2021, ApJ, 917, 3
Dudik, R. P., Weingartner, J. C., Satyapal, S., et al. 2007, ApJ, 664, 71
Efstathiou, A., Farrah, D., Afonso, J., et al. 2022, MNRAS, 512, 5183
Egorov, O. V., Leroy, A. K., Sandstrom, K., et al. 2025, A&A, 703, A103
Ferland, G. J. & Netzer, H. 1983, ApJ, 264, 105
Ferrarese, L. & Merritt, D. 2000, ApJ, 539, L9
Finlez, C., Treister, E., Bauer, F., et al. 2022, ApJ, 936, 88
Finlez, C., Treister, E., Bauer, F., et al. 2025, arXiv e-prints, arXiv:2507.01115
Fluetsch, A., Maiolino, R., Carniani, S., et al. 2021, MNRAS, 505, 5753
Fluetsch, A., Maiolino, R., Carniani, S., et al. 2019, MNRAS, 483, 4586
Gaia Collaboration, Vallenari, A., Brown, A. G. A., et al. 2023, A&A, 674, A1
Gao, T., U, V., Auge, C. W., et al. 2025, ApJ, 988, 185
García-Bernete, I., Rigopoulou, D., Donnan, F. R., et al. 2024, arXiv e-prints, arXiv:2409.05686
Gardner, J. P., Mather, J. C., Abbott, R., et al. 2023, PASP, 135, 068001
Guillard, P., Boulanger, F., Pineau des Forêts, G., et al. 2012, ApJ, 749, 158
Güver, T. & Özel, F. 2009, MNRAS, 400, 2050
Heckman, T. M., Armus, L., & Miley, G. K. 1990, ApJS, 74, 833
Hernán-Caballero, A., Spoon, H. W. W., Alonso-Herrero, A., et al. 2020, MNRAS, 497, 4614
Herrero-Illana, R., Privon, G. C., Evans, A. S., et al. 2019, A&A, 628, A71
Hill, M. J. & Zakamska, N. L. 2014, MNRAS, 439, 2701
Hinshaw, G., Weiland, J. L., Hill, R. S., et al. 2009, ApJS, 180, 225
Ho, L. C. & Keto, E. 2007, ApJ, 658, 314
Hopkins, P. F., Cox, T. J., Hernquist, L., et al. 2013, MNRAS, 430, 1901
Hopkins, P. F., Hernquist, L., Cox, T. J., et al. 2005, ApJ, 630, 705

Hopkins, P. F., Hernquist, L., Cox, T. J., et al. 2006, ApJS, 163, 1
Howell, J. H., Armus, L., Mazzarella, J. M., et al. 2010, ApJ, 715, 572
Huang, X., Davis, S. W., & Zhang, D. 2020, ApJ, 893, 50
Hummer, D. G. & Storey, P. J. 1987, MNRAS, 224, 801
Inami, H., Armus, L., Charmandaris, V., et al. 2013, ApJ, 777, 156
Inami, H., Armus, L., Matsuhara, H., et al. 2018, A&A, 617, A130
Iwasawa, K., Sanders, D. B., Teng, S. H., et al. 2011, A&A, 529, A106
Kader, J. A., U, V., Barcos-Muñoz, L., et al. 2026, arXiv e-prints, arXiv:2601.08791
Kauffmann, G. & Haehnelt, M. 2000, MNRAS, 311, 576
Kauffmann, G., Heckman, T. M., Tremonti, C., et al. 2003, MNRAS, 346, 1055
Keel, W. C., Chojnowski, S. D., Bennert, V. N., et al. 2012, MNRAS, 420, 878
Keel, W. C., Moiseev, A., Uklein, R., & Smirnova, A. 2024, MNRAS, 530, 1624
Kewley, L. J., Dopita, M. A., Sutherland, R. S., Heisler, C. A., & Trevena, J. 2001, ApJ, 556, 121
Kewley, L. J., Groves, B., Kauffmann, G., & Heckman, T. 2006, MNRAS, 372, 961
Khalatyan, A., Cattaneo, A., Schramm, M., et al. 2008, MNRAS, 387, 13
Kim, D. C., Evans, A. S., Vavilkin, T., et al. 2013, ApJ, 768, 102
Koss, M. J., Blecha, L., Bernhard, P., et al. 2018, Nature, 563, 214
Krieger, N., Bolatto, A. D., Walter, F., et al. 2019, ApJ, 881, 43
Lai, T. S. Y., Armus, L., Bianchin, M., et al. 2023, ApJ, 957, L26
Lai, T. S. Y., Armus, L., U, V., et al. 2022, ApJ, 941, L36
Lai, T. S. Y., Smith, J. D. T., Peeters, E., et al. 2024, ApJ, 967, 83
Lamperti, I., Pereira-Santaella, M., Perna, M., et al. 2022, A&A, 668, A45
Larson, K. L., Díaz-Santos, T., Armus, L., et al. 2020, ApJ, 888, 92
Law, D., Diaz, R., Sosey, M., et al. 2025, JWST Pipeline Notebooks
Leroy, A. K., Rosolowsky, E., Usero, A., et al. 2022, ApJ, 927, 149
Leroy, A. K., Walter, F., Martini, P., et al. 2015, ApJ, 814, 83
Lintott, C. J., Schawinski, K., Keel, W., et al. 2009, MNRAS, 399, 129
Lopez, S., Ring, C., Leroy, A. K., et al. 2026, ApJ, 999, L7
Lu, S., Xu, D., Wang, Y., et al. 2021, MNRAS, 503, 726
Lutz, D., Sturm, E., Janssen, A., et al. 2020, A&A, 633, A134
Magorrian, J., Tremaine, S., Richstone, D., et al. 1998, AJ, 115, 2285
Marshall, J. A., Herter, T. L., Armus, L., et al. 2007, ApJ, 670, 129
McConnell, N. J. & Ma, C.-P. 2013, ApJ, 764, 184
McMullin, J. P., Waters, B., Schiebel, D., Young, W., & Golap, K. 2007, in Astronomical Society of the Pacific Conference Series, Vol. 376, Astronomical Data Analysis Software and Systems XVI, ed. R. A. Shaw, F. Hill, & D. J. Bell, 127
Medling, A. M., U, V., Guedes, J., et al. 2014, ApJ, 784, 70
Medling, A. M., U, V., Max, C. E., et al. 2015, ApJ, 803, 61
Mezcua, M. & Prieto, M. A. 2014, ApJ, 787, 62
Montoya Arroyave, I., Cicone, C., Makroleivaditi, E., et al. 2023, A&A, 673, A13
Morrissey, P., Matuszewski, M., Martin, D. C., et al. 2018, ApJ, 864, 93
Mould, J. R., Huchra, J. P., Freedman, W. L., et al. 2000, ApJ, 529, 786
Murphy, E. J., Condon, J. J., Schinnerer, E., et al. 2011, ApJ, 737, 67
Murray, N., Quataert, E., & Thompson, T. A. 2005, ApJ, 618, 569
Newville, M., Otten, R., Nelson, A., et al. 2025, LMFIT: Non-Linear Least-Squares Minimization and Curve-Fitting for Python
O'Sullivan, D. & Chen, Y. 2020, CWITools: Tools for Cosmic Web Imager data, Astrophysics Source Code Library, record ascl:2011.028
Patapis, P., Argyriou, I., Law, D. R., et al. 2024, A&A, 682, A53
Pereira-Santaella, M., Colina, L., García-Burillo, S., et al. 2018, A&A, 616, A171
Pereira-Santaella, M., Diamond-Stanic, A. M., Alonso-Herrero, A., & Rieke, G. H. 2010, ApJ, 725, 2270
Pereira-Santaella, M., González-Alfonso, E., García-Bernete, I., García-Burillo, S., & Rigopoulou, D. 2024, A&A, 681, A117
Pereira-Santaella, M., Spinoglio, L., van der Werf, P. P., & Piqueras López, J. 2014, A&A, 566, A49
Perna, M., Arribas, S., Pereira Santaella, M., et al. 2021, A&A, 646, A101
Petric, A. O., Armus, L., Howell, J., et al. 2011, ApJ, 730, 28
Ramos Almeida, C., García-Bernete, I., Pereira-Santaella, M., et al. 2025, A&A, 698, A194
Rau, U. & Cornwell, T. J. 2011, A&A, 532, A71
Ricci, C., Bauer, F. E., Treister, E., et al. 2017a, MNRAS, 468, 1273
Ricci, C., Chang, C.-S., Kawamuro, T., et al. 2023, ApJ, 952, L28
Ricci, C. & Paltani, S. 2023, ApJ, 945, 55
Ricci, C., Privon, G. C., Pfeifle, R. W., et al. 2021, MNRAS, 506, 5935
Ricci, C., Trakhtenbrot, B., Koss, M. J., et al. 2017b, ApJS, 233, 17
Rich, J., Aalto, S., Evans, A. S., et al. 2023, ApJ, 944, L50
Richie, H. M. & Schneider, E. E. 2026, ApJ, 996, 17
Richings, A. J. & Faucher-Giguère, C.-A. 2018a, MNRAS, 478, 3100
Richings, A. J. & Faucher-Giguère, C.-A. 2018b, MNRAS, 474, 3673
Rieke, G. H., Buiten, V. A., Goldberg, C. E., et al. 2025, ApJ, 988, 17
Rieke, G. H., Wright, G. S., Böker, T., et al. 2015, PASP, 127, 584
Rizzo, F., Bacchini, C., Kohandel, M., et al. 2024, A&A, 689, A273
Robinson, L., Farrah, D., Efstathiou, A., et al. 2026, ApJ, 999, 25
Rodríguez-Ardila, A., Prieto, M. A., Mazzalay, X., et al. 2017, MNRAS, 470, 2845
Rodríguez-Ardila, A., Prieto, M. A., Viegas, S., & Gruenwald, R. 2006, ApJ, 653, 1098
Rupke, D. S., Veilleux, S., & Sanders, D. B. 2005a, ApJ, 632, 751
Rupke, D. S., Veilleux, S., & Sanders, D. B. 2005b, ApJS, 160, 115
Rupke, D. S. N. & Veilleux, S. 2013, ApJ, 768, 75
Sanders, D. B. & Mirabel, I. F. 1996, ARA&A, 34, 749
Sanders, D. B., Soifer, B. T., Elias, J. H., et al. 1988, ApJ, 325, 74
Sanders, R. L., Shapley, A. E., Kriek, M., et al. 2016, ApJ, 816, 23
Sartori, L. F., Schawinski, K., Koss, M., et al. 2016, MNRAS, 457, 3629
Satyapal, S., Kamal, L., Cann, J. M., Secrest, N. J., & Abel, N. P. 2021, ApJ, 906, 35
Satyapal, S., Vega, D., Heckman, T., O'Halloran, B., & Dudik, R. 2007, ApJ, 663, L9
Schawinski, K., Thomas, D., Sarzi, M., et al. 2007, MNRAS, 382, 1415
Shipley, H. V., Papovich, C., Rieke, G. H., Brown, M. J. I., & Moustakas, J. 2016, ApJ, 818, 60
Shopbell, P. L. & Bland-Hawthorn, J. 1998, ApJ, 493, 129
Silk, J. & Rees, M. J. 1998, A&A, 331, L1
Smith, J. D. T., Draine, B. T., Dale, D. A., et al. 2007, ApJ, 656, 770
Solomon, P. M., Downes, D., Radford, S. J. E., & Barrett, J. W. 1997, ApJ, 478, 144
Song, Y., Linden, S. T., Evans, A. S., et al. 2022, ApJ, 940, 52
Spinoglio, L., Fernández-Ontiveros, J. A., & Malkan, M. A. 2022, ApJ, 941, 46
Spoon, H. W. W., Farrah, D., Lebouteiller, V., et al. 2013, ApJ, 775, 127
Spoon, H. W. W., Marshall, J. A., Houck, J. R., et al. 2007, ApJ, 654, L49
Springel, V., Di Matteo, T., & Hernquist, L. 2005a, ApJ, 620, L79
Springel, V., Di Matteo, T., & Hernquist, L. 2005b, MNRAS, 361, 776
Stierwalt, S., Armus, L., Charmandaris, V., et al. 2014, ApJ, 790, 124
Stierwalt, S., Armus, L., Surace, J. A., et al. 2013, ApJS, 206, 1
Sutherland, R., Dopita, M., Binette, L., & Groves, B. 2018, MAPPINGS V: Astrophysical plasma modeling code, Astrophysics Source Code Library, record ascl:1807.005
Sutter, J., Sandstrom, K., Chown, R., et al. 2025, ApJ, 992, L7
Thompson, T. A., Quataert, E., & Murray, N. 2005, ApJ, 630, 167
Tielens, A. G. G. M. 2008, ARA&A, 46, 289
Togi, A. & Smith, J. D. T. 2016, ApJ, 830, 18
Torres-Albà, N., Iwasawa, K., Díaz-Santos, T., et al. 2018, A&A, 620, A140
U, V., Lai, T., Bianchin, M., et al. 2022, ApJ, 940, L5
U, V., Medling, A. M., Inami, H., et al. 2019, ApJ, 871, 166
Vardoulaki, E., Charmandaris, V., Murphy, E. J., et al. 2015a, A&A, 574, A4
Vardoulaki, E., Charmandaris, V., Murphy, E. J., et al. 2015b, A&A, 574, A4
Veilleux, S., Cecil, G., & Bland-Hawthorn, J. 2005, ARA&A, 43, 769
Veilleux, S., Kim, D. C., Sanders, D. B., Mazzarella, J. M., & Soifer, B. T. 1995, ApJS, 98, 171
Veilleux, S., Meléndez, M., Sturm, E., et al. 2013, ApJ, 776, 27
Veilleux, S. & Osterbrock, D. E. 1987, ApJS, 63, 295
Veilleux, S., Shopbell, P. L., & Miller, S. T. 2001, AJ, 121, 198
Venturi, G., Treister, E., Finlez, C., et al. 2023, A&A, 678, A127
Wells, M., Pel, J. W., Glasse, A., et al. 2015, PASP, 127, 646
Whitcomb, C. M., Sandstrom, K., Murphy, E. J., & Linden, S. 2020, ApJ, 901, 47
Whiting, M. T. 2012, MNRAS, 421, 3242
Wyithe, J. S. B. & Loeb, A. 2003, ApJ, 595, 614
Xie, Y. & Ho, L. C. 2019, ApJ, 884, 136
Yuan, T. T., Kewley, L. J., & Sanders, D. B. 2010, ApJ, 709, 884
Zakamska, N. L. 2010, Nature, 465, 60
Zhang, L., Ho, L. C., & Li, A. 2022, ApJ, 939, 22
Zhuang, M.-Y., Ho, L. C., & Shangguan, J. 2019, ApJ, 873, 103
Zubovas, K. & Nardini, E. 2020, MNRAS, 498, 3633

[1] European Southern Observatory, Alonso de Córdova, 3107, Vitacura, Santiago, 763-0355, Chile
[2] Joint ALMA Observatory, Alonso de Córdova, 3107, Vitacura, Santiago, 763-0355, Chile
[3] Max-Planck-Institut für Radioastronomie, Auf dem Hügel 69, 53121, Bonn, Germany
[4] IPAC, California Institute of Technology, 1200 E. California Boulevard, Pasadena, CA 91125, USA
[5] Department of Physics and Astronomy, 4129 Frederick Reines Hall, University of California, Irvine, CA 92697, USA
[6] Instituto de Astrofísica de Canarias, Calle Vía Láctea, s/n, E-38205, La Laguna, Tenerife, Spain
[7] Departamento de Astrofísica, Universidad de La Laguna, E-38206, La Laguna, Tenerife, Spain
[8] Ritter Astrophysical Research Center and Department of Physics

and Astronomy, University of Toledo, Toledo, OH 43606, USA
[9] National Radio Astronomy Observatory, 520 Edgemont Road, Charlottesville, VA 22903, USA
[10] Department of Astronomy, University of Virginia, 530 McCormick Road, Charlottesville, VA 22903, USA
[11] Department of Astronomy, University of Geneva, Chemin Pegasi 51, 1290, Versoix, Switzerland
[12] Instituto de Estudios Astrofísicos, Facultad de Ingeniería y Ciencias, Universidad Diego Portales, Av. Ejército Libertador 441, Santiago, Chile
[13] Department of Physics & Astronomy, University of British Columbia, 6224 Agricultural Road, Vancouver, BC, V6T 1Z1, Canada
[14] Hiroshima Astrophysical Science Center, Hiroshima University, 1-3-1 Kagamiyama, Higashi-Hiroshima, Hiroshima 739-8526, Japan
[15] Occidental College, Physics Department, 1600 Campus Road, Los Angeles, CA 90042, USA
[16] Leiden Observatory, Leiden University, PO Box 9513, 2300 RA Leiden, The Netherlands
[17] Instituto de Alta Investigación, Universidad de Tarapacá, Casilla 7D, Arica, Chile
[18] European Space Agency, c/o STScI, 3700 San Martin Drive, Baltimore, MD 21218, USA
[19] Centre for Astrophysics Research, University of Hertfordshire, College Lane, Hatfield, AL10 9AB, UK
[20] Steward Observatory, University of Arizona, 933 North Cherry Avenue, Tucson, AZ 85721, USA
[21] School of Sciences, European University Cyprus, Diogenes Street, Engomi, 1516 Nicosia, Cyprus
[22] Institute of Astrophysics, Foundation for Research and Technology-Hellas (FORTH), Heraklion, 70013, Greece
[23] Department of Physics, University of Crete, Heraklion, 71003, Greece
[24] Department of Astronomy, University of Florida, P.O. Box 112055, Gainesville, FL 32611, USA
[25] Research School of Astronomy and Astrophysics, Australian National University, Weston Creek, ACT 2611, Australia
[26] ARC Centre of Excellence for All Sky Astrophysics in 3 Dimensions (ASTRO 3D); Australia
[27] W. M. Keck Observatory, Kamuela, HI, USA
[28] Institute for Astronomy, University of Hawaii, 2680 Woodlawn Drive, Honolulu, HI 96822, USA

Appendix A: Information on the ALMA datasets

We provide details on the ALMA observations used in this work in Table A.1, along with the characteristics of the reduced imaging products. The reduction and imaging procedures of these datasets are described in Section 2. Emission line maps for the CO (J = 2-1) line, which achieves the highest SNR, are shown in Figure 7. Maps for the CO (J = 1-0) and (J=3-2) lines are shown below in Figure A.1 for reference.

Table A.1: Information on ALMA observations and imaging products

Observations				
Project	PI	Band	MOUS	LAS
2017.1.01235.S	L. Barcos-Muñoz	3	uid://A001/X1292/X3a uid://A001/X1292/X3c	1.″26 8.″65
2019.1.00811.S	A. Medling	6	uid://A001/X1465/X228b uid://A001/X1465/X2285	3.″88 3.″92
2018.1.00279.S	L. Barcos-Muñoz	7	uid://A001/X13b3/X10c uid://A001/X1358/X39	1.″15 4.″24

Imaging Products				
Band	Target Emission	$\theta_M \times \theta_m$	PA (deg)	$\sigma_{\rm rms}$ (mJy/beam)
3	105 GHz Continuum	0.″37 × 0.″28	−74	0.03
	CO (J=1-0)	0.″35 × 0.″27	−73	0.54
6	228 GHz Continuum	0.″32 × 0.″27	40	0.05
	CO (J=2-1)	0.″42 × 0.″33	73	0.52
7	334 GHz Continuum	0.″18 × 0.″16	−60	0.20
	CO (J=3-2)	0.″44 × 0.″37	90	2.20

Notes. θ_M and θ_m are the major and minor axis length of the synthesized beam. The reported $\sigma_{\rm rms}$, in unit of mJy/beam, are given per velocity channel width of 10.5, 10.5 and 7.1 km s^{-1} for CO J=1-0, J=2-1 and J=3-2 cubes. In the last two columns we also list the Member ObsUnitSet (MOUS) of the associated ALMA observations and the Largest Angular Scale (LAS), or the maximum recoverable scale, of each dataset.

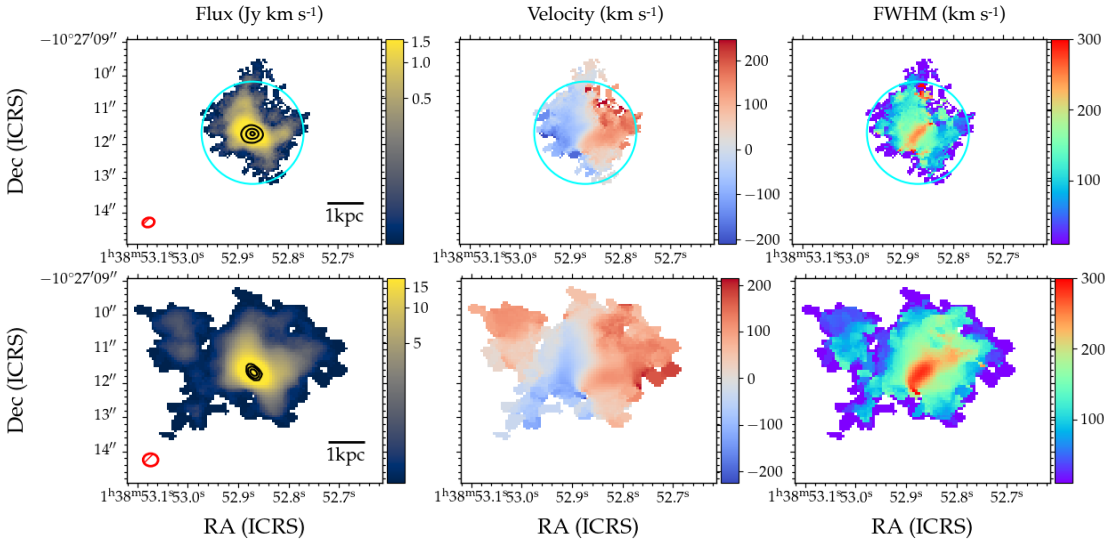


Fig. A.1: Flux, velocity and linewidth FWHM of the CO (J = 1 - 0) and CO (J = 3 - 2) emission, shown in the upper and lower panels, respectively. The 105 GHz and 334 GHz continuum emission in levels of [10, 30, 50]$\sigma_{\rm rms}$, and [5, 10, 20]$\sigma_{\rm rms}$, are overlaid in black contours over the CO (J = 1 - 0) and CO (J = 3 - 2) flux maps, respectively, where $\sigma_{\rm rms}$ are reported in Table A.1. Cyan circle mark region C, which encompasses the bulk of the cold molecular gas emission traced by CO (J = 1 - 0).

Appendix B: Fluxes of PAH features obtained from *MRS* spectra with CAFE

We provide the observed and attenuation corrected fluxes of PAH features obtained from fitting the *MRS* spectra using CAFE (Diaz-Santos et al. 2025), as described in Section 3.1.1. In Table B.1, we report values for all features identified with CAFE from the nuclear and central spectra, described in Section 3.1.1 and shown in Figure 2. The fitted optical depths of absorption features of silicate at 9.7μm ($\tau_{\rm Sil}$), water ice at 6μm ($\tau_{\rm H_2O}$), and hydrogenated amorphous carbon ($\tau_{\rm HAC}$) at 6.8 μm derived from CAFE are listed in the lower section of the Table. In Table B.2, we list values for only the brightest PAH features at 6.2, 7.7 and 11.3 μm from spectra extracted with region 1 - 9. These regions are defined in Section 3.1 and shown in Figure 5. The 6.2 and 7.7 μm PAH features are poorly constrained in region 3 and 7, hence not reported here. For the other regions, flux ratios measured between these PAH features are visualized in Figure 11. The fitted $\tau_{\rm Sil}$, $\tau_{\rm H_2O}$, and $\tau_{\rm HAC}$ derived from CAFE are listed in right side of the Table.

Table B.1: PAH features in the *MRS* nuclear and central spectra

	Nuclear		Central (3 kpc)	
Feature	f_{obs}	f_{int}	f_{obs}	f_{int}
(1)	(2)	(3)	(4)	(5)
PAH6.2	0.21±0.01	0.90±0.04	0.66±0.06	2.54±0.21
PAH7.7(C)	0.70±0.02	2.17±0.06	1.75±0.11	5.31±0.34
PAH8.3	0.09±0.01	5.31±0.34	0.22±0.02	0.81±0.09
PAH8.6	0.11±0.01	0.45±0.02	0.28±0.03	1.19±0.13
PAH11.3(C)	0.09±0.01	0.61±0.02	0.22±0.02	1.46±0.11
PAH12.6(C)	0.21±0.01	0.79±0.04	0.33±0.04	1.20±0.13
PAH17.0(C)	0.28±0.01	1.30±0.06	0.35±0.03	1.59±0.12
$\tau_{\rm Sil}$	12.0		11.6	
$\tau_{\rm H_2O}$	1.47		1.07	
$\tau_{\rm HAC}$	0.46		0.22	

Notes. (1) Name of the PAH feature or complex ("C"), where the number represents the central wavelength of the emission in μm. (2) & (3): observed and attenuation-corrected PAH flux and uncertainties derived by `CAFE` from the nuclear spectrum, in units of 10^{-15} W m^{-2}. (4) & (5): same as (2) and (3), but from spectra extracted within the central region (i.e., region C). Last three rows list the optical depths of the absorption features due to silicate, water ice and hydrogenated amorphous carbon derived with `CAFE`.

Table B.2: PAH features in *MRS* spectra extracted from region 1 - 9

	PAH6.2		PAH7.7(C)		PAH11.3(C)		$\tau_{\rm Sil}$	$\tau_{\rm H_2O}$	$\tau_{\rm HAC}$
Region	f_{obs}	f_{int}	f_{obs}	f_{int}	f_{obs}	f_{int}			
1	0.44±0.04	1.97±0.19	1.21±0.10	4.85±0.42	0.25±0.02	2.36±0.21	7.60	0.46	0.00
2	0.38 ± 0.05	1.68 ± 0.21	1.05 ± 0.09	3.96 ± 0.33	0.22 ± 0.22	1.88 ± 0.17	10.3	0.69	0.05
3	-	-	-	-	0.05 ± 0.05	0.28 ± 0.23	-	-	-
4	0.44 ± 0.1	1.62 ± 0.37	1.4 ± 0.3	4.61 ± 1.0	0.27 ± 0.27	2.0 ± 0.48	7.79	0.37	0.00
5	4.03 ± 0.21	18.1 ± 0.1	10.7 ± 0.6	38.2 ± 2.1	1.05 ± 1.05	8.4 ± 0.52	14.5	1.16	0.30
6	0.45 ± 0.09	1.29 ± 0.26	1.41 ± 0.19	3.4 ± 0.47	0.26 ± 0.26	1.29 ± 0.22	5.90	0.56	0.04
7	-	-	-	-	0.07 ± 0.07	0.08 ± 0.03	-	-	-
8	0.32 ± 0.06	1.14 ± 0.2	0.94 ± 0.12	3.0 ± 0.4	0.2 ± 0.2	1.46 ± 0.22	5.25	0.32	0.00
9	0.67 ± 0.09	2.89 ± 0.37	1.77 ± 0.18	6.77 ± 0.7	0.29 ± 0.29	2.51 ± 0.27	12.1	0.61	0.04

Notes. f_{obs} and f_{int} are observed and attenuation-corrected PAH flux and uncertainties derived by `CAFE`, in units of 10^{-16} W m^{-2}. Last three columns list the derived optical depths of the absorption features due to silicate, water ice and hydrogenated amorphous carbon.

Appendix C: Selection of best-fit models of emission line profiles

We illustrate in Figure C.1 below the model selection process described in Section 3.1 for fitting the emission line profiles. We consider the model with the lowest BIC value as the best-fit model, which correspond to a single Gaussian model, two-Gaussian model and three-Gaussian model for Huδ, H_2 0-0 S(2), and [Ne III] lines shown in Figure C.1. In the case where the BIC values are the same or have only slight difference of < 50, we choose the model with less components as the best-fit to avoid over-fitting. We also exclude models that yield a best-fit component with SNR < 5.

Appendix D: Best-fit parameters for emission lines detected in the multi-wavelength datasets

We provide the best-fit parameters of continuum-subtracted line profiles of individual emission lines from the multi-wavelength IFU datasets presented in this work, using the methodology described in Section 3.1 and Appendix D above. In Table D.1 we list the values for all mid-IR emission lines identified from the nuclear and central *MRS* spectra, defined in Section 3.1.1. Table D.2 lists the values for [Ne II], [Ne III] and H_2 0-0 S(3) lines extracted from region 1 - 9, defined in Section 3.1 and shown in Figure 5. The continuum-subtracted line profiles of these three lines are also visualized in Figure 6. Table D.3 lists the values for CO J=1-0, 2-1 and 3-2 lines extracted from region 1 - 9 and also the central region, from the multi-frequency ALMA datasets described in Appendix A. These line profiles are visualized in Figure 7. Table D.4 and D.5 report values for the brightest emission lines detected in the KCWI spectra extracted in the seven regions (i.e., exS, SE, SW, C, NE, SW, exN) defined in Section 3.3. The line profiles of Hβ and [O] III are visualized in Figure 9. For the other lines, robust decomposition is challenging due to relatively fainter emission and/or line blending, hence only the integrated line fluxes are reported (i.e., in Table D.5). The flux ratios of these lines are visualized in Figure 13.

Appendix E: Kinematic modelling of the central molecular gas disk with ^{3D}Barolo

We estimate the contribution from the rotating molecular disk to the total CO (J = 2 - 1) flux measured within the central 3 kpc covered by region C, by performing tilted-ring modeling with ^{3D}Barolo (Di Teodoro & Fraternali 2015). Agostino et al. (2026) already performed kinematic modelling of the nuclear molecular disk with ^{3D}Barolo using CO (J = 2 - 1) observations with an angular resolution of $\sim 0\farcs02$ (19 pc), which is more than 10 times higher than the CO (J = 2 - 1) observation used this work that

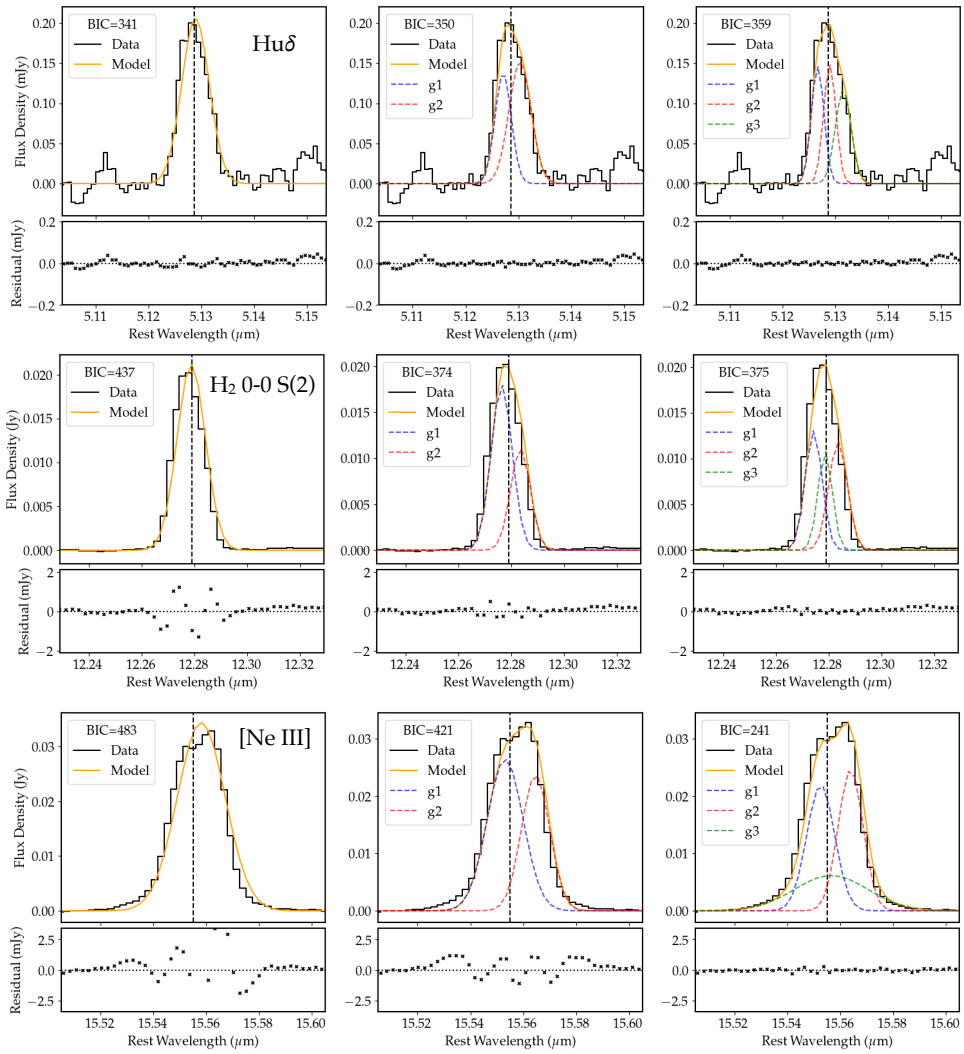


Fig. C.1: Continuum-subtracted line profiles of the Huδ, H_2 0-0 S(2), and [Ne III] lines detected in the nuclear *MRS* spectrum (Figure 2), shown in black curves, respectively in the top, middle and bottom panels. The model fitting results (in orange curves) and residual using one, two and three Gaussian components are shown from left to right. The individual Gaussian components (i.e., "g1", "g2", "g3") for multi-Gaussian models are shown in dashed blue, red and green curves.

focuses on the extended emission. Here we assume that the massive nuclear molecular gas disk modeled by Agostino et al. (2026) on ∼10-pc scale also dictates the rotational motion on kpc-scale, and hence we model the inner kpc (∼ 1″) of the low-resolution CO (J = 2 - 1) emission by fixing the inclination and PA to values derived by Agostino et al. (2026) from high-resolution observations, which are 60° and 256°, respectively. The rotational velocity and dispersion are allowed to vary freely. The modelling results are shown below in Figure E.1 in red contours over the PV diagrams extracted along the major (ϕ = 256°) and minor axis (ϕ = 345°), shown in grey scales. The model accounts for ∼ 60% of the total CO (J = 2 - 1) flux, as shown in the rightmost panel. Region C, indicated with vertical dashed cyan lines in the PV diagrams, covers the bulk of the cold molecular gas outflow that is most visible along the minor axis, while excluding the tidal feature seen towards NE that is most visible along the major axis. We note that the modelling performed here is only meant as an independent assessment of the disk contribution, rather than an accurate representation of the underlying gas kinematics, given that the observed gas motions within the central kpc may still be impacted by the outflow.

Appendix F: Channel maps for the multi-phase gas tracers

To better visualize the kinematic features present in IRAS F01364, we present here channel maps for [Ne III] 15.6μm, H_2 0-0 S(3), CO (J = 2 − 1) and [O III] λ5007 lines, respectively in Figure F.1, F.2 and F.3. We only show channels over the velocity ranges where emission is seen, which is approximately −500−+350 km/s for H_2 0-0 S(3), −600−+700 km/s for [Ne III] 15.6μm, −300−+300 km/s for CO(2-1) and −450 − +500 km/s for [O III] λ5007. The channels displayed were selected to center around the velocity channel closest to 0 km/s with spacings of 3, 3, 5 and 6 channels for [Ne III] 15.6μm, H_2 0-0 S(3), CO (J = 2 − 1) and [O III] λ5007, respectively, to account for the different instrument spectral resolutions. In all panels, we additional show the direction of the kinematic major axis of the stellar disk (i.e., Figure 8), represented in white dashed lines, and the outlines of the NW and SE outflow

Table D.1: Emission lines detected in the *MRS* nuclear and central spectra

			Nuclear Region			Central Region		
Line	λ_{rest}	IP	f_{obs}	v_{cen}	FWHM	f_{obs}	v_{cen}	FWHM
(1)	(2)	(3)	(4)	(5)	(6)	(7)	(8)	(9)
H_2 0-0 S(9)	4.69		0.62±0.06	60±8	285±19	5.16±0.17	33±4	360±9
H_2 0-0 S(8)	5.05		0.43±0.02	48±2	306±5	2.67±0.10	39±3	321±9
Huδ	5.13	13.6	0.16±0.01	27±8	360±20	0.74±0.11	142±30	646±72
[Fe II]	5.34	7.9	1.66±0.08	-25±8	262±9	5.19±0.37	-35±11	249±14
			0.85±0.08	169±7	198±8	3.26±0.38	163±10	200±12
H_2 0-0 S(7)	5.51		1.54±0.12	-40±11	233±10	8.99±0.54	-46±12	246±13
			0.73±0.12	131±13	189±12	4.25±0.57	135±13	194±14
Huγ	5.91	13.6	0.17±0.01	121±9	423±22	0.43±0.06	87±25	548±50
H_2 0-0 S(6)	6.11		0.80±0.02	-6±2	284±5	5.18±0.14	-4±3	306±6
H_2 0-0 S(5)	6.91		2.99±0.13	0±6	218±7	14.9±0.5	-30±4	213±4
			1.00±0.14	167±11	178±10	9.15±0.48	151±5	196±6
[Ar II]	6.99	15.8	1.19±0.06	-63±1	218±2	2.81±0.17	-60±1	216±2
			1.10±0.06	162±1	198±2	2.52±0.15	164±1	190±1
			1.18±0.12	-48±22	1211±64	2.86±0.32	-73±28	1220±76
Pfα	7.46	13.6	1.34±0.11	153±12	445±28	2.82±0.19	146±9	407±21
H_2 0-0 S(4)	8.03		2.77±0.11	12±4	303±9	13.1±0.2	2±2	318±4
[Ar III]	8.99	27.6	0.17±0.49	-45±3	164±10	0.30±0.02	-55±2	162±7
			0.19±0.55	173±6	182±12	0.35±0.02	153±3	197±7
			0.39±0.16	-10±35	384±22	0.82±0.26	2±18	514±48
H_2 0-0 S(3)	9.66		2.85±11.59	-26±10	221±7	18.1±0.6	-35±5	237±6
			0.85±0.31	128±25	202±18	7.10±0.66	155±8	193±8
[S IV]	10.51	34.8	0.05±0.02	-61±4	173±12	0.13±0.14	-60±6	188±13
			0.06±0.01	177±7	217±12	0.18±0.14	170±7	197±16
			0.13±0.05	-28±40	489±50	0.29±0.15	-43±53	532±69
H_2 0-0 S(2)	12.28		4.00±0.24	-50±9	209±9	11.6±0.54	-53±5	210±6
			1.67±0.25	124±13	179±13	6.44±0.56	135±7	180±7
Huα	12.37	13.6	0.50±0.06	170±18	475±42	0.77±0.08	162±17	467±39
[Ne II]	12.81	21.6	5.56±0.32	-53±2	216±3	9.71±0.51	-51±1	215±3
			5.21±0.30	171±1	199±3	9.11±0.48	169±1	198±3
			5.74±0.79	34±17	1030±64	9.97±1.30	32±14	928±54
[Ne V]	14.32	97.1	0.29±0.06	183±24	336±56	0.45±0.08	190±21	343±51
[Cl II]	14.37	13.0	0.56±0.07	41±15	374±34	0.83±0.09	40±12	357±29
[Ne III]	15.56	41.0	1.39±0.08	-35±4	208±8	2.02±0.03	-36±3	204±6
			1.23±0.08	183±3	176±9	1.83±0.03	179±2	177±6
			2.56±0.92	29±18	607±68	4.33±0.39	29±11	613±41
H_2 0-0 S(1)	17.04		9.06±0.30	-57±5	196±5	24.2±0.7	-44±3	214±4
			4.69±0.31	128±6	156±6	9.75±0.66	150±4	145±4
[S III]	18.71	23.3	7.11±0.18	50±3	341±6	9.55±0.24	50±3	346±6
[O IV]	25.89	54.9	17.0±3.1	-170±92	1524±219	19.3±3.6	-178±97	1607±231

Notes. 1): Name of the emission line. (2): Rest wavelength in μm. (3): Ionizing potential, in eV. For each line, we list the best-fit parameters of the individual Gaussian components. (4) & (7): Component flux, in 10^{-18} W m^{-2}. (5) & (8): Central component velocity relative to the galaxy systemic velocity, in km s^{-1}. (6) & (9): Component FWHM in km s^{-1}. The instrumental FWHM (see Section 2.2) has been subtracted in quadrature from the reported values. See Section 3.1 for details.

cones, in dashed cyan lines. The latter were defined based on the FWHM linewidth-enhanced regions identified in [O III]λ5007 (i.e., Figure 9).

Table D.2: Best-fit parameters for [Ne III], [Ne II] and H_2 0-0 S(3) lines in region 1 - 9

Region	[Ne III]			[Ne II]			H_2 0-0 S(3)		
	f_{obs}	v_{cen}	FWHM	f_{obs}	v_{cen}	FWHM	f_{obs}	v_{cen}	FWHM
	(1)	(2)	(3)	(4)	(5)	(6)	(7)	(8)	(9)
1	0.43±0.03	170±3	147±7	2.43±0.24	181±4	146±12	1.07±0.93	24±20	277±10
	0.84±0.04	70±5	350±5	4.44±0.31	65±8	337±7	1.20±1.00	101±4	185±12
2	0.33±0.02	-9±5	272±7	1.35±0.08	-20±3	234±7	0.89±0.17	-91±3	220±10
	0.23±0.02	191±2	170±7	1.12±0.07	180±2	185±6	1.33±0.13	23±12	352±7
	0.57±0.09	185±20	507±18	1.44±0.35	106±15	653±51	-	-	-
3	0.03±0.02	-65±5	225±18	0.13±0.01	-70±4	203±11	1.73±0.19	-94±2	168±9
	0.03±0.03	177±7	260±16	0.14±0.01	155±4	222±11	1.40±0.33	-67±7	342±23
	0.08±0.05	53±21	663±108	0.35±0.07	-5±20	599±64	-	-	-
4	0.43±0.10	13±21	235±43	4.23±0.14	42±5	344±5	3.34±1.53	47±49	264±35
	0.16±0.09	175±6	140±7	1.54±0.11	181±3	134±8	5.01±1.21	166±4	167±13
	0.87±0.30	-24±11	526±39	-	-	-	-	-	-
5	1.16±0.02	-35±5	206±9	5.45±0.27	-52±1	216±3	4.65±1.71	-23±6	231±5
	1.01±0.02	184±4	169±12	5.08±0.26	171±1	198±3	1.39±0.23	142±10	187±9
	2.35±1.08	42±15	534±67	5.15±0.60	-12±16	985±53	-	-	-
6	0.67±0.09	-54±4	172±8	2.68±0.46	-73±4	189±13	4.20±0.14	-87±1	171±3
	0.29±0.04	188±9	170±22	4.02±0.38	87±18	343±16	1.29±0.24	-47±6	330±15
	1.63±0.25	113±12	494±22	-	-	-	-	-	-
7	0.06±0.01	-104±10	288±13	0.23±0.02	-55±6	244±13	2.30±0.50	30±34	314±24
	0.05±0.01	120±4	220±13	0.21±0.02	148±4	220±12	2.17±0.52	168±5	215±13
	0.13±0.03	-79±21	680±67	0.37±0.14	-85±45	688±84	-	-	-
8	0.20±0.02	-56±2	186±5	0.94±0.03	-64±2	192±4	2.33±0.21	-18±12	240±10
	0.21±0.02	158±2	208±5	1.01±0.03	150±2	212±4	2.03±0.22	163±10	219±9
	0.49±0.05	-137±22	542±18	1.32±0.18	-59±15	617±27	-	-	-
9	0.47±0.09	-51±5	159±6	3.06±1.52	-75±4	183±12	1.93±0.27	-34±3	157±8
	0.24±0.05	158±15	120±31	4.59±0.48	59±14	336±10	2.29±0.37	15±7	249±6
	1.16±0.21	-33±14	473±16	-	-	-	-		-

Notes. (1), (4), (7): Component flux, in 10^{-18} W m^{-2}. (2), (5), (8): Central component velocity relative to the galaxy systemic velocity, in km s^{-1}. (3), (6), (9): Component FWHM in km s^{-1}. The instrumental FWHM (see Section 2.2) have been subtracted in quadrature from the reported values. These parameters are visualized in Figure 6.

Table D.3: Best-fit parameters for CO (1-0), CO (2-1) and CO (3-2) lines

Region	CO (1-0)			CO (2-1)			CO (3-2)		
	$S_\nu\Delta v$	v_{cen}	FWHM	$S_\nu\Delta v$	v_{cen}	FWHM	$S_\nu\Delta v$	v_{cen}	FWHM
	(1)	(2)	(3)	(4)	(5)	(6)	(7)	(8)	(9)
1	2.06±0.27	59±7	167±16	2.64±0.70	65±3	125±16	13.9±0.7	61±3	202±8
	-	-	-	4.61±1.41	60±5	260±27	-	-	-
2	-	-	-	1.91±0.53	−21±34	482±71	4.23±0.73	−85±10	183±24
	-	-	-	0.79±0.24	−104±10	143±32			
3	1.15±0.30	−125±18	208±42	1.79±0.17	−95±5	167±12	3.73±0.57	−87±8	156±18
4	2.49±0.27	150±6	176±14	6.38±1.27	154±3	149±11	11.9±3.3	160±4	146±17
	-	-	-	2.00±1.23	25±99	257±109	8.5±3.3	32±65	264±71
5	7.47±1.08	131±14	193±16	24.8±0.7	140±2	176±3	46.4±1.8	149±3	171±4
	7.77±1.08	−44±17	209±21	32.3±0.7	−44±3	215±4	67.7±1.9	−41±4	224±6
6	2.90±0.27	−91±5	177±13	7.98±0.19	−87±1	194±3	15.8±0.8	−82±3	182±7
7	1.22±0.37	172±29	301±69	2.76±0.20	116±7	305±17	9.35±0.96	121±10	300±23
8	2.07±0.32	171±16	313±37	1.45±0.41	150±9	157±29	13.1±0.8	96±6	285±14
	-	-	-	5.33±0.75	70±13	358±19	-	-	-
9	3.80±0.27	−26±4	182±10	12.0±0.2	−27±1	180±2	23.6±0.6	−25±2	190±4
C	21.9±6.7	103±51	276±61	44.9±2.1	140±4	182±5	77.0±5.3	151±5	163±7
	13.1±7.3	−76±30	202±38	69.1±2.2	−43±4	216±6	151±6	−34±5	221±8

Notes. (1), (4), (7): Component flux, in Jy km s^{-1}. (2), (5), (8): Central component velocity relative to the galaxy systemic velocity, in km s^{-1}. (3), (6), (9): Component FWHM in km s^{-1}. These parameters are visualized in Figure 7.

Table D.4: Best-fit parameters for Hβ and [O III]λ5007 lines

Region	Hβ			[O III]λ5007		
	f_{obs} (1)	v_{cen} (2)	FWHM (3)	f_{obs} (4)	v_{cen} (5)	FWHM (6)
exS	1.69±0.10	94±8	409±19	2.61±0.31	75±10	474±31
	-	-	-	0.70±0.12	109±5	120±16
SE	1.29±0.21	210±18	806±58	3.28±0.10	159±6	704±15
	0.81±0.09	146±6	297±22	0.09±0.03	181±8	60±22
SW	0.58±0.09	203±8	111±17	0.79±0.11	172±13	176±24
	0.34±0.07	311±6	48±11	0.29±0.08	287±4	46±14
C	3.46±0.80	44±28	244±24	2.51±0.24	14±10	204±16
	2.93±0.87	200±20	216±17	1.67±0.22	170±7	142±10
	1.75±0.30	137±21	874±65	3.91±0.37	101±8	637±26
NW	0.40±0.10	-75±16	301±57	4.12±0.09	-30±5	688±11
	0.34±0.04	187±4	111±11	0.35±0.03	154±3	66±7
	1.46±0.24	-75±22	970±76	-	-	-
NE	0.64±0.08	119±16	209±21	0.53±0.13	19±31	214±48
	0.22±0.06	224±4	70±17	0.50±0.11	176±9	124±17
exN	2.47±0.15	119±8	393±18	5.10±0.16	115±4	402±10

Notes. (1)(4): Component flux, in 10^{-16} erg s^{-1} cm^{-2}. (2)(5): Central component velocity relative to the galaxy systemic velocity, in km s^{-1}. (3)(6): Component FWHM in km s^{-1}. These parameters are visualized in Figure 9.

Table D.5: Flux measurements of optical emission lines detected with KCWI

Region	[O II]λ3726	[O II]λ3729	Hα	[N II]λ6584	[O I]λ6300	[S II]λ6716	[S II]λ6731
exS	5.20±1.52	6.17±1.38	10.3±1.0	8.66±0.96	4.01±0.45	1.61±0.12	1.11±0.08
SE	7.75±2.36	2.98±7.92	11.0±0.2	21.0±0.3	3.46±0.19	5.30±0.05	4.06±0.05
SW	3.35±0.39	3.97±0.37	6.21±0.10	4.47±0.10	1.93±0.18	2.95±0.05	2.03±0.04
C	10.3±1.0	15.0±0.8	46.3±0.6	42.7±0.6	10.7±0.3	18.1±0.1	13.0±0.1
NW	6.77±17.37	9.85±4.38	7.81±2.02	10.6±0.3	1.34±0.11	2.45±0.08	1.80±0.06
NE	2.25±0.22	2.39±0.21	3.09±0.50	2.51±0.35	1.32±0.16	1.75±0.16	1.21±0.11
exN	7.92±1.53	8.97±1.35	19.7±1.7	6.75±0.86	1.59±0.21	1.46±0.14	1.58±0.14

Notes. Values are in units of 10^{-16} erg s^{-1} cm^{-2}.

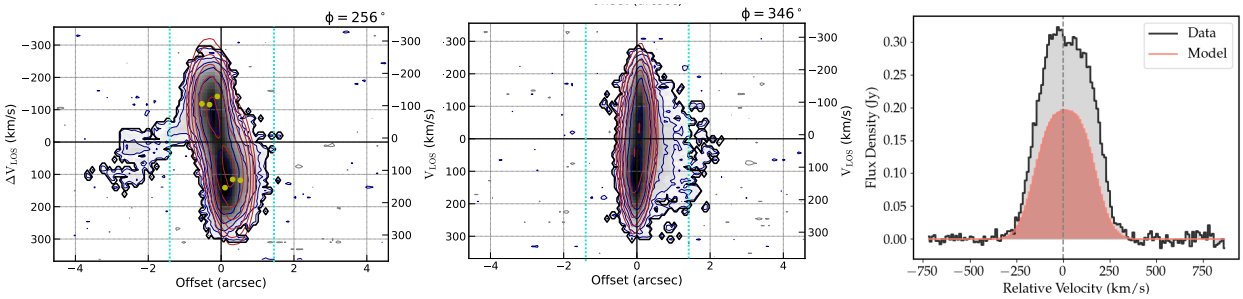


Fig. E.1: Modelling results of the central kpc of the CO (J = 2 - 1) emission from ^{3D}Barolo. The left and middle panels show the PV diagrams of the fitted model of the nuclear rotating molecular disk (in red contours), along the major (ϕ = 256°) and minor axis (ϕ = 345°) previously determined by Agostino et al. (2026). The observed emission are shown in grey scales, and area covered by region C is indicated with vertical dashed cyan lines. The right panel compares the observed and modeled CO (J = 2 - 1) line profile extracted from region C, shown in grey and red, respectively. The modeled nuclear disk contributes 60% of the total flux contained within region C.

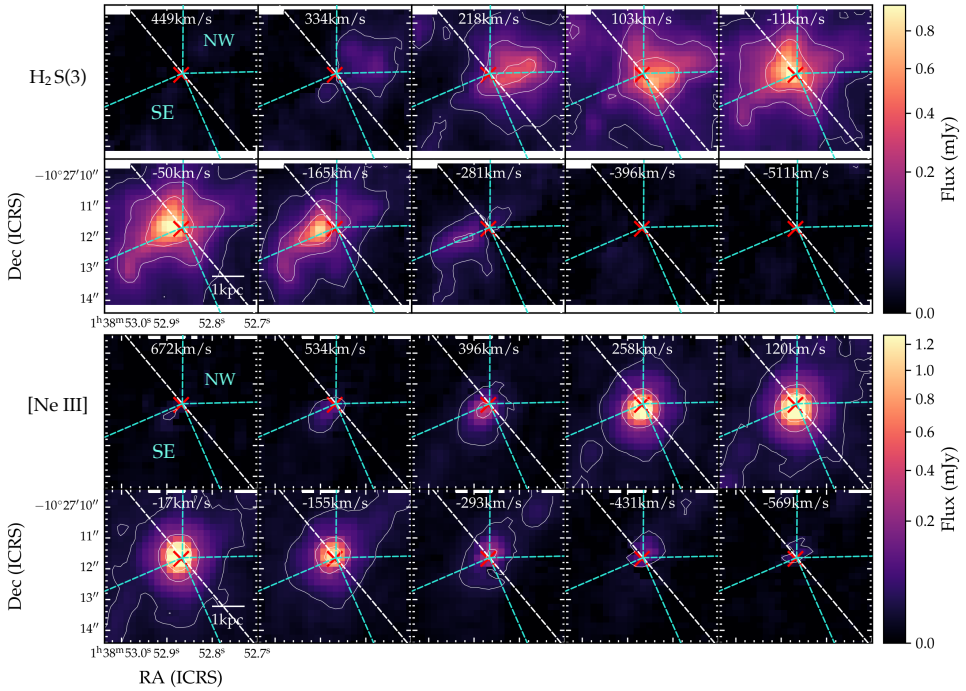


Fig. F.1: Channel maps for (top) H_2 0-0 S(3) and (bottom) [Ne III]15.6μm lines observed with *JWST/MIRI-MRS*. Red cross mark the position of the nucleus based on the ALMA 334 GHz continuum image. White and cyan dash lines represent the kinematic major axis of the stellar disk, and the outlines of the NW and SE outflow cones, respectively. White contours show levels of 0.015, 0.09 , 0.3 mJy, and 0.016, 0.24 , 0.8 mJy, for the top and bottom panels respectively.

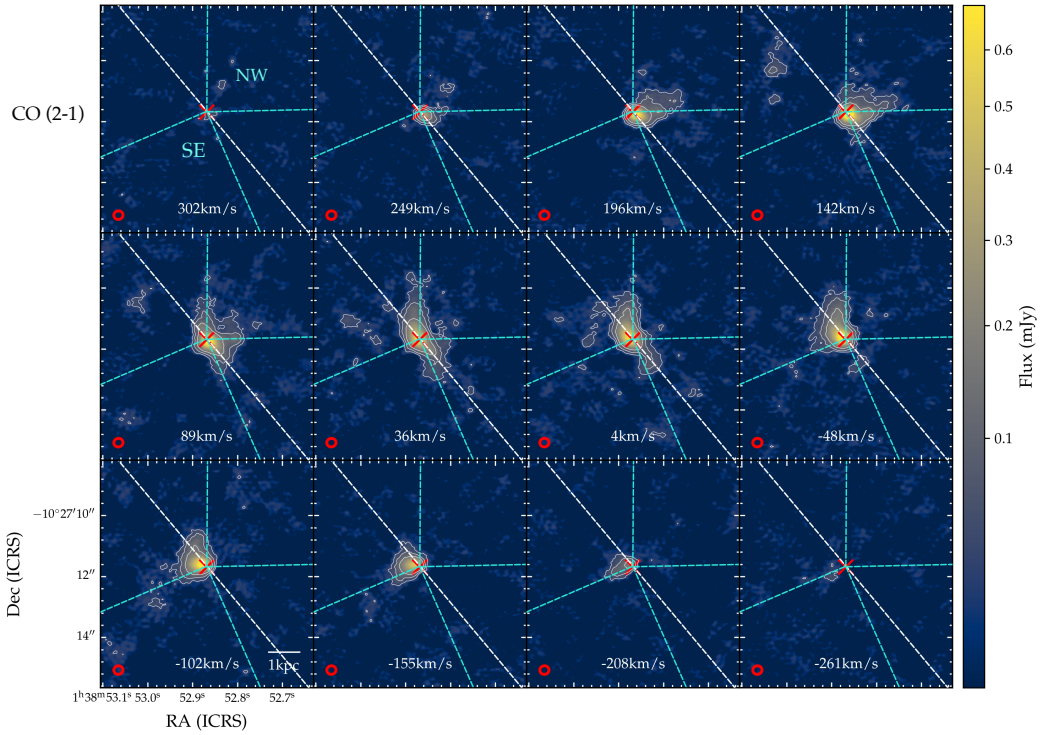


Fig. F.2: Channel maps for the CO(J = 2 - 1) line observed with ALMA. Red cross, white and cyan dashed lines are the same as in Figure F.1. White contours show levels of 0.04, 0.07, 0.14 mJy.

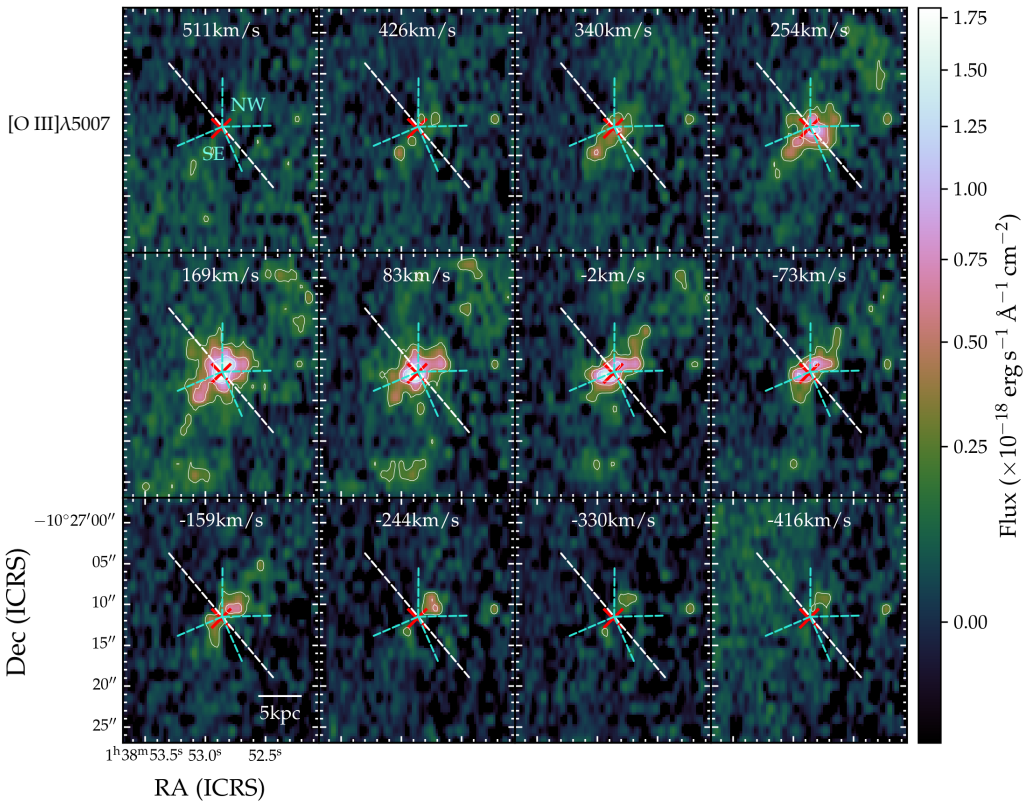


Fig. F.3: Channel maps for the [O III]λ5007 line observed with Keck/KCWI. Red cross, white and cyan dashed lines are the same as in Figure F.1. White contours show levels of 0.2, 0.5, 1.0 $\times 10^{-18}$ erg s^{-1} Å^{-1} cm^{-2}.